UNIVERSITÀ DEGLI STUDI DI PADOVA

DIPARTIMENTO DI FISICA E ASTRONOMIA "GALILEO GALILEI"

MASTER THESIS IN ASTROPHYSICS AND COSMOLOGY

Dark matter in galaxy clusters in the context of ΛCDM and MOND

SUPERVISOR
PROF. ALESSANDRO PIZZELLA
UNIVERSITÀ DEGLI STUDI DI PADOVA

CO-SUPERVISOR
DR. FEDERICO LELLI
INAF- OSSERVATORIO ASTROFISICO DI ARCETRI

CANDIDATE
RUTH KELLEHER

STUDENT ID
2039504

ACADEMIC YEAR
2022/23

Abstract

The nature of dark matter remains one of the most significant unsolved mysteries in the field of physics. The observations that lead to the dark matter problem are reviewed in Chapter 1 of this thesis. There are many proposed solutions for the various unexplained phenomena. Two major frameworks that continue to be tested today are the lambda cold dark matter cosmological model (ΛCDM) and Milgromian dynamiccs or MOdified Newtonian Dynamics (MOND). This thesis tests both frameworks using galaxy clusters. Galaxy clusters were chosen as the object of this investigation because they are the largest virialized systems in the Universe, so they are at the intersection of cosmology and astrophysics.

In the context of Newtonian dynamics, dark matter halo models with different density profiles were fit to the cluster data. These models were the pseudo-isothermal profile, Burket profile, Lucky-13 profile, NFW profile and the Einasto profile. The simple case of scaling up the baryonic component was also investigated. These models were quantitatively compared and the best fit profile was found to be the pseudo-isothermal profile. This cored profile was favored over the ΛCDM NFW and Einasto profiles, adding further evidence to the "cusp-core problem" that has been observed for galaxies. The NFW and Einasto profiles were investigated further using ΛCDM scaling relations, to varying degrees of success.

The observations from the clusters were then fit using MOND. Firstly it was found that additional mass is still needed for MOND in clusters, which is a well known issue. This missing mass was attempted to be modelled in the same way as before using density profiles. The profiles used here were cored density profiles with a converging mass, a density profile proportional to $1/r$, and a truncated sphere with constant density. The best fit profile here was the cored profile. In order to determine the nature of this missing mass, a number of correlation tests were applied to the data.

An estimation of the possible hydrostatic bias was performed in the context of MOND. The Newtonian models and MOND models were compared using the data unaffected by hydrostatic bias. It was found that the MOND cored density profile was the overall best fit model. This, among other successes for MOND throughout this thesis, as well as some issues arising for ΛCDM, gives further credence to the theory of MOND. The missing mass needed in MOND in galaxy clusters, however, does not have a clear explanation, but some hints were found that it may be possibly related to the properties related to the properties of the ICM, most notably its temperature.

Contents

List of Figures

11

12

13

14

List of Tables

1

Introduction

1.1 A History of Dark Matter

One of the biggest unanswered questions in physics today is the nature of dark matter. The idea that there could be some form of "dark matter" identified by its gravitational effect, was proposed as early as the 19th century, by studying the orbits of the planets in the Solar System. During the 1840s, Urbain Le Verrier and Johan Couch Adams found anomalies in the orbit of the outermost planet that was known in the Solar System at the time, Uranus. They proposed the existence of an unobserved "dark planet". This planet was discovered in 1846 by J. G. Galle and H. L. d'Arrest by pointing their telescope in the direction of Uranus, predicted by the calculations of Le Verrier. This planet that was named Neptune. Le Verrier subsequently found another anomaloy in the Solar System. He found that there was an anomalous degree of precession of the perihelion of Mercury and so proposed again that there was some missing mass in the form of a "dark planet" that he named Vulcan. [7] This planet was never discovered and we know now that the reason for the anomalous precession is due to General Relativity. The history of these gravitational anomalies in the Solar System are interesting, as they highlight two completely different explanations for the same problem. In the case of Uranus there was indeed some missing matter present in form of Neptune but in the case of

Mercury the solution was a drastic change and extension of the gravitational physics that was known at the time. This interplay between dark matter and modifying gravitational physics is still very relevant today and is the focus of this thesis.

1.1.1 Evidence from galaxy dynamics

Skipping ahead to the early 20th century, the investigations extended from our Solar System to the Milky Way. In 1906 Lord Kelvin attempted to perform a dynamical estimate of the mass of the Milky Way galaxy, proposing that some of the stars could be "extinct and dark". Henri Poincaré responded to this work and for the first time coined the term "dark matter" ("matiére obscuré" in the original French). However, he proposed that the abundance of this dark matter was less than that of visible matter [8]. Scientists continued to posit about the mass of the galaxy and whether this missing or dark mass in the form of faint stars was relevant. In 1932 Dutch astronomer Jan Oort studied the vertical kinematics of stars in the solar neighbourhood by using their Doppler shifts in order to calculate their velocities. He found that the vertical velocity dispersion of stars was much higher than should be possible from the gravitational pull of the luminous mass. He therefore postulated that there was some unseen mass to account for these velocities. Oort also estimated that the maximum allowed amount of dark matter was less than half of the total mass [9]. Luminous matter was still thought to be the dominant type at this time.

During the same years of Oort's investigation, the Swiss astronomer Fritz Zwicky was studying the redshifts of galaxies in the Coma cluster. He found that the velocity dispersion of the galaxy members was significantly larger than the estimated escape velocity from the cluster potential well. This led to the absurd result that the entire galaxy cluster should have been unbound. Armed with this knowledge he then used the Virial theorem to determine the mass of the cluster. This led him to the conclusion that "*If this would be confirmed, we would get the surprising result that dark matter is present in much greater amount than luminous matter*". [10] This was the first time a galaxy cluster's mass was estimated, and it was done so in the context of dark matter. Soon after this revelation, Sinclair Smith analysed data of the Virgo Cluster and came to similar conclusions [11].

Further work was performed in the coming decades but it wasn't until the 1970s with the publication of rotation curve of M31 by Vera Rubin, that things propelled
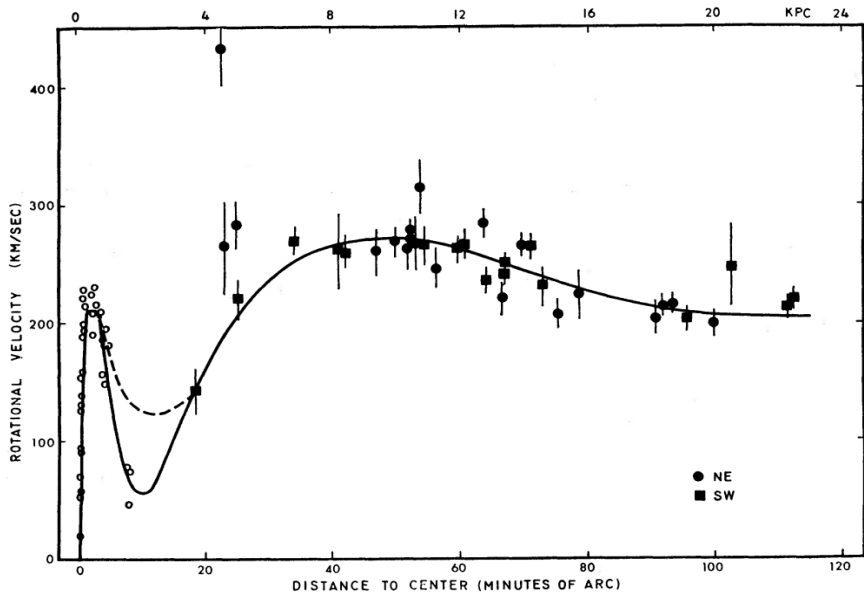
Figure 1.1: The rotation curve of M31 from [1] showing the unexpected flatness at large radii

forward. It was expected that the rotation curve would follow the Keplerian decline at large radii as $V(r) = \sqrt{GM(r)/r}$ where $V(r)$ is the rotational velocity at radius r, G is the gravitational constant and $M(r)$ is the mass contained within radius r. However this Keplerian decline of $V(r) \propto 1/\sqrt{r}$ was not observed. Instead, Rubin and her team observed that the rotation curve of M31 was roughly flat, as seen in Figure 1.1. This meant that the outer regions of the galaxy were rotating at roughly the same speed as the inner regions. [1] One explanation of this observation is that there is a large amount of unseen matter in these outer regions which would exert a gravitational pull on the visible matter causing it to rotate faster.

In 1972 D. Rogstad and G. Shostak built on this work, extending the study to 5 galaxies. They observed the 21cm line emitted by neutral Hydrogen gas to map the distribution and motion of Hydrogen gas in the galaxies out to large radii. They observed that these rotation curves were also asymptotically flat out to very large radii - beyond the bulk mass of luminous matter [12]. Many more papers were published in the next decade, most notably that of Bosma as part of his Ph.D. thesis [13] and additional studies carried out by Rubin et al. [14] which all came to the same conclusions; asymptotically flat rotation curves out to large radii are ubiquitous among disk galaxies.

21

1.1.2 Evidence from galaxy clusters

It should be noted that these results were not accepted at first, in particular the conclusions drawn from clusters which were displaying very large mass discrepancies with dynamical mass-to-light ratios of the order of 100-1000. Later on, with the advent of X-ray astronomy in the 1980s, it was discovered that galaxy clusters are permeated by hot diffuse gas known as the intracluster medium (ICM). This gas constitutes the bulk of the visible baryonic mass. In fact, in galaxy clusters, the mass of gas and stars inside individual galaxies accounts for just about 10% of the mass of the ICM. This lead to a major revision of the measured dynamical mass-to-light ratios of galaxy clusters to a factor of 5-10.

Subsequently, gravitational lensing was put forward as a method to probe the mass distribution in clusters. Gravitational lensing is a consequence of General Relativity which posits that a massive object causes the fabric of space-time to curve due to the object's gravitational field. This causes propagation of electromagnetic radiation to deflect from its original straight line path and instead to follow geodesics on this curved surface. The angle of deflection is given by $\alpha = 4GM/bc^2$ where G is the gravitational constant, M is the mass of the body, b is the impact parameter and c is the speed of light. This means that the amount by which the light is deflected is proportional to the mass of the body, making it advantageous in the study of clusters. Due to their large mass, the deflection should also be large and therefore easier to measure. The idealized scenario is where there is a galaxy directly behind the cluster along the observer's line of sight. In this case an Einstein ring is formed where the light from the background galaxy is distorted by the cluster to form a ring-like structure around the cluster. The distortion of light from galaxies can be seen in Figure 1.2 where some of the galaxies are spread as arcs of light. The angular radius of the Einstein ring θ_E is related to the mass of the cluster by

$$\theta_E = \sqrt{\frac{4GM}{c^2}\frac{D_{LS}}{D_L D_S}} \tag{1.1}$$

where D_{LS} is the distance from lens to source, D_L is the distance from observer to lens and D_S is the distance from observer to source[15]. This method was applied to a number of clusters[16] which led to the conclusion that the luminous mass in clusters was only a fraction of the total mass.

Figure 1.2: The gravitational lensing in the cluster A2218 from Hubble Space Telescope imaging [2]. The cluster is so massive that its gravitational field deflects the light passing through it, producing the arcs in the image. These arcs are very distant galaxies to the cluster.

The Bullet Cluster

The most notable study employing this method is that of the colliding cluster 1E0657-558, also known as the Bullet Cluster. In the paper titled "A direct empirical proof of the existence of dark matter", Clowe et al. [17] used X-ray observations to determine the hot gas mass distribution as well as gravitational lensing to determine the total mass distribution. They found that the two distributions are offset, meaning the majority of the mass in the cluster is separated from the mass in the ICM. In a particle dark matter scenario, this is expected because dark matter is collisionless, meaning that the dark matter haloes of the two clusters will pass through each other, similarly to the individual galaxies. However, the hot gas is highly collisional, so the ICM remains in between the two colliding objects.

That being said, the Bullet cluster may not be a clear victory for ΛCDM as it has been presented. The smaller cluster moving through the larger cluster created a shock wave, with a very large velocity. It was estimated to be as high as 4740 km/s or as low as 2700 km/s, but the velocity which best reproduces the data is 3100km/s as seen in Mastropietro and Burkert [18]. The difference in these values is due to a difference in the initial conditions of the velocities of the clusters. Lee and Komatsu [19] attempted to determine how likely these kinds of high-velocity merging systems

are in the ΛCDM paradigm. They used a large N-body cosmological simulation to determine the distribution of velocities at which subclusters fall towards the main clusters. They found that the existence of this system is incompatible in ΛCDM by more than 99.91% confidence level at $z = 0$. Subsequent to the estimation of the upper limit velocity of 4740 km/s, the mass of the main cluster was refined. With this new information the probability of the clusters creating a shock wave with this velocity decreased to 10^{-7}. [20] [21]

1.1.3 Evidence from Cosmology

During these same years the field of Cosmology was developing fast. The first clear connection between dark matter and Cosmology can be summarised by the opening argument in Ostriker et al. [22] "*There are reasons, increasing in number and quality, to believe that the masses of ordinary galaxies may have been underestimated by a factor of 10 or more. Since the mean density of the Universe is computed by multiplying the observed number density of galaxies by the typical mass per galaxy, the mean density of the Universe would have been underestimated by the same factor.*" This led to questions surrounding the formation of structure and the evolution of the Universe.

To begin, the basis of Cosmology stands on the Cosmological Principle which states that the Universe is homogeneous and isotropic. This has been proven to be true on large scales through measurements of the Cosmic Microwave Background (CMB). In Big Bang Cosmology, there was a time when the Universe consisted of an opaque plasma of ionized primordial gas and photons constantly scattering. As the Universe expanded and cooled, the electrons and protons combined to form neutral Hydrogen which was no longer energy efficient in scattering the photons. These photons did their "last scattering" and were then allowed to freely travel. This relic radiation is what we measure today as the CMB. The CMB radiation shows that the early Universe is indeed homogeneous and isotropic to a very good approximation, in agreement with the Cosmological Principle.

Although the CMB emission is extremely uniform (2.73K everywhere), through missions such as WMAP [3] and COBE [23], tiny fluctuations were measured of the order 10^{-5}K, as seen in Figure 1.3. Since the fluctuations are uniform across the whole sky, they can be characterized by the CMB angular power spectrum,
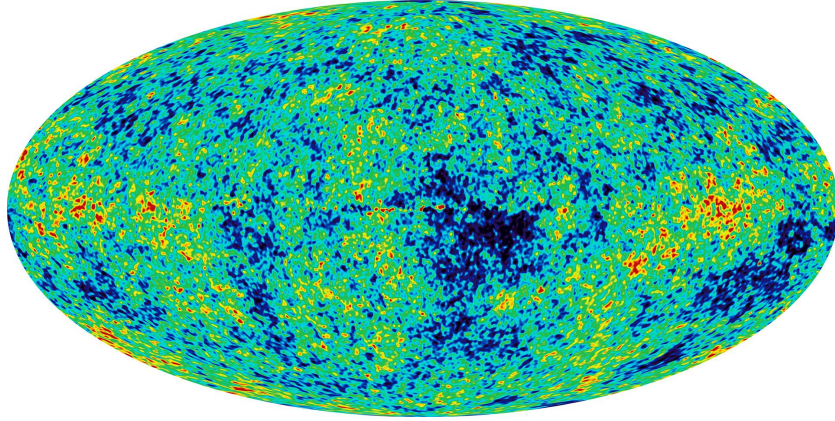
Figure 1.3: A heat map of the temperature fluctuations in the CMB. The redder spots are cooler than the blue ones but the temperature difference is only $\pm 200 \mu K$, corresponding to density fluctuations of the order 10^{-5}. [3]

a description of how the amplitude of the temperature fluctuations varies as a function of angular scale shown in Figure 1.4. The various scales are due to different effects. On small scales the fluctuations are due to acoustic oscillations of the primordial plasma; the fluid is stretched and compressed in a repeating cycle due to the presence of local potential wells. When the photons decoupled from the fluid, some were in the peaks of the fluctuations and some in the troughs, meaning they emerged from the plasma with varying temperature.

On large scales the fluctuations are due to the early Sachs-Wolfe effect. This is where the photons escape the gravitational well to travel towards us, losing energy as they travel due to gravitational redshift. If a photon travelled out of a deep potential well, then the photon will experience a larger redshift, and so will be cooler in the CMB. The converse is true for small potential wells. Both of these effects depend on the initial density perturbations that allowed for the formation of early gravitational wells as well as dynamics of the photon-baryon fluid. This means that the amount of baryons present at the time is crucial. If the Universe were made only by baryons plus radiation at last scattering, we would expect a "damped" power spectrum in which the relative height of the peaks progressively decrease towards smaller angular scales or higher multipole moment l. This means the first peak in the CMB power spectrum would be the higher than the second, the second higher than the third, and so on. Instead we observe that the third peak is higher than the second. In order to explain this ratio, we need an extra source of

25

the gravitational potential wells that is displaced from the baryons. This has been hypothesised to be provided by non-baryonic dark matter which is a new type of particle beyond the standard model of particle physics.
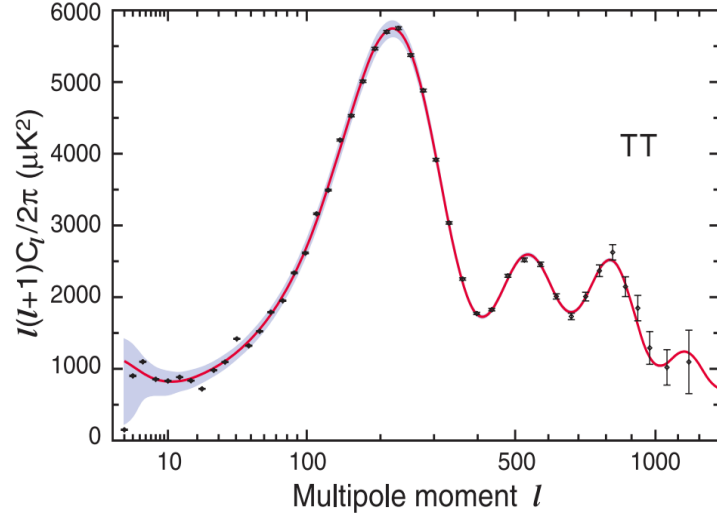
Figure 1.4: The Angular Power Spectrum derived from the whole sky map from Bennett et al. [3]. The data along with their error bars obtained from WMAP are in black and the red curve is the ΛCDM best-fit model. The shaded region is the smoothed binned cosmic variance. The y-axis represents the temperature fluctuations, as seen in Figure 1.3, with some scaling coefficients. The x-axis displays the multipole moment which is inversely related to the angular scale.

In addition, according to linear perturbation theory, the fluctuations can grow by, at most, the ratio of the scale factor today to the scale factor at recombination. This ratio is approximately a factor of 10^3, meaning the fluctuations would be of order 10^{-2} today. These fluctuations are too small to make the large scale structure (LSS) that we observe today, together with galaxies, stars, planets and human beings. The problem is that only at recombination with the formation of neutral Hydrogen did baryons become charge neutral. Before this, due to electromagnetic forces, matter could not have clustered together to form the necessary gravitational wells. In order to explain the presence of the LSS, it is proposed that dark matter was present in the very early universe and decoupled from the plasma well before the last scattering. This would allow sufficient time for the dark matter to clump together to form the deep potential wells for the baryonic matter to fall in to. It is hypothesised to be non-baryonic matter because it must not interact with electromagnetic radiation, in agreement with the dark matter inferred in galaxies and galaxy clusters. [24]

There is a third argument based on the CMB properties, that points to a substantial fraction of missing mass-energy density in the Universe. Firstly, through General Relativity we know that mass curves spacetime and the curvature of the Universe is determined by the density parameter Ω, which is the energy density of the Universe weighted by the critical energy density. This means a flat Universe has $\Omega = 1$. The location of the first peak of the CMB implies that $\Omega = 1$, so the Universe it flat. In general, a parameter X has a density ρ_X and a density parameter $\Omega_X = \rho_X/\rho_c$ where ρ_c is the critical density. The physical densities are therefore proportional to $\Omega_X h^2$ and are usually quoted as such. From calculations in the context of big bang nucleosynthesis, it is known that Ω_b must be much smaller than 1 in order to produce the observed amounts of primordial Hydrogen, Deuterium, Helium and Lithium. Thus, the bulk of the mass-energy of the Universe cannot be in the form of baryonic matter. The baryonic matter density $\Omega_b h^2$ and the total matter density $\Omega_m h^2$ can also be measured from the angular power spectrum from WMAP and are found to be

$$\Omega_b h^2 = 0.02260 \pm 0.00053 \quad \Omega_m h^2 = 0.1334^{+0.0056}_{-0.0055} \tag{1.2}$$

The first interesting thing to note about these measurements is the fact that there is still a large amount of missing mass-energy to reach $\Omega = 1$. This corresponds to the so-called dark energy. If dark energy is simply a Cosmological constant Λ whose contribution does not vary with cosmic time, then it is measured to be

$$\Omega_\Lambda = 0.728^{+0.015}_{-0.016} \tag{1.3}$$

The Cosmological constant represents a uniform energy density that is found throughout the Universe which acts as a repulsive force, causing the expansion of the Universe to accelerate, as observed using supernova type 1a. The nature of dark energy is still not fully understood and is part of an active area of research. This thesis, however, will focus on dark matter; baryons do not make up 100% of the total observed matter, in fact they only make up approximately 15% by these estimates. These estimates have been confirmed by later surveys such as Planck [25] and data from the SDSS [26]

1.1.4 Search for a dark matter particle

There have been many attempts to find a candidate for the dark matter particle. Prime dark matter candidates are the hypothesised WIMPs (Weakly Interacting Massive Particles) which were motivated by string theory and supersymmetry. Another candidate is the Axion which is motivated by the strong CP problem in nuclear physics. After decades of searches, however, none of these particles have been discovered.

Another constraint on the hypothetical particle is closely related to the CMB fluctuations and the formation of the LSS. To form the observed LSS at $z = 0$ the dark matter particle must be "cold", meaning that the particle was non-relativistic when it decoupled from the primordial plasma. This meant that the particle moved slowly through the Universe, which allowed it form clumps through gravitational interactions leading to the observed LSS. If the particle was "hot" meaning it was relativistic when it decoupled, it would be moving too quickly preventing the formation of small structures. Hot dark matter may still be an acceptable candidate in combination with modified gravity theories, which would change the growth of perturbations and therefore the formation of the LSS. A hot dark matter candidate is a sterile neutrino with a mass of tens of eV, which is motivated by the observed neutrino flavour oscillations. There are several more exotic candidates which fit some of the requirements, but there has been no credible indication for any of them so far. [27] [28]

1.2 A History of MOND

1.2.1 The basics of MOND

The pieces of evidence presented for dark matter up to this point implicitly assume that standard gravitational physics, be it Newtonian or Einsteinian, holds in all cases including the regime of interest here associated with galaxy clusters. One theory that does not rely on these assumptions is that of MOdified Newtonian Dynamics (hereafter referred to as MOND) proposed by Mordehai Milgrom in 1983.[29] [30] [31] Milgrom posits that below a characteristic acceleration a_0 there

is a departure from the standard laws of gravity such that

$$g_N = g\mu\left(\frac{g}{a_0}\right) \tag{1.4}$$

where g_N is the Newtonian gravitational acceleration, g is the observed kinematic acceleration and μ is an interpolating function given by

$$\begin{cases} \mu\left(x = \frac{g}{a_0} \gg 1\right) \approx 1 \\ \mu\left(x = \frac{g}{a_0} \ll 1\right) \approx \frac{g}{a_0} \end{cases}$$

The interpolating function has the characteristic such that for large accelerations $g/a_0 \gg 1$, the Newtonian regime is restored. There is a well known family of interpolating functions that satisfy this criteria given by

$$\mu(x) = \frac{x}{(1 + x^n)^{(1/n)}} \tag{1.5}$$

where n are positive integers. Common forms of the function include the $n = 1$ case known as the simple function and $n = 2$ known as the standard function. Note that the exact form of the interpolating function does not drastically change the results, it only matters that it satisfies the criteria in the different limits. It is common to apply the MOND formula in a slightly different way, by rearranging Equation 1.4 by making the transformation $\nu = \mu^{-1}$

$$g = g_N \nu\left(\frac{g_N}{a_0}\right) \tag{1.6}$$

where this inverse interpolating function ν has the properties

$$\begin{cases} \nu\left(\frac{g_N}{a_0} \gg 1\right) \approx 1 \\ \nu\left(\frac{g_N}{a_0} \ll 1\right) \approx \left(\frac{g_N}{a_0}\right)^{-1/2} \end{cases}$$

The small acceleration regime of $g/a_0 \ll 1$ is known as the deep MOND limit (DML) where the departure from standard physics occurs. The motivation behind the DML is to require that the rotation curve of a finite galaxy becomes asymptotically flat as observed. This is immediately obtained from MOND if we consider the

29

DML regime where

$$g_N = \frac{g^2}{a_0} \tag{1.7}$$

At large distances from a mass distribution, the monopole term dominates the gravitational field g_N so it can be expressed using Newton's gravitational law

$$g_N = \frac{GM}{r^2} \tag{1.8}$$

where M is the total mass of the object. If we assume the object moves in a circular orbit, then $g = v^2/r$ and Equation 1.7 becomes

$$\frac{GM}{r^2} = \frac{v^4}{r^2 a_0} \tag{1.9}$$

Remarkably the radial dependence disappears which gives the asymptotically flat rotation curve as needed. This equation can be rewritten to give

$$v^4 = GMa_0 \tag{1.10}$$

Note that this is occasionally written in the literature as $v^4 = M\mathcal{A}_0$, having defined $\mathcal{A}_0 = Ga_0$ for convenience. The DML originates from a generalized theory of gravitational dynamics and so has constants G, a_0 and masses. A spacetime scale invariance is applied to the equations of motion meaning that the dynamical evolution is invariant under $(t, \boldsymbol{r}) \to \lambda(t, \boldsymbol{r})$ as $\lambda \to \infty$. Since $\lambda \to \infty$, this means that the accelerations g scale as $g \to g/\lambda \to 0$, meaning the deep MOND limit requirement of $g \ll a_0$ is satisfied. The constants of the theory are not affected by the scaling but equivalently the DML can be achieved by only scaling the constants.

1.2.2   MOND as modified gravity

Up to this point, only the equations of motion have been considered. However the more fundamental underlying action should be discussed. The Newtonian non-relativistic action for a system of particles interacting with gravity is given by

$$S = S_\phi + S_K + S_{int} = -\frac{1}{8\pi G} \int d^3 r (\vec{\nabla}\phi)^2 + \sum_i \frac{1}{2} m_i \int dt v_i^2 - \int d^3 r \rho(\vec{r})\phi(\vec{r}) \tag{1.11}$$

30

This first term in the action S_ϕ is associated with the gravitational potential ϕ, the second is that of the kinetic energy of the individual particles of the system, and the third represents the interaction term. If the S_ϕ term is changed then the gravitational law is changed and so the modified gravity theory is achieved in the non-relativistic regime, as described in Bekenstein and Milgrom [32]. If instead the S_K term is modified, then the gravitational law is unchanged but Newton's second law is changed and we have the modified inertia theory, as described in Milgrom [33]. If S_{int} are changed then both the gravity and inertia is changed.

I will now focus on the modified gravity theory of Bekenstein and Milgrom [32]. This was the first full fledged MOND theory and is often referred to as AQUAL from AQUAdratic Lagrangian. The modification of the action would be of the form

$$S_\phi = -\frac{1}{8\pi G} a_0^2 \int d^3 r F\left(\frac{(\vec{\nabla}\phi)^2}{a_0^2}\right) \tag{1.12}$$

where F is a dimensionless function. If the Principle of Least Action is applied, then we get an equation that is the non-linear generalization of the Newton–Poisson equation

$$\vec{\nabla} \cdot \left[\mu\left(\frac{|\nabla\phi|}{a_0}\right)\nabla\phi\right] = 4\pi G\rho \quad \text{where} \quad \mu(x) = \frac{dF(x^2)}{dx} \tag{1.13}$$

Since this is derived from an action, it can be demonstrated to satisfy all the necessary conservation laws. This equation can be analytically solved given suitable boundary conditions and high symmetry, i.e. spherical symmetry to yield Milgrom's law as seen in Equation 1.4

$$g_N = g\mu\left(\frac{g}{a_0}\right) = \frac{g^2}{a_0} \tag{1.14}$$

where $g = \nabla\phi$. It is now useful to point out that a modified-gravity theory in the DML corresponds to a theory that is conformally invariant, meaning we can derive useful analytic results, the first being a Virial relation. In general the Virial theorem is given by the Virial $\mathcal{V}$

$$\mathcal{V} = -\sum_i \boldsymbol{r}_i \cdot \boldsymbol{F}_i \tag{1.15}$$

31

which can be rewritten using the fact that the force F_i is $m_i\nabla\phi(r_i)$

$$\mathcal{V} = -\sum_i m_i \boldsymbol{r}_i \cdot \ddot{\boldsymbol{r}}_i \tag{1.16}$$

and using the chain rule of differentiation gives

$$\mathcal{V} = -\frac{1}{2}\frac{d^2}{dt^2}\sum_i m_i \boldsymbol{r}_i^2 + \sum_i m_i \dot{\boldsymbol{r}}_i^2 \tag{1.17}$$

The second derivative term vanishes for systems that remain bound over a long time and so the remaining term forces the Virial theorem to become

$$\mathcal{V} = 2E_k = M < \boldsymbol{v}^2 > \tag{1.18}$$

In order to get the explicit equation, I refer to Milgrom [34] where he defines the Virial integral as

$$\mathcal{V} = -\int d^3r \rho \boldsymbol{r} \cdot \boldsymbol{g} \tag{1.19}$$

using the expression for the divergence of the stress energy tensor of the gravitational field $\vec{\nabla} \cdot \boldsymbol{P} = \rho \boldsymbol{g}$

$$\mathcal{V} = -\int d^3r \boldsymbol{r} \cdot (\vec{\nabla} \cdot \boldsymbol{P}) \tag{1.20}$$

and using a vector identity and the trace property of P

$$\mathcal{V} = -\int d^3r \vec{\nabla} \cdot (\boldsymbol{P} \cdot \boldsymbol{r}) + \int d^3r Tr(\boldsymbol{P}) \tag{1.21}$$

The full workings out can be found in Milgrom [34] but these integrals are given by

$$\mathcal{V} = \frac{2}{3}M(MGa_0)^{1/2} + \frac{1}{4\pi G}\int d^3r[2\nu g_N^2 - \frac{3}{2}a_0^2\mathcal{Q}] \tag{1.22}$$

M here is the total mass of the system and $\mathcal{Q}$ is a parameter which in the DML is independent of mass and size of the system and is of order unity. In the DML $a_0^2\mathcal{Q} = 4/3\nu g_N^2$ and so the volume integral disappears, which gives the final expression for the Virial theorem in MOND

$$\mathcal{V} = \frac{2}{3}M(GMa_0)^{1/2} \tag{1.23}$$

32

or more formally, for any isolated DML system of point-like masses m_i in a steady-state equilibrium, the Virial equation is

$$\sum_i \boldsymbol{r}_i \cdot \boldsymbol{F}_i = -M(GMa_0)^{1/2}\mathcal{Q} \tag{1.24}$$

with

$$\mathcal{Q} = \frac{2}{3}\left(1 - \sum_i q_i^{2/3}\right) \quad \text{and} \quad q_i = \frac{m_i}{M} \tag{1.25}$$

As well as the Virial theorem, the expression for the two-body force can be determined using the above equation, rewritten for clarity

$$-\sum_i \boldsymbol{r}_i \cdot \boldsymbol{F}_i = \frac{2}{3}(Ga_0)^{1/2}\left[\left(\sum_i m_i\right)^{3/2} - \sum_i m_i^{2/3}\right] \tag{1.26}$$

so it is clear from this that in the DML the two-body force for two masses m_1, m_2, a distance r apart the force is

$$F(m_1, m_2, r) = \frac{2}{3}\frac{(Ga_0)^{1/2}}{r}[(m_1 + m_2)^{3/2} - m_1^{3/2} - m_2^{3/2}] \tag{1.27}$$

1.2.3 MOND as modified inertia

The previous Section was considering MOND as modified gravity but equally we can consider MOND as modified inertia which amounts to modifiying S_K from equation 1.11. This must obey as $a_0 \to 0$, the action goes to the standard Newtonian action, and for the DML as $a_0 \to \infty$ then the action must go as $S_k \propto a_0^{-1}$ to achieve the asmyptotic flat rotation curves. The action must therefore change to be $S_k[\vec{r}(t), a_0]$, i.e. a functional of the particle trajectory as well as a_0 dependent. This can be done by modifying the particle equation of motion such that a test particle of mass m would experience a force $\boldsymbol{F}(t)$ given by

$$\boldsymbol{F}(t) = m\boldsymbol{A}[\boldsymbol{r}(t), t, a_0] \tag{1.28}$$

where A is a functional of the full particle trajectory such that as $A[(\boldsymbol{r}(t), t, a_0) \to 0] \to \boldsymbol{a}$ and $A[(\boldsymbol{r}(t), t, a_0) \to \infty] \to \boldsymbol{q}[\boldsymbol{r}(t), t]$ as required. If we apply this force to

33

circular orbits the expression for the velocity curve is given by

$$\frac{v^2}{r}\mu\left(\frac{v^2}{ra_0}\right) = \frac{d\phi}{dr} \tag{1.29}$$

ϕ is the Newtonian potential. In the DML this is

$$\frac{v^4(r)}{r^2a_0} = -\frac{d\phi}{dr} \tag{1.30}$$

which leads to the modified inertia Virial relation for disk galaxies

$$< v^2 >^2 = \frac{4}{9}GMa_0 \tag{1.31}$$

Both the modified inertia and modified gravity formulations of MOND achieve the asymptotic flat rotation curves through different means.

1.2.4 Significance of a_0

It is clear that the constant a_0 is integral to the outlined dynamics. The numerical value has been determined by a number of independent methods which match theory to data and they all turn out to be in good agreement with each other. The current best value is

$$a_0 = 1.2 \pm 0.02 \, \text{x} \, 10^{-10} \, ms^{-2} \tag{1.32}$$

The first method that was used to determine a_0 was fitting rotation curves, the connection being clear from Equation 1.10 as outlined in Milgrom [30]. Further investigations were made in fitting rotation curves keeping a_0 as a fixed parameter and as a free parameter, which both produced consistent results. [35][36]

Equation 1.10 for the velocity is clearly related to the Tully Fisher relation, which relates the luminosity to the velocity by $v^4 \propto L$. Replacing $M = \Upsilon L$ in the velocity equation, where Υ is the mass to light ratio, the Tully Fisher relation is obtained $v^4 = G\Upsilon a_0 L \propto L$. It is one of the great successes of MOND that the Tully-Fisher relation occurs naturally. In the ΛCDM context, the relation must emerge empirically by fitting a straight line in logspace from $log(M_b) = \alpha log(v) - log(\beta)$. The slope α was best fit to be 4 which constrains the normalization β to be $1/Ga_0$, where a_0 is the MOND acceleration scale. This relation does not arise naturally

through ΛCDM which predicts a slope of $\alpha = 3$ and $\beta = 10 f_V^3 G H_0$. f_V is a phenomenological parameter that is required to be approximately 1.3. Even using this f_V parameter, the values for α and β do not accurately fit the observed relation.

In Milgrom [30], a value for a_0 was determined through this TF by using the ratio $(v^4/L)/(M/L)$ from a sample of galaxies and it was found that $a_0 = 1.9$x$10^{-10} m s^{-2}$ with a reported error of a factor of 2. In this same vein, Milgrom plotted $log(M)$ vs $log(v)$ and in determining the intercept found a value of a_0 to be 1.5x$10^{-10} m s^{-2}$ also with an uncertainty of a factor of 2. Modern, independent measurements of a_0 give the consistent value of 1.2x$10^{-10} m s^{-2}$ with uncertainties of the order of 10-20%. [37]

In addition to these astrophysical determinations of a_0, there are also cosmological connections or numerical coincidences. One of them is that $a_0 \approx c H_0$ where c is the speed of light and H_0 is the Hubble constant today. The second cosmological connection is $a_0 \approx c(\Lambda/3)^{1/2}$ where Λ is the cosmological constant. This is relevant because a theory gains greater credibility when its constants can be expressed in relation to pre-existing constants. This further adds credibility because it indicates that the internal dynamics of local systems could be related to the state of the Universe as a whole and could be responding to these changes. Since it is related to H_0 which changes over time, perhaps a_0 will change over time meaning the dynamics and limits imposed by a_0 will change. The relation to Λ however implies that a_0 could be a veritable constant as Λ is not time dependent. Whatever the case may be, this suggests that the cosmological acceleration parameters appear in the local dynamics in systems much smaller than the Universe. [29] [30] [31] [38] [39] [40] [41] [42] [43] [44] [45] [46]

1.2.5 External Field Effect

The Milgromian dynamics presented in the previous Sections were derived under the assumption that galaxies and/or galaxy clusters are isolated systems and that their environments had no effect on them. This is of course not true, there are no completely isolated systems in the universe. In Newtonian dynamics, the internal dynamics of a system are independent of its surroundings or the external field in which it resides. This is in fact a fundamental principle in General Relativity, known as the Strong Equivalence Principle, which states that the outcome of any

local experiment in a freely falling laboratory is independent of the velocity of the laboratory and its location in spacetime. MOND however breaks this principle due to its non-linearity. MOND is concerned with the total gravitational acceleration with respect to some frame, meaning that MOND only comes into effect when both the internal g and the external g_e gravitational acceleration are less than the a_0 threshold: $g_e < g < a_0$. Equation 1.4 is technically only correct in isolation. For non-isolated systems, the so-called external field effect (EFE) should be taken into account. In general, accounting for the EFE requires numerical 3D computations that solve the modified Poisson equation of MOND. To a zeroth order approximation, the EFE can be analytically calculated considering a 1D equation in which the accelerations are summed in modulus as if the acceleration vectors always have the same direction. This gives the following equation

$$g_N = g_\mu \left(\frac{g + g_e}{a_0} \right) + g_e \left[\mu \left(\frac{g + g_e}{a_0} \right) - \mu \left(\frac{g_e}{a_0} \right) \right] \tag{1.33}$$

Analogous to Equation 1.6, this can be rearranged for g using the inverse of the interpolating function ν

$$g = g_N \nu \left(\frac{g_N + g_{Ne}}{a_0} \right) + g_{Ne} \left[\nu \left(\frac{g_N + g_{Ne}}{a_0} \right) - \nu \left(\frac{g_{Ne}}{a_0} \right) \right] \tag{1.34}$$

In the above equations, g is the observed or internal gravitational acceleration, g_N is the Newtonian gravitational acceleration, g_e is the MOND external gravitational acceleration and g_{Ne} is the Newtonian external gravitational acceleration. g_{Ne} is relatively easy to calculate because Newtonian gravity is linear, so one can consider the gravitational field from N point masses (galaxies and/or galaxy clusters) in the vicinity of a target of interest, then simply sum up the Newtonian gravitational fields in a vectorial sense to obtain g_{Ne}. g_e is more complicated to determine because MOND is a non-linear theory.

1.3 Galaxy Clusters

Galaxy clusters are the largest virialized structures in the Universe. They reside at the intersection of cosmology and astrophysics, making them exceptional research

environments to examine theories associated with gravitational physics, as is the case in this thesis. As pointed out in Sections 1.1.1 and 1.1.2, the history of dark matter is closely related to galaxy clusters. In particular, it was through observations of the hot ICM that precise mass estimates were made, contributing to the evidence for mass discrepancies in the Universe. The hot ICM contains ionized gas and so the charged particles are accelerated and deflected by other charged particles, causing the particle to lose kinetic energy in the form of the bremsstrahlung radiation emitting in the X-rays.

There is also the production of X-rays through inverse Compton scattering. This occurs when a high-energy electron collides with a low-energy photon causing the scattered photon to gain energy at the expense of the electron, which loses energy resulting in the production of X-ray photons. This is the mechanism by which the Sunyaev Zeldovich (SZ) effect operates. In particular the SZ effect is due to the high energy electrons in the ICM interacting with CMB photons, causing them to gain energy therefore shifting to higher frequencies. The magnitude of this distortion in the CMB can be used to infer properties of the galaxy cluster. These intriguing observations ignited a surge of curiosity in the field of galaxy cluster formation and evolution.

The current theory on cluster formation starts from the fact that at very early times, the Universe had quantum fluctuations which are modelled by fluctuations in a fluid in a gravitational field. The fluctuations correspond to peaks and troughs in the fluid which is the primordial density field. The fluctuations are described by the density contrast field $\delta(\boldsymbol{x})$ as

$$\delta(\boldsymbol{x}) = \frac{\rho(\boldsymbol{x}) - \bar{\rho_m}}{\bar{\rho_m}} \tag{1.35}$$

where ρ_m is the average mass density in the Universe and $\rho(\boldsymbol{x})$ is the density field at point $\boldsymbol{x}$. The density field is assumed to be a homogeneous and isotropic random Gaussian field, which means it can be described by its power spectrum $P(k)$ as a function of the wavevector k and variance of σ^2. This is described in Fourier space for mathematical convenience. At early times, the growth of the fluctuations is linear according to a power law of the form $P(k) \propto k^\alpha$. As the fluctuations grew, the gravitational potentials increased and started to accrete matter. As mentioned in Section 1.1.3, it is theorised that dark matter decoupled first in order to form

the necessary gravitational wells. These are referred to as dark matter halos. As these halos formed, they began to merge with other halos to form massive halos for the baryonic matter to fall into. With this, the Universe continued to evolve until the gravitational interactions grew to a point where they could no longer be described by the linear regime. There was then a transition to the non-linear regime, which roughly corresponds to the formation of galaxies. These structures evolved under the influence of gravity to merge and gradually assemble in larger structures, known as galaxy clusters. This process is known as hierarchical structure formation; gravitational interactions amplify the fluctuations until small-scale structures collapse to serve as seeds for larger structures to grow from. This is also known as the bottom-up formation scenario where smaller structures lead to larger ones.
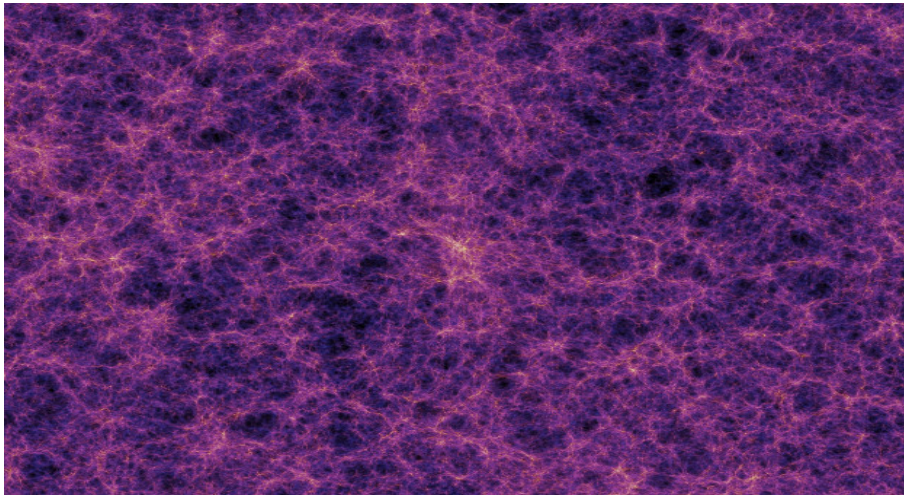
Figure 1.5: The result of a N-body high-resolution simulation dubbed the Millennium Simulation. The simulation included N = 2160^3 particles, evolving from redshift $z = 127$ to now $z = 0$, in a cubic region with $500h^{-1}$ Mpc sides. The image is largely homogeneous but there are filaments which surround large voids. The nodes of these filaments are where the galaxy clusters reside. [4]

Filaments are formed as a result of hierarchical structure formation. These are massive thread-like structures that connect galaxy clusters and superclusters forming something known as the Cosmic Web, which ultimately defines the structure of the Universe. A simulation of this structure can be seen in Figure 1.5. These filaments formed the paths that matter would flow down toward the high gravitational potential well. Matter continues to flow along the filaments causing them to merge and accrete even more, leading to the growth and thickening of the filaments.

It is along these filaments where the intercluster gas is contained, and it is at the intersection of filaments where galaxy clusters form.

The majority of the baryonic matter is contained in the ICM in the form of diffuse gas. With the exception of quasars, galaxy clusters are the most luminous X-ray emitting extra galactic objects meaning that this gas is relatively easy to trace using X-rays. The total baryonic content of the gas and the stellar component is directly observable in clusters as outlined in Chapter 2. [47] [48] [49]

1.4   Aim and content of the thesis

The aim of this thesis is to investigate the dark matter problem using galaxy clusters, the largest cosmological structures in the Universe. The two frameworks that are discussed in this thesis are that of standard cosmology using Newtonian dynamics and Milgromian dynamics (MOND). I test both of these theories by attempting to model the observed gravitational acceleration measured from the clusters, and comparing and contrasting the successes and failures of such models.

The thesis is organised as follows:

- Chapter 2 describes the data that are used in the thesis. Section 2.1 describes the clusters that were chosen in the thesis. Section 2.2 outlines the collection and analysis of the data that was performed in order to obtain the desired observed gravitational acceleration to be used in the modelling. Section does the same for the baryonic gravitational acceleration.

- Chapter 3 presents the models that were chosen to be studied under Newtonian dynamics. I outline the fitting procedures and all the parameters that were used. In Section 3.7 I present the results of all the fits and discuss their successes using the BIC. I further discuss the NFW and Einasto models in the context of ΛCDM.

- Chapter 4 attempts to describe the observations in the context of Milgromian dynamics. The Chapter opens by discovering that MOND still requires a large amount of missing mass to reproduce observations. Through this investigation, the EFE as well as the presence of hydrostatic bias is discussed. Some models are presented and fit to the data as before. The BIC is applied to these models to determine the best fit. Some correlation tests were then performed on the best fit data.

- In Chapter 5 I discuss the results from Chapters 3 and 4 in the context of the dark matter problem in general. I discuss the successes and problems with both of the theories. I also discuss extensions to this thesis that could be investigated in the future.

2

Dataset - XCOP

2.1 The cluster sample

The data used in this thesis consists of 5 galaxy clusters. This data was obtained as part of the XMM-Newton cluster outskirts project (X-COP), using the X-ray Multi Mirror Mission (XMMNewton) X-ray telescope. The sample of clusters in the X-COP project was selected based on a number of selection criteria. The most fundamental one is a signal-to-noise (SNR) higher than 12 in the Sunyaev-Zeldovich (SZ) from the Planck satellite. [50] This survey aimed to combine the X-ray and SZ data in order to get a complete reconstruction of the clusters' properties out to large radii. The clusters were also required to have halo masses $M_{500} > 3 \times 10^{14} M_{\odot}$, redshift between 0.04-0.1, apparent size $\theta_{500} > 10$ arcmin and column density of $N_H < 10^{21} cm^{-2}$ along the line-of-sight. These criteria yielded 15 clusters; however 3 were excluded due to complex morphologies, leaving 12 clusters. Of these 12, 5 were selected in this thesis (A644, A1795, A2029, A2142, A2319) because they had additional measurements of the stellar mass distribution within the brightest cluster galaxy (BCG) and the satellite galaxies. These components were then used to compute the gravitational field from all the baryonic components: stars and gas in galaxies plus the hot ICM gas. The majority (90%) of the baryonic component consists of ICM gas while the remaining 10% is made of gas and stars in galaxies.

The selection criteria of these 5 galaxy clusters are shown in Table 2.1. Two of these clusters (A644 and A1795) are shown in Figure 2.1. These figures show composite images of the X-ray and Optical data overlayed on each other.

Table 2.1: Cluster properties

Cluster	z	SNR_{SZ}	M_{500} $[10^{14} M_\odot]$	θ_{500} [arcmin]	N_H $[10^{20} cm^2]$
A644	0.0704	17.3	7.55	16.82	7.5
A1795	0.0622	19.3	5.33	16.82	1.2
A2029	0.0766	23.2	8.36	16.08	3.2
A2142	0.090	28.4	8.51	13.92	3.8
A2319	0.0557	49.0	10.56	23.49	3.2
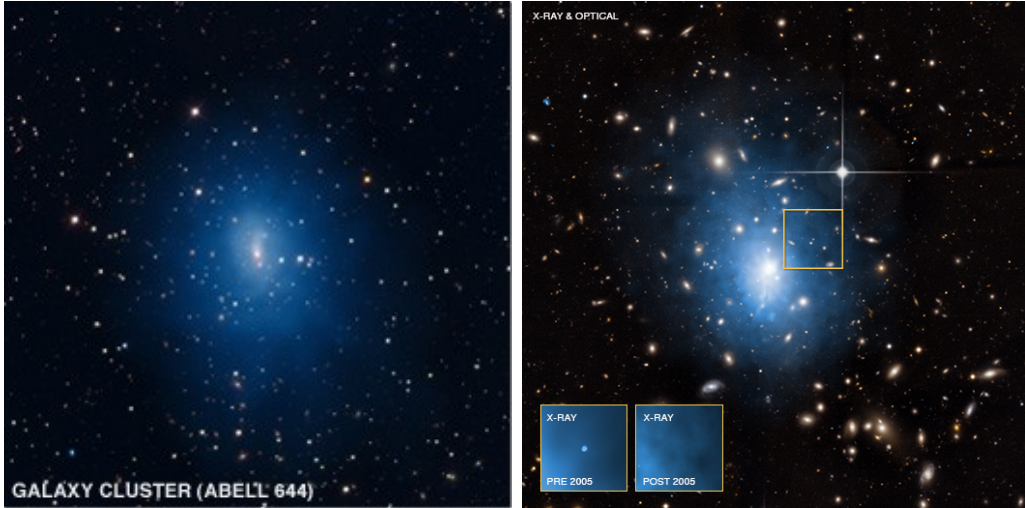
Figure 2.1: Clusters A644 (left) and A1795 (right). The data shown here is a mixture of X-ray data taken from the Chandra X-ray Observatory and optical data from the Sloan Digital Sky Survey. The X-ray data is shown in blue which is overlayed on to optical data. [5]

2.2 Observed gravitational field

The SZ data is described by a unit-less Comptonization parameter y which provides the integrated gas pressure P_{gas} along the line of sight l,

$$y = \frac{\sigma_T}{m_e c^2} \int_l P_{gas}(l) dl \tag{2.1}$$

where σ_T is the Thomson cross section, m_e the mass of the electron and c is the speed of light. The 3D pressure profiles are determined by binning the y-profiles and deprojecting them assuming spherical symmetry.

The observables in this dataset are therefore the electron pressure from the SZ data, the X-ray surface brightness profiles (proxy for the hot gas density) and the spectroscopic temperature from the X-ray data. From this data, the gas density, gas temperature and gas pressure are directly obtained, which are all related according to the ideal gas law given by

$$P_{gas} = \frac{k}{\mu m_p} \rho_{gas} T_{gas} \tag{2.2}$$

It is assumed that the hot gas is in hydrostatic equilibrium, so that the pressure gradient balances the gravitational attraction as

$$\frac{dP_{gas}}{dr} = -\rho_{gas} g_{obs} \tag{2.3}$$

where g_{obs} is the observed gravitational acceleration. In spherical symmetry this acceleration is given by GM_{tot}/R^2 in a Newtonian context and $g_N \nu(g_N/a_0)$ in a MOND context where $g_N = GM_{bar}/R^2$ is the Newtonian gravitational field sourced only by the observed baryons.

It is common in the literature to estimate the total "dynamical" mass profiles assuming Newtonian dynamics. Eckert et al. [6] used 3 distinct methods to estimate the mass profile; (i) parametric mass models - models which assumes a fixed functional form and a fixed number of parameters, (ii) forward fitting with parametric functions - a specific technique used to estimate the parameters of a parametric model from observed data, and lastly (iii) a nonparametric log-normal mixture reconstruction - models that don't make any assumptions about the data but only relies on the data itself to produce a model. The data used in this study are the non-parametric data in order to minimize assumptions.

To begin, the gas density profile is obtained from the 3D X-ray emissivity profile ϵ. Emissivity is the measure of an object's ability to emit energy, so it is a way of mapping out the distribution of hot ionized gas in the ICM of the cluster because it is proportional to the electron number density $\epsilon \propto n_e^2$. The emissivity can be described as the linear combination of a large number N_K of basis functions in the

form of King profiles Φ_k given by

$$\epsilon(r) = \sum_{k=1}^{N_k} \alpha_k \Phi_k(r) \tag{2.4}$$

where the King function is given by

$$\Phi_k(r) = \left(1 + \left(\frac{r}{r_{c,k}}\right)^2\right)^{-3\beta_k} \tag{2.5}$$

where r is the distance to the centre of the cluster, α_k is the model coefficients, β_k characterizes the shape of the density distribution and $r_{c,k}$ is a scale factor known as the core radius. Eckert et al. [6] set up a grid for a range of β and r_c values to provide a range of shapes for the surface brightness and at the same time the α_k coefficients are fit, providing a model for the observed surface brightness. The King functions are convenient because they are monotonously decreasing, which is the expected behavior of the emissitivity. Additionally it is advantageous to use the King functions because one can write analytically the relationship between the projected 2D profile and the deprojected 3D profile.

The observed temperature that is derived from the spectroscopic data is the temperature integrated along the line of sight weighted by the local emissitivity, which gives the expression

$$T_{spec}(r) = \frac{\int T_{3D} n_e^2 T_{3D}^{-3/4} dl}{\int n_e^2 T_{3D}^{-3/4} dl} \tag{2.6}$$

The spectroscopic temperature profile is obtained by measuring the energy and intensity of the X-rays at different wavelengths and comparing them to theoretical models. For convenience, the intrinsic 3D temperature profile is described as a linear combination of a large number N_g of log-normal functions

$$T_{3D}(r) = \sum_{i=1}^{N_g} G_i \frac{1}{\sqrt{2\pi\sigma_i^2}} \exp\left(-\frac{[ln(r) - ln(\mu_i)]^2}{2\sigma_i^2}\right) \tag{2.7}$$

Equation 2.4 for the emissitivity ϵ and Equation 2.7 are used in Equation 2.6 to fit the measured T_{spec} profile and infer the parameters that describe T_{3D}. The mean

values $\{\mu_i\}_{i=1}^{N_g}$ and standard deviations $\{\sigma_i\}_{i=1}^{N_g}$ of the Gaussians are set a priori in order to decrease the number of parameters to fit. For large values of N_g the model is essentially independent of μ_i and N_g, whereas the standard deviations act as effective smoothing scales. Eckert et al. [6] used $N_g = 200$, values for μ_i logarithmically spaced from the innermost to the outermost data points, and set the values of σ_i to the width of the nearest spectroscopic annulus. Once these are set, the model can be projected onto the line of sight and the normalizations $\{G_i\}_{N_g}^{i=1}$ of the Gaussians can be fit to the spectroscopic X-ray temperatures and SZ pressure profile combining Equations 2.2 and 2.1.

The observed gravitational potential can then be reconstructed by combining the 3D temperature and density profiles

$$g_{obs} = -\frac{k}{\mu m_p}\left(\frac{dT_{3D}}{dr} + \frac{T_{3D}}{\rho_{gas}}\frac{d\rho_{gas}}{dr}\right) \tag{2.8}$$

where k is Boltzman's constant, m_p is the proton mass and μ is the mean atomic weight of the plasma. The temperature T_{3D} is obtained in Equation 2.7 and so the temperature gradient is just the derivative of this equation given by

$$\frac{\partial T_{3D}}{\partial r} = \sum_{i=1}^{N_g} G_i \frac{1}{\sqrt{2\pi}\sigma_i^3}\exp\left(-\frac{[ln(r) - ln(\mu_i)]^2}{2\sigma_i^2}\right)\frac{ln(\mu_i) - ln(r)}{r} \tag{2.9}$$

The gas density gradient can be computed analytically from Equation 2.4 given the relation between emissitivity and gas density, so one has

$$\frac{\partial \epsilon}{\partial r} = \sum_{k=1}^{N_k} \alpha_k \frac{\partial \Phi_k}{\partial r} \tag{2.10}$$

The g_{obs} data is used extensively in the fits in Chapters 2 and 3.

2.3 Baryonic gravitational field

The computation of g_{bar} consists of the determination of the stellar gravitational field g_* and the gas gravitational field g_{gas}. To obtain the stellar mass distributions, data for the BCGs was obtained using r-band imaging. Eckert et al. [6] measured

the surface brightness profile projected on the sky, which was then deprojected to the true 3D mass density profile. This was done under the assumption of a constant stellar mass-to-light ratio Υ_*, which was estimated from stellar kinematic data. The BCG stellar kinematical models not only includes the stellar mass contribution but they also contains a supermassive black hole and a DM halo, whose mass was determined using weak lensing data, meaning the only fitting parameters were Υ_* and the stellar velocity anisotropy β_z. β_z and Υ_* were adjusted in the fit until the BCG profile fit the observed spectroscopic data. This Υ_* is then used to determine the stellar mass enclosed in different radii. The errors on M_{DM} and R_{200} from the lensing data are the main source of errors in this measurement therefore the errors on Υ_* and β_z were estimated by the 1σ errors on the lensing masses as well as a $\pm$ 10 % uncertainty for the concentration parameter. The uncertainties on the stellar mass profiles are therefore constant with radius.

The other stellar mass component is contained in the satellite galaxies. u-, g-, r- and i- band imaging was performed and the Υ_* were obtained using spectral energy distribution fitting. With the determination of the mass profiles, the acceleration profiles of the stellar components are easily calculated using Newtonian dynamics, so they are given by

$$g_{bar} = \frac{GM_{BCG}}{r^2} + \frac{GM_{sat}}{r^2} \tag{2.11}$$

The gravitational acceleration of the gas is computed assuming spherical symmetry and integrating the gas density over the cluster volume

$$M_{gas}(< r) = 4\pi \int_0^r \rho_{gas}(r')r'^2 dr' \tag{2.12}$$

where ρ_{gas} is obtained from Equation 2.3. The total baryonic component is $g_{bar} = g_{BCG} + g_{sat} + g_{gas}$. [6] [51] [52] [53]

3

Newtonian Dynamics

In this Chapter I fit the data to models that assume standard Newtonian dynamics along with a dark matter halo. I test a simple baryonic scaling model which assumes that the distribution of mass follows the distribution of light, as well as 5 different halo models. Pseudo-isothermal, Burkert and Lucky-13 are halo models motivated by fitting rotation curves of disk galaxies. They have no Cosmological basis. The other two models, NFW and Einasto, are motivated by N-body simulations of structure formation in a ΛCDM cosmology.

The models as well as the fitting parameters are described below. In all the models a common fitting parameter is the baryonic mass-to-light ratio Υ_{bar} which is assumed to be radially constant throughout the cluster. This fitting parameter accounts for uncertainties in the measured hot gas mass from the X-rays and the stellar mass from surface photometry. In the DM halo models, a common parameter is the scale radius r_s which is a characteristic radius defined by the scale at which the logarithmic slope of the density profile has value of -2. Naturally, there is a corresponding scale volume density given by $\rho(r = r_s) = \rho_s$.

In order to have direct comparison with ΛCDM cosmology, it is convenient to express the two parameters ρ_s and r_s in terms of the halo mass M_{200} and the halo concentration $C_{200} = R_{200}/r_s$ where R_{200} is the radius at which the density enclosed within this radius is 200 times the critical density of the Universe. The critical

density is defined using the first Friedmann equation

$$H^2 = \frac{8\pi G\rho}{3} - \frac{kc^2}{a^2} \tag{3.1}$$

where the flatness parameter k is set to zero making it a flat universe. Rearranging Equation 3.1 gives the equation for the critical density

$$\rho_c = \frac{3H^2}{8\pi G} = 2.7754 \times 10^{11} h^2 M_\odot \, \mathrm{Mpc}^{-3} \tag{3.2}$$

for $H_0 = 67.4$ km/s/Mpc. Since the boundary of a halo is not well defined, the mass is usually determined in terms of the critical density, such as M_{200} or any other fixed fraction of the critical density. The halo mass is then given by $M_{200} = 4/3\pi R_{200}^3 200\rho_c$, along with the circular velocity $V_{200} = 10C_{200}r_s H_0$. Lastly, for convenience, most models use an adimensional parameter $x = r/r_s$.

3.1 Bayesian fitting

The Bayesian approach of parameter estimation was used in this thesis, where a degree of belief is assigned to the parameters in the model. In Bayesian statistics, this degree of belief is quantified as a probability using Bayes' theorem

$$P(x|D) = \frac{P(D|x)P(x)}{P(D)} \tag{3.3}$$

where x are the parameters in question and D is the data. These expressions can also be expressed by

$$\mathrm{posterior} = \frac{\mathrm{likelihood} \times \mathrm{prior}}{\mathrm{evidence}} \tag{3.4}$$

The posterior is the probability of the model parameters given the data, the likelihood is the probability of observing the data given a set of model parameters, the prior is any previous knowledge on the model parameters and the evidence is the probability of the data. The evidence was not used in the fits as it only contributes a normalization of the posterior and does not contribute any useful information.

The posterior distribution is usually difficult to determine analytically, so we determine it numerically using Monte Carlo methods. This is an algorithm which

uses random sampling to simulate probability distributions. The exact Monte Carlo method used was a Markov chain Monte Carlo (MCMC), which is one in which there is no memory of the previous step, so it only depends on the current one. The starting points for these chains are very important because a poor starting point will produce a poor representation of the data. The parameter space was explored in logspace rather than linear space due to the large variations displayed in the data. The starting point in logspace for Υ_{bar} was preliminarily set to 1, and allowed to explore a large range of 0.25 dex in logspace or 58%. The starting points for the other parameters were set to be very broad in the initialization and were ocasionally adjusted after review of the plots of the convergence of the steps and the plots of the marginalized posterior probability distributions (the so-called "corner plots").

Υ_{bar} was assigned a lognormal prior because it is relatively well known what this parameter should be and how it should behave. The other parameters were assigned a uniform prior in order to not bias them by introducing strict probability distributions. The corner plots can be found at the end of the Chapter in Section 3.9. The 1D and 2D projections of the posterior probabilities of the parameters are displayed in the corner plots. The histograms on the diagonal are the 1D histograms for each of the parameters, which are obtained by marginalizing over the others. The solid red line in each represents the best fit value, along with the dashed lines on either side representing the 16th and 84th quantile. The other panels display the 2D projections of the posterior probability distributions for every combination of pairs of parameters. The red dot at the centre of the cross represents the best fit value.

3.2 Baryonic Scaling

The simplest model consists of solely scaling up the baryonic matter component to try to fit the observed acceleration. This involves only one free parameter; the baryonic mass-to-light ratio Υ_{bar}. This scaling model would correspond to a galaxy cluster where the DM closely follows the distribution of baryons, motivated by the fact that baryonic scaling works reasonably well for disk galaxies as demonstrated by Hoekstra et al. [54], Swaters et al. [55]. Intriguingly, as seen in Section 3.8.1, this model can somewhat reproduce the observed acceleration and mass profiles with only one free parameter.

3.3 Pseudo-Isothermal Profile

The pseudo-isothermal profile (pISO) [56] is given by

$$\rho_{pISO}(r) = \frac{\rho_s}{1 + (\frac{r}{r_s})^2} \tag{3.5}$$

This has the property of having a constant density at small radii $\rho(r \to 0) \to \rho_s$ and so it is commonly dubbed a "cored" profile. The enclosed mass is determined by integrating the density over the volume of a sphere of radius r, where the volume of the sphere is divided into infinitesimal shells of thickness dr with a surface area of $4\pi r^2$, so the integral is given by

$$M_{pISO}(< r) = \int_0^r 4\pi r'^2 \frac{\rho_s}{1 + (\frac{r'}{r_s})^2} \, dr' \tag{3.6}$$

$$= 4\pi \rho_s r_s^3 \left(\frac{r'}{r_s} - \arctan\left(\frac{r'}{r_s}\right) \right) \Big|_0^r \tag{3.7}$$

$$= 4\pi \rho_s r_s^3 (x - \arctan(x)) \tag{3.8}$$

Rather than fitting the observed enclosed mass density profile as is common in other cluster studies, it is preferred here to fit the observed acceleration profile g_{obs}. This means that g_{pISO} is needed instead of the mass, which is calculated by $g_{pISO} = V_{pISO}^2/r$ where the expected circular velocity of a test particle is given by

$$V_{pISO}(r) = \sqrt{\frac{GM_{pISO}}{r}} \tag{3.9}$$

$$= \sqrt{4\pi \rho_s r_s^3 (x - \arctan(x))} \tag{3.10}$$

We want to express the circular velocity in terms of V_{200} as given by

$$V_{200} = \sqrt{\frac{GM_{200}}{R_{200}}} \tag{3.11}$$

$$= \sqrt{4\pi \rho_s r_s^3 \left(\frac{R_{200}}{r_s} - \arctan\left(\frac{R_{200}}{r_s}\right) \right)} \tag{3.12}$$

$$\tag{3.13}$$

By dividing both sides of Equation 3.10 by V_{200} and by using the definition of $C_{200} = R_{200}/r_s$ gives the final expression

$$V_{pISO}(r) = V_{200}\sqrt{\frac{1 - \frac{\arctan(x)}{x}}{1 - \frac{\arctan(C_{200})}{C_{200}}}} \qquad (3.14)$$

This has fitting parameters C_{200} and V_{200} but the desired parameters are M_{200} and C_{200} which are related to the others by

$$V_{200} = (M_{200}10GH(z))^{1/3} \quad \text{and} \quad r_s = V_{200}/(10C_{200}H(z)) \qquad (3.15)$$

where:

$G = 4.3\mathrm{x}10^{-6}\,kpckm^2s^{-2}M_\odot^{-1}$ the gravitational constant in appropriate units

$H(z) = H_0(\Omega_m(1+z)^3 + \Omega_\Lambda)^{1/2}$

$H_0 = 0.0674kms^{-1}kpc^{-1}$ the Hubble constant in appropriate units

$\Omega_m = \rho_m/\rho_c = 0.315$ the matter density parameter

$\Omega_\Lambda = \rho_\Lambda/\rho_c = 0.685$ the dark energy density parameter

z : redshifts of the clusters

This g_{pISO} profile is fit along with the baryonic component g_{bar} to the g_{obs} so the last fitting parameter is the Υ_{bar}.

3.4   Burkert Profile

The same procedure is followed for the Burket profile [57] where the density profile is given by

$$\rho_{Burkert}(r) = \frac{\rho_s}{\left(1 + \frac{r}{r_s}\right)\left(1 + \left(\frac{r}{r_s}\right)^2\right)} \qquad (3.16)$$

and the enclosed mass is determined by performing the previous integral

$$M_{Burket}(r) = 2\pi\rho_s r_s^3\left(\frac{1}{2}\ln(1 + x^2) + \ln(1 + x) - \arctan(x)\right) \qquad (3.17)$$

51

And the rotational velocity, in terms of V_{200} is

$$V_{Burkert}(r) = V_{200}\frac{C_{200}}{x}\sqrt{\frac{\frac{1}{2}\ln(1+x^2)+\ln(1+x)-\arctan(x)}{\frac{1}{2}\ln(1+C_{200}^2)+\ln(1+C_{200})-\arctan(C_{200})}} \qquad (3.18)$$

3.5 Lucky13 Profile

The Lucky13 density profile [58] is given by

$$\rho_{130}(r) = \frac{\rho_s}{\left(1+\frac{r}{r_s}\right)^3} \qquad (3.19)$$

with an enclosed mass of

$$M_{130}(r) = 4\pi\rho_s r_s^3\left(\ln(1+x)+\frac{2}{1+x}-\frac{1}{2(1+x)^2}-\frac{3}{2}\right) \qquad (3.20)$$

leading to an expected circular velocity of

$$V_{130}(r) = V_{200}\sqrt{\frac{C_{200}\left(\ln(1+x)+\frac{2}{1+x}-\frac{1}{2(1+x)^2}-\frac{3}{2}\right)}{x\left(\ln(1+C_{200})+\frac{2}{1+C_{200}}-\frac{1}{2(1+C_{200})^2}-\frac{3}{2}\right)}} \qquad (3.21)$$

3.6 Navarro Frenk White Profile

The NFW density profile is one of the most common profiles used for dark matter halos. [59] The density profile is given by

$$\rho_{NFW}(r) = \frac{\rho_0}{\frac{r}{r_s}\left(1+\frac{r}{r_s}\right)^2} \qquad (3.22)$$

This profile implies a steep density increase in the inner region of the halo where $r \ll r_s$ and $\rho(r) \propto r^{-1}$. Formally, the density diverges to infinity for $r \to 0$, which is commonly referred to as the "cusp". As $r \to r_s$ the density profile becomes shallower and decreases as $\propto r^{-3}$. The enclosed mass profile is given by

$$M_{NFW}(r) = 4\pi\rho_s r_s^3\left(\ln(1+x)-\frac{x}{1+x}\right) \qquad (3.23)$$

leading to the rotational velocity of

$$V_{NFW}(r) = V_{200}\sqrt{\frac{C_{200}(\ln(1+x) - \frac{x}{1+x})}{x(\ln(1+C_{200} - \frac{C_{200}}{(1+C_{200})})}} \tag{3.24}$$

3.7 Einasto Profile

The Einasto density profile [60] is similar to the NFW profile except that it has an additional fitting parameter α which describes the inner slope of the profile. The density profile is given by

$$\rho_{Einasto}(r) = \rho_s \exp\left[-\frac{2}{\alpha}\left(\left[\frac{r}{r_s}\right]^\alpha - 1\right)\right] \tag{3.25}$$

The Einasto profile has the property that as $r \to 0$, $\rho(r) \propto$ constant and as $r \to \infty$ $\rho(r) \propto 0$. The shape of this transition is set by the parameter α. Typical values of α for a galaxy cluster are $0.2 < \alpha < 0.3$, which are motivated by fitting simulated DM halos in cosmological LCDM simulations. A value of $\alpha = 0.25$ [61] is fixed in the following fits for simplicity, so that the Einasto fits have the same number of free parameters as the other halo models. This also makes it easier to compare the models because Einasto and NFW profiles are quite different at the two extreme radii, but on the scales of interest for galaxy clusters they are relatively similar for $\alpha = 0.25$. This value for α is applicable for $z \simeq 0$ which is the approximate redshift of the clusters. The full α-redshift relation can be found in Dutton and Macciò [61].

The enclosed mass is given by

$$M_{Einasto}(r) = 4\pi\rho_s r_s^3 \exp\left(\frac{2}{\alpha}\right)\left(\frac{2}{\alpha}\right)^{-3/\alpha}\left(\frac{1}{\alpha}\right)\Gamma\left(\frac{3}{\alpha}, \frac{2}{\alpha}x^\alpha\right) \tag{3.26}$$

where

$$\Gamma\left(\frac{3}{\alpha}, \frac{2}{\alpha}x^\alpha\right) = \int_0^{\frac{2}{\alpha}x^\alpha} t^{\frac{3}{\alpha}-1}e^{-t}dt \tag{3.27}$$

is the incomplete Gamma function. The rotational velocity is given by

$$V_{Einasto}(r) = V_{200}\sqrt{\frac{C_{200}\Gamma\left(\frac{3}{\alpha}, \frac{2}{\alpha}x^\alpha\right)}{x\Gamma\left(\frac{3}{\alpha}, \frac{2}{\alpha}C_{200}^\alpha\right)}} \tag{3.28}$$

53

3.8 Results

The best-fit results are presented as follows: for the baryonic scaling model a single page shows all five galaxy clusters, while for the DM halo models each cluster has a dedicated page that compares the various models. The baryonic scaling profiles can be found in Figure 3.1 and the DM halo models in Figures 3.2 to 3.6. These two approaches are distinguished, because it is more relevant to compare the DM halo models to each other rather than to the baryonic scaling model. The rows of the plots from top to bottom show the different halo models in the same order as Sections 3.2 to 3.7, that is Psuedo Isothermal, Burkert, Lucky13, NFW and Einasto. The first column is the fitted acceleration profile, the second is the enclosed mass profile and the third is the corresponding circular velocity curve of a test particle. These three columns present the same data and best-fit model in a slightly different way. The first one, the acceleration, is the most physical because g_{obs} is what is actually measured by hydrostatic equilibrium. The second one, the enclosed mass, is commonly used in the cluster literature, however we note that this quantity is the "Newtonian dynamical mass" which may have no precise meaning in other gravitational theories. The third one, the circular velocity, allows direct comparison with the observed rotation curves of disk galaxies, in which the rotation speed is a good proxy of the circular velocity of a test particle. The posterior probability distributions from the MCMC fitting ("corner plots") are included in an appendix at the end of the Chapter. The results of the best fit parameters are displayed in Table 3.1.

Table 3.1: The best fit model parameters from the MCMC parameter estimation procedure. These values are quoted in base 10 logarithm with M_{200} in Solar mass units

		pISO	Burkert	Lucky13	NFW	Einasto
A644	$log(\Upsilon_{bar})$	0 ± 0.1	0 ± 0.1	0 ± 0.1	-0.1 ± 0.09	0 ± 0.1
	$log(M_{200})$	15.08 ± 0.01	14.77 ± 0.01	14.90 ± 0.1	14.97 ± 0.02	14.90 ± 0.01
	$log(C_{200})$	1.48 ± 0.02	0.41 ± 0.01	1.07 ± 0.01	$0.67\,^{+0.01}_{-0.02}$	0.66 ± 0.01
A1795	$log(\Upsilon_{bar})$	0 ± 0.1	0 ± 0.1	0 ± 0.1	0.02 ± 0.09	0 ± 0.1
	$log(M_{200})$	14.82 ± 0.01	14.50 ± 0.02	14.62 ± 0.01	14.70 ± 0.02	14.69 ± 0.02
	$log(C_{200})$	1.58 ± 0.02	0.43 ± 0.01	1.12 ± 0.01	$0.71\,^{+0.01}_{-0.02}$	0.70 ± 0.01
A2029	$log(\Upsilon_{bar})$	0 ± 0.1	0 ± 0.1	0 ± 0.1	0.13 ± 0.07	0 ± 0.1
	$log(M_{200})$	15.00 ± 0.01	14.73 ± 0.02	14.81 ± 0.01	$14.89\,^{+0.02}_{-0.03}$	14.90 ± 0.02
	$log(C_{200})$	1.57 ± 0.01	0.40 ± 0.01	1.11 ± 0.01	0.65 ± 0.02	0.67 ± 0.01
A2142	$log(\Upsilon_{bar})$	0 ± 0.1	0 ± 0.1	0 ± 0.1	$0.22\,^{+0.07}_{-0.08}$	0 ± 0.1
	$log(M_{200})$	15.06 ± 0.02	14.94 ± 0.03	14.94 ± 0.02	15.01 ± 0.04	15.05 ± 0.03
	$log(C_{200})$	1.31 ± 0.02	0.25 ± 0.01	1.31 ± 0.02	$0.39\,^{+0.03}_{-0.04}$	0.44 ± 0.02
A2319	$log(\Upsilon_{bar})$	0 ± 0.1	0 ± 0.1	0 ± 0.1	-0.37 ± 0.07	0 ± 0.1
	$log(M_{200})$	15.13 ± 0.01	14.91 ± 0.01	15.00 ± 0.01	15.10 ± 0.01	15.04 ± 0.01
	$log(C_{200})$	1.33 ± 0.01	0.31 ± 0.01	0.95 ± 0.1	0.54 ± 0.01	0.52 ± 0.01
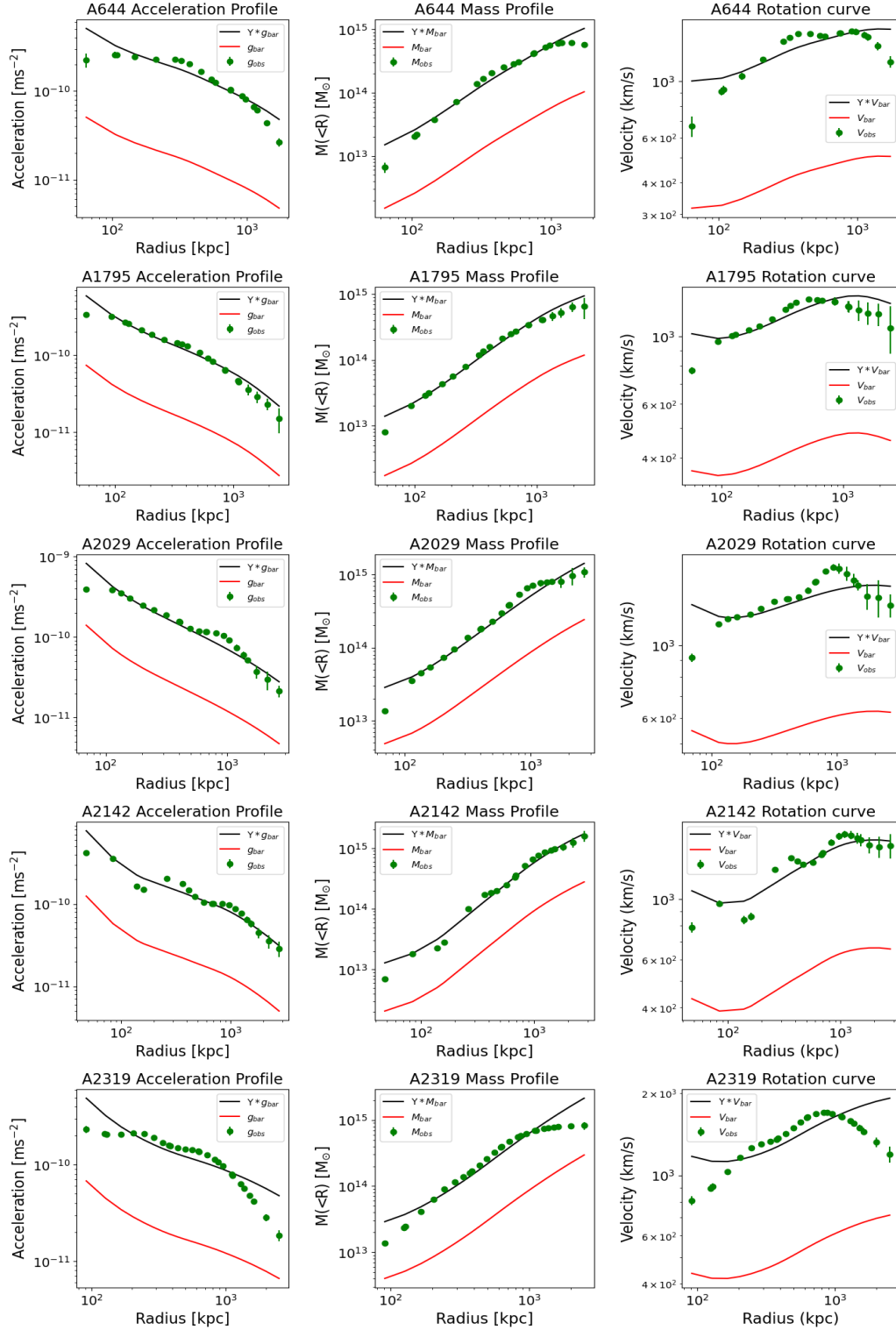
Figure 3.1: The baryonic scaling profiles. The green data points are the g_{obs} data, the red line is the g_{bar} data and the black line is the scaled g_{bar} data.
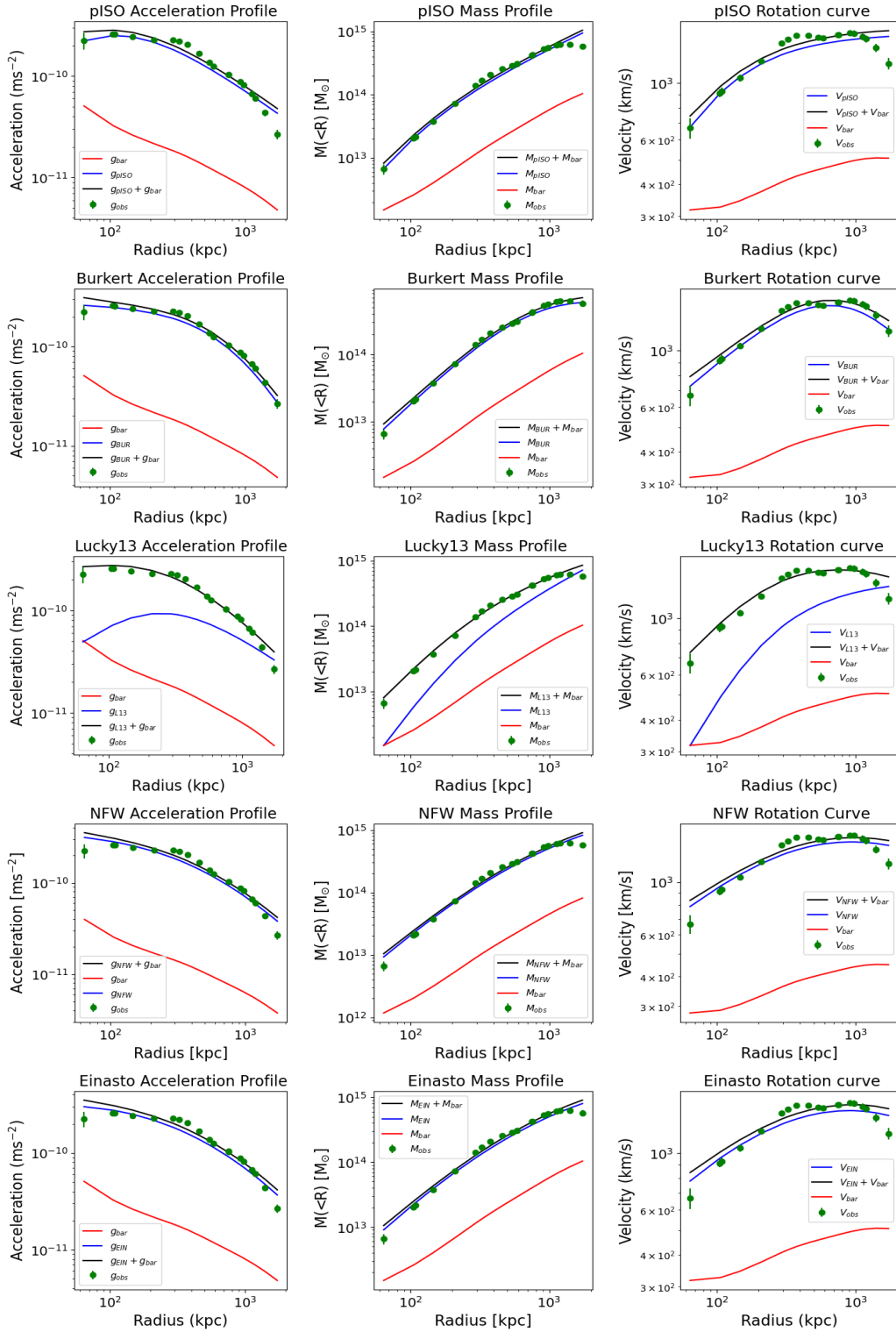
Figure 3.2: The A644 profiles. The green data points are the g_{obs} data, the red line is the g_{bar} data, the blue line is the halo gravitational acceleration profile only and the black line is the halo profile fit with the baryonic component
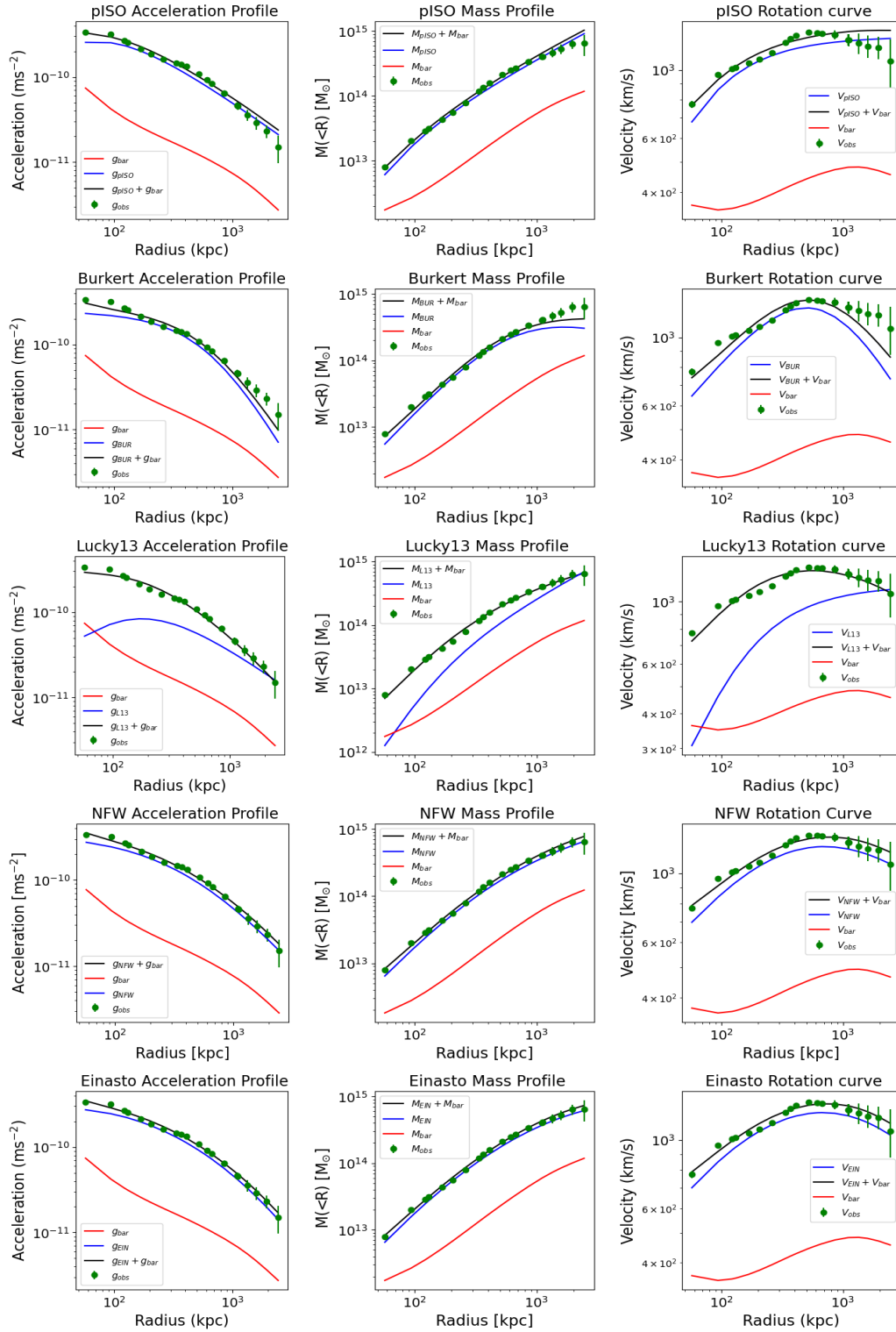
Figure 3.3: The A1795 profiles. The green data points are the g_{obs} data, the red line is the g_{bar} data, the blue line is the halo gravitational acceleration profile only and the black line is the halo profile fit with the baryonic component
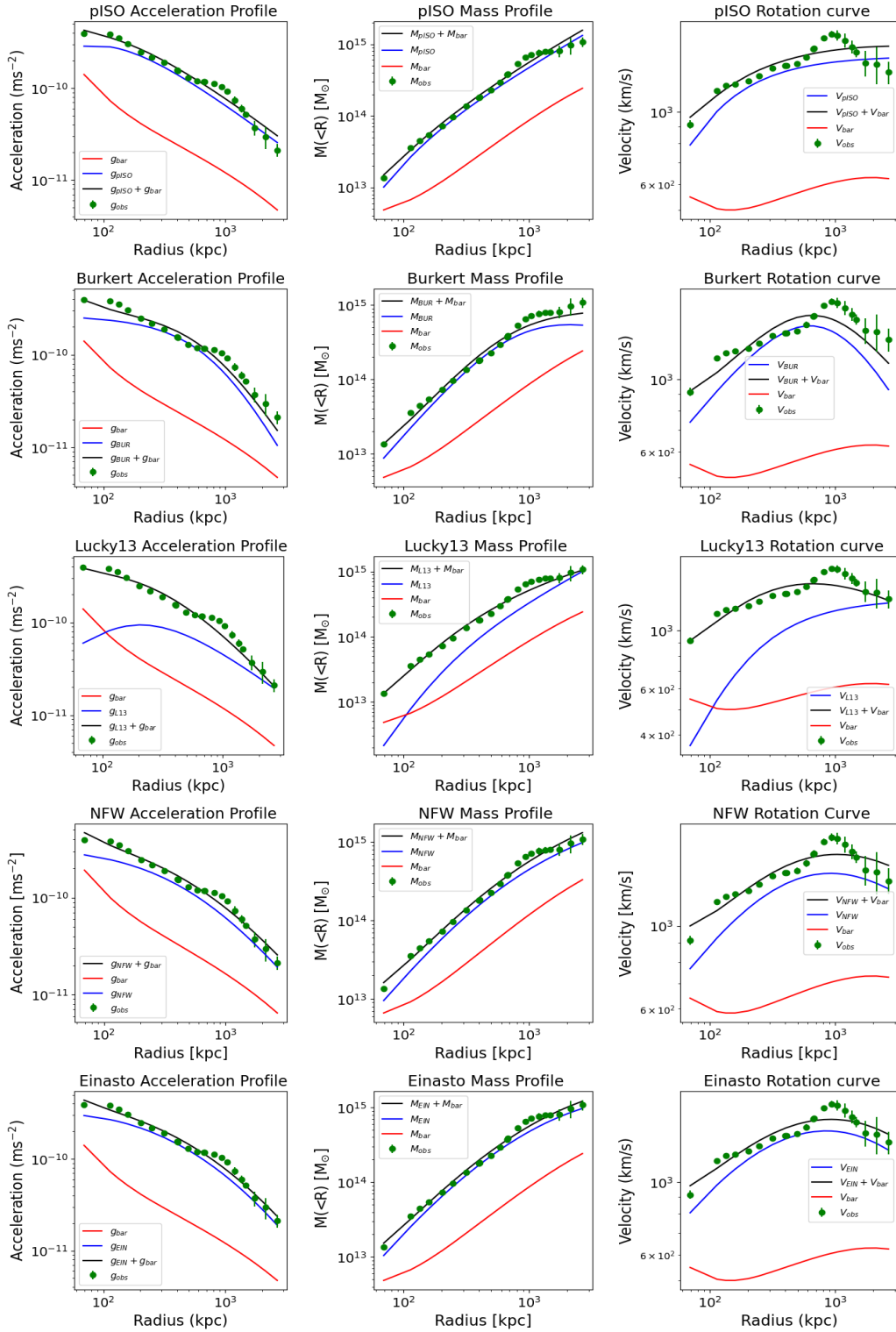
Figure 3.4: The A2029 profiles. The green data points are the g_{obs} data, the red line is the g_{bar} data, the blue line is the halo gravitational acceleration profile only and the black line is the halo profile fit with the baryonic component
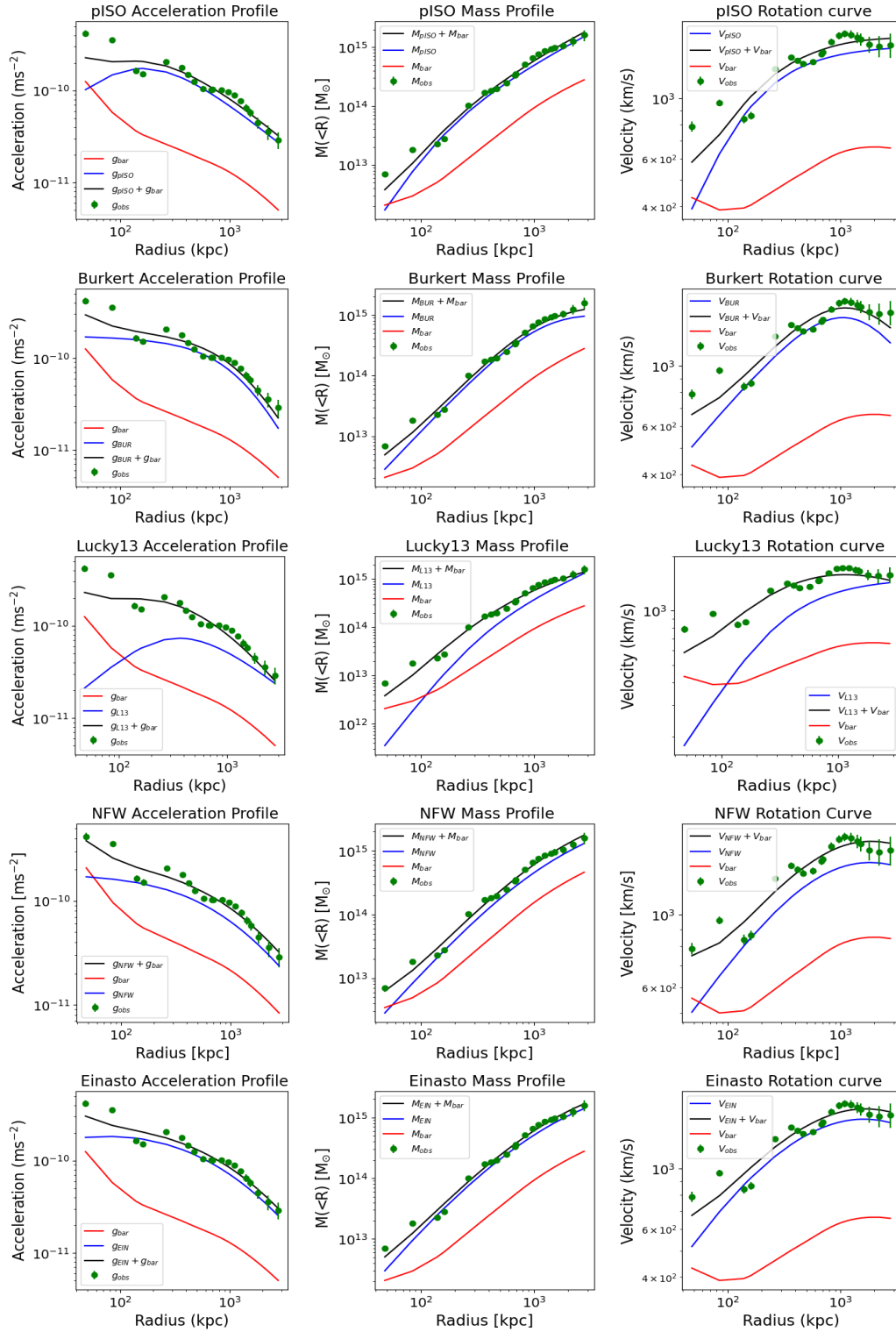
Figure 3.5: The A2142 profiles. The green data points are the g_{obs} data, the red line is the g_{bar} data, the blue line is the halo gravitational acceleration profile only and the black line is the halo profile fit with the baryonic component
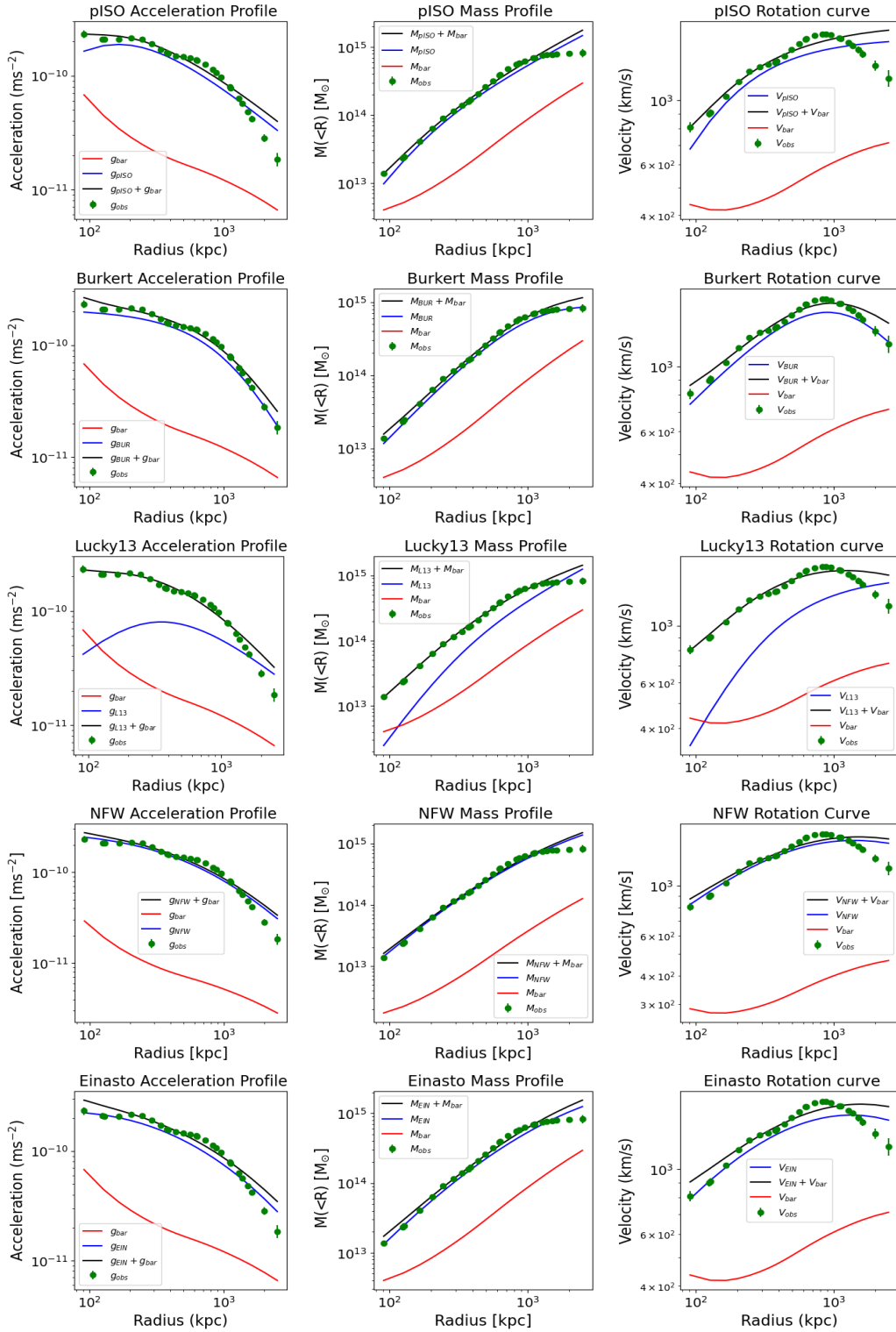
Figure 3.6: The A2319 profiles. The green data points are the g_{obs} data, the red line is the g_{bar} data, the blue line is the halo gravitational acceleration profile only and the black line is the halo profile fit with the baryonic component

3.8.1 Baryonic scaling

Figure 3.1 presents the results from the baryonic scaling model. Surprisingly, this simple model with only one free parameter provides a decent representation for most clusters. It is immediately apparent that some clusters are fit worse than others by this scaling, such as A644 and A2319. A more quantitative comparison on the effectiveness of the fits is discussed in the next Section. The Υ_{bar} value required for the scaling is reported in Table 3.2. It is unphysical to have values of Υ_{bar} as large as 5-10. However this simple exercise tells us that there is a correlation between the baryonic matter and the total mass. This could mean that the additional matter has a somewhat similar distribution as the baryonic matter.

There have been studies of spiral galaxies where their baryonic components, the HI gas and stellar discs, were arbitrarily scaled up to fit the observed rotation curve, providing relatively good fits. To explain these results it was proposed that there could be DM in the form of "dark" molecular gas distributed in a similar way as the HI component. However, this type of explanation is inconsistent with cosmological evidence for DM and would lead to serious problems with disk stability. [62] It has also been suggested that since the profiles of the baryonic components peak at different radii, perhaps the combination of these profiles produce the flat rotation curve almost by coincidence. [63] This scaling of total matter to baryonic matter has not been studied for clusters, but it is interesting that it seems to somewhat work on both galaxies and clusters scales, pointing to the fact that there could be some matter missing in the from of baryons. It is also possible that the underlying physics is incorrect as discussed in Chapter 4.

Table 3.2: The best fit baryonic scaling Υ_{bar} values in log and linear scale

Cluster	$log_{10}(\Upsilon)$	Υ
A644	$0.901^{+0.00387}_{-0.00389}$	$7.963^{+1.009}_{-0.991}$
A1795	$1.001^{+0.00520}_{-0.00527}$	$10.023^{+1.012}_{-0.988}$
A2029	$0.859^{+0.00280}_{-0.00283}$	$7.228^{+1.006}_{-0.994}$
A2142	$0.770^{+0.00379}_{-0.00379}$	$5.888^{+1.009}_{-0.991}$
A2319	$0.793^{+0.00578}_{-0.00590}$	$6.209^{+1.013}_{-0.987}$

3.8.2 Dark matter halos

Qualitatively, it is clear that some models provide better fits than others. It can be seen in the corner plots in Section 3.9, all of the 1D histograms are very close to Gaussians, meaning that the best-fit parameters are well determined. The same

can be said for the 2D distributions as they are mostly circular, except for some correlation between mass and concentration, which presents as a slightly skewed distribution rather than circular. This is to be expected as these two parameters are slightly degenerate and are closely related.

In general, if we look at the gravitational acceleration profile, there is a trend where the pseudo-isothermal profile and the Lucky-13 fits the inner radii well and not as well the outer radii, for example in cluster A2319. NFW, Einasto and Burkert on the otherhand do not fit the inner or outer radii well, but the intermediate regions of the profile do align with the data points. A more quantitative description of the fitting quality is provided in the next Section.

3.8.3 Model Comparison

The Bayesian Information Criterion (BIC) is a tool used in model comparison and selection. The model that is preferred by the BIC corresponds to the model that best describes the data. The BIC is based on the log-likelihood and so it does not require precise priors, which is advantageous to some Bayesian modelling where the priors are difficult to set or unknown. The BIC is given by

$$BIC = k \, log(n) - 2log(\mathcal{L}) \tag{3.29}$$

where k is the number of parameters in the model, n is the size of the data set and $\mathcal{L}$ is the maximum likelihood. The log-likelihood is calculated using the residuals and standard deviation of the residuals, which are then used in probability distribution function. In this case, the function used is the log probability density function of a normal distribution, which represents the likelihood of observing each residual value assuming a normal distribution with the determined standard deviation. The BIC values for all the clusters and models are included in Table 3.3.

Table 3.3: The BIC values of the various models

Cluster	Bary. scaling	pISO	Burkert	Lucky13	NFW	Einasto
A644	-818.901	-871.156	-867.518	-881.793	-849.792	-850.241
A1795	-916.646	-997.953	-970.218	-974.075	-995.547	-997.904
A2029	-937.825	-1023.906	-1001.076	-1011.908	-1007.909	-1015.248
A2142	-856.392	-877.590	-888.350	-877.528	-903.186	-891.138
A2319	-1175.567	-1271.152	-1271.439	-1285.22	-1253.668	-1241.997

We can compare the individual models on a cluster by cluster basis as seen in Table 3.3, or on average in Table 3.4. A more favorable model will have the smallest

Table 3.4: The average BIC values by model

Model	Average BIC
Baryonic scaling	-941.066
pISO	-1008.351
Burkert	-999.720
Lucky13	-1006.105
NFW	-1002.020
Einasto	-999.306

BIC and since these values are all negative the best fit model will have the largest negative number. This means that the best model was the pseudo-isothermal profile, followed by Lucky13, NFW, Burkert, Einasto and lastly is the baryonic scaling. It is clear even by eye that the baryonic scaling is the worst of the models, but as described in the previous section it is more intriguing that it can provide a reasonable fit. To compare the other 5 models we can use the table from Neath and Cavanaugh [64] because the BIC numbers are arbitrary on their own. If there are two models to compare M_1 and M_2 and their BICs are calculated to be B_1 and B_2, the difference is $\Delta_{12} = B_1 - B_2$ and this difference is quantified in Table 3.5.

Table 3.5: Strength of evidence by difference in BIC

Δ_{12}	Evidence to favor M_2 over M_1
0-2	Inconclusive
2-6	Positive
6-10	Strong
>10	Very strong

From Table 3.4 it is clear that all five of the halo models have very strong evidence for being better than the baryonic scaling model. According to Table 3.5, moreover, there is strong evidence that the pseudo-isothermal profile is a better model for the data than the Burkert, NFW and Einasto profiles, but the same cannot be said for the Lucky13, profile where there is just about positive evidence for the pseudo-isothermal profile being better than Lucky13. Thus, cored halo profiles such as pseudo-isothermal or Lucky-13 are strongly favoured with respect to the cuspy profiles such as NFW and Einasto.

This result is analogous to the long-standing "cusp-core problem" in galaxies. Cosmological simulations in ΛCDM have predicted the "cuspy" profiles. In reality, it seems that rotation curves of galaxies are better fit by the cored profiles. This is still a long-standing problem in the standard ΛCDM paradigm that has yet to

be solved, although there has been some suggestions put forward. The results from these fits suggest that clusters also prefer the cored profiles suggesting that the cusp-core problem may not be limited to the "small-scales" of galaxies but may apply to the largest scales of galaxy clusters. [65]

It is also relevant to compare the overall shape of each of the profiles of the clusters to each other. Some clusters have smooth profiles whereas some of them have irregularities. This makes model comparison slightly more complicated because some profiles will fit the anomalies in some of the data better, but these shapes may or may not be representative of clusters' equilibrium gravitational potential due to, for example, deviation from hydrostatic equilibrium. It would also be advantageous to have a larger number of clusters so that the anomalies would become clearer and would not skew the results as much.

3.8.4   Comparison with ΛCDM scaling relations

The NFW and Einasto profiles are motivated by cosmological simulations of structure formation in ΛCDM. [61] In addition to predicting the halo density profiles, these simulations also predict a tight scaling relation between the halo mass and the halo concentration. It is therefore important to check whether the best fit M_{200} and C_{200} parameters of the clusters lie on the predicted mass-concentration relation.

This relationship links the halo mass M_{200} to the concentration index C_{200}, as defined in the opening of Section 3. In Dutton and Macciò [61] the authors fit NFW and Einasto halos separately over 5 decades of masses, from dwarf galaxies to massive clusters, as well as a wide range of redshifts from $0 < z < 5$, and determined a concentration-mass relation. The general relation is given by

$$log_{10}C = a + blog_{10}\Big(\frac{M}{10^{12}h^{-1}M_\odot}\Big) \tag{3.30}$$

The best fit slope and intercept for NFW was determined to be

$$b = -0.101 + 0.025z \tag{3.31}$$

$$a = 0.520 + (0.905 - 0.520)\exp(-0.617z^{1.21}) \tag{3.32}$$

and for Einasto

$$b = -0.130 + 0.029z \tag{3.33}$$

$$a = 0.459 + (0.977 - 0.459)\exp(-0.490z^{1.303}) \tag{3.34}$$

This relation is plotted in Figure 3.7 for $z = 0$, where the shaded grey regions
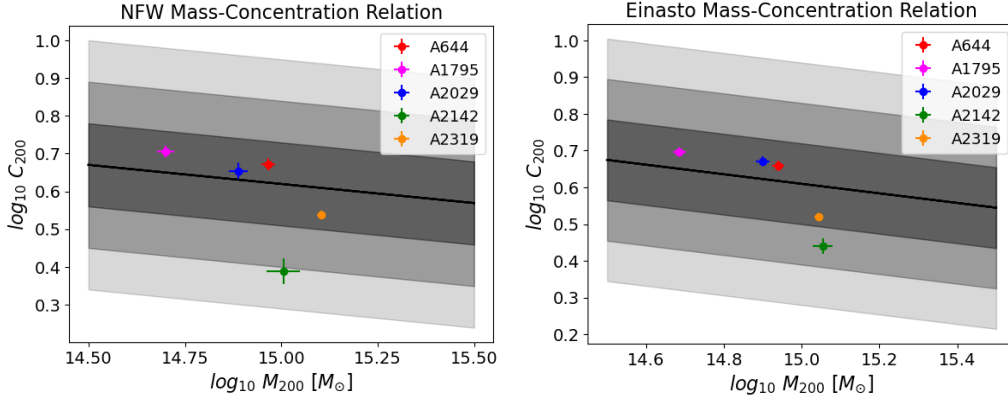
Figure 3.7: The mass-concentration relation shown in logscale. This relation is shown in black and the grey bands represent $1\sigma, 2\sigma$ and 3σ
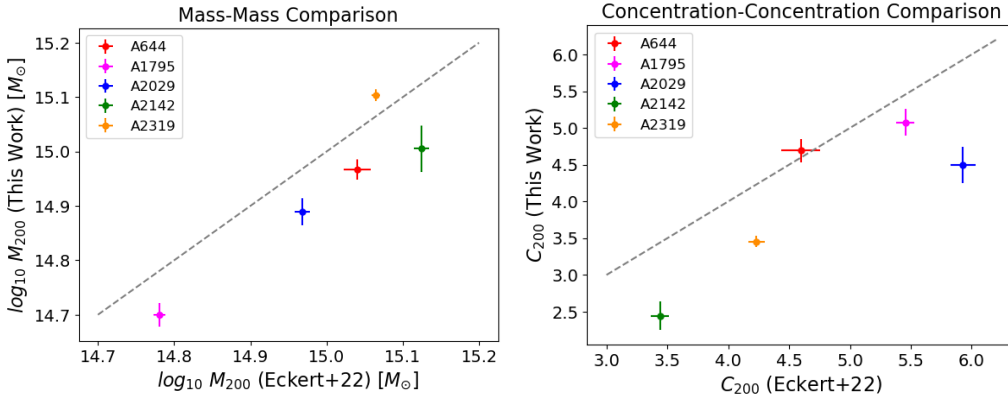
Figure 3.8: A comparison of the values obtained in this work for the NFW mass-concentration relation to those found in Eckert et al. [6]. The dotted line is the 1:1 line.

correspond to $1\sigma, 2\sigma$ and 3σ. All of the data points except for A2142 lie within 1σ, which lead to the conclusion that they are consistent with the ΛCDM paradigm. Moreover, as expected, the observed points scatter above and below the predicted relations, indicating that there is no significant systematics. The fact that the Einasto data points have slightly less scatter could point to the fact that Einasto is a better description of the clusters, but no strong conclusions can be made from this plot alone.

In Figure 3.8 the masses and concentrations determined in this study are compared to those found in Eckert et al. [6] who have only provided NFW fits. The values found in this study are generally in good agreement but systematically smaller than those in Eckert et al. [6].

The values that they quote are determined with a forward parametric model

fitted directly to the X-ray observables, whereas the values determined in this work used the non-parametric approach. The non-parametric data was used in this study because there are no predefined functional forms imposed on the data which could perhaps lead to more accurate estimates. There is also more flexibility in the non-parametric approach because there is no limit to the specific functional form and associated parameters that there is in the parametric method. Parametric models can also be more sensitive to outliers or anomalies in the data. In general, the two methods are consistent with each other, but due to their different formulation they may lead to slightly different results as is the case here.

Moster et al. [66] studied the connection between the dark matter halo of a galaxy and its stellar mass using the abundance-matching approach. In order to compare the two, the stellar-to-halo mass (SHM) ratio is determined. They adopt a parametrization derived from Yang et al. [67], which was originally derived as a mass-luminosity relation and extended to the SHM in Moster et al. [68]. The resulting relation is of the form

$$\frac{m}{M} = 2N \left[\left(\frac{M}{M_1}\right)^{-\beta} + \left(\frac{M}{M_1}\right)^{\gamma} \right]^{-1} \tag{3.35}$$

which has four free parameters. N is the value of the SHM ratio at a characteristic mass M_1. β and γ are the slopes which determine the behaviour at the low mass end for $M \ll M_1$, SHM $\propto M^{-\beta}$, and for the high mass end $M \gg M_1$, SHM $\propto M^{\gamma}$. This means that the SHM is not constant, but it increases with increasing mass, peaks and then decreases. The full expressions for M, N, β and γ can be found in Moster et al. [66].
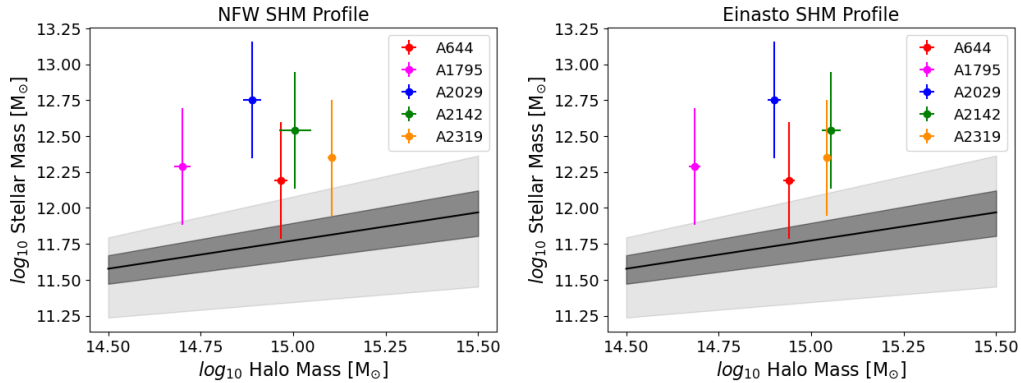
Figure 3.9: The stellar-to-halo mass relation shown in logscale in black. The grey bands represent 1σ and 3σ

Since the redshifts of the sampled clusters are < 0.1, the redshift was set to zero in the equations for simplicity. The results are shown in Figure 3.9. The shaded regions correspond to 1σ and 3σ. In Figure 3.9 all of the stellar masses lie well above the relation, indicating that the relationship between stellar mass and halo mass does not hold for these clusters. This presents another problem for the ΛCDM because this relation should be universally held.

3.8.5 Hydrostatic bias

During the MOND analysis in the next Chapter, it is proposed that the hydrostatic equilibrium assumption may not be reliable beyond 1 Mpc. There is a possibility that there is some amount of hydrostatic bias in the outskirts in the clusters, the reasons for which are discussed in Section 4.2. The fits in Chapter 4 are made using the data up to 1 Mpc. In order to compare the models, the fits in this Chapter are reproduced using the data up to 1 Mpc. The new BIC values were calculated for these fits and are included in Table 3.6, along with the averaged BIC values per model in Table 3.7. Recall that using the full data set that the pseudo-isothermal profile and the Lucky-13 fit the inner radii well, and not as well the outer radii. NFW, Einasto and Burkert do not fit the inner or outer radii well, but the intermediate regions of the profile does align with the data points. It therefore makes sense that once the outer points were removed, the pISO and Lucky13 profiles were the smallest BIC values, and that the other 3 did not improve so much as to be a better fit.

Table 3.6: The BIC values for the fits performed with data < 1 Mpc for the Newtonian models

Cluster	Bary. scaling	pISO	Burkert	Lucky13	NFW	Einasto
A644	-641.391	-699.047	-681.369	-701.736	-672.86	-675.073
A1795	-646.595	-706.03	-688.968	-689.626	-704.016	-705.83
A2029	-630.906	-692.634	-679.485	-686.162	-680.291	-685.433
A2142	-548.537	-563.903	-572.228	-564.713	-579.633	-572.697
A2319	-812.549	-898.133	-898.08	-897.779	-897.928	-900.248

Table 3.7: Average BIC values for data < 1 Mpc by model

Model	Average BIC
Baryonic scaling	-655.995
pISO	-711.949
Burkert	-704.026
Lucky13	-708.003
NFW	-706.945
Einasto	-707.856

3.9   Corner Plots
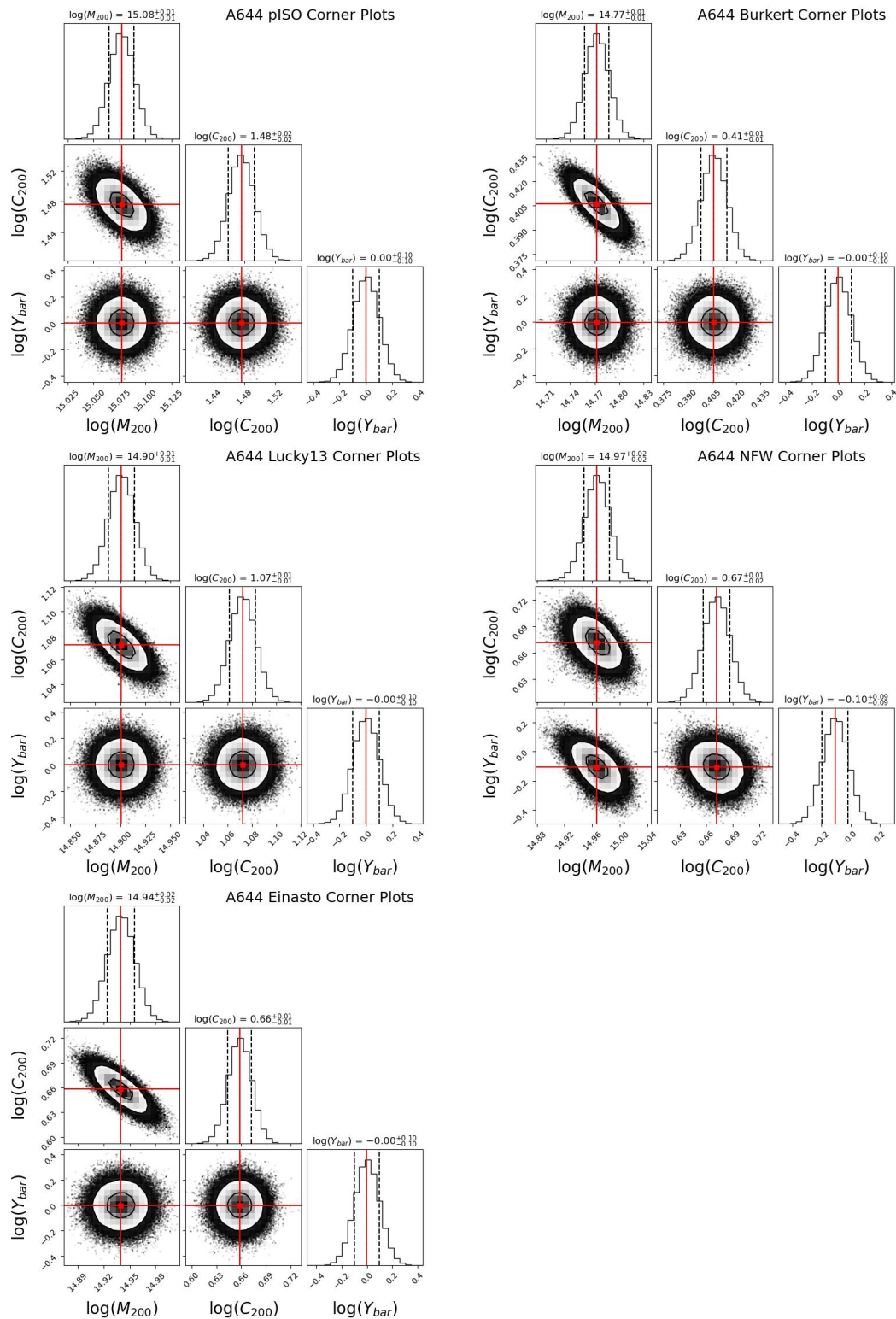
Figure 3.10: The Corner plots for A644. The best fit value is represented as a red dot at the centre of the cross on the 2D projection of the posterior probabilities. This best fit value is printed above the 1D projections of the posterior probabilities. The solid red line in the 1D projections represents the best fit value, along with the dashed lines on either side representing the 16th and 84th quantile.
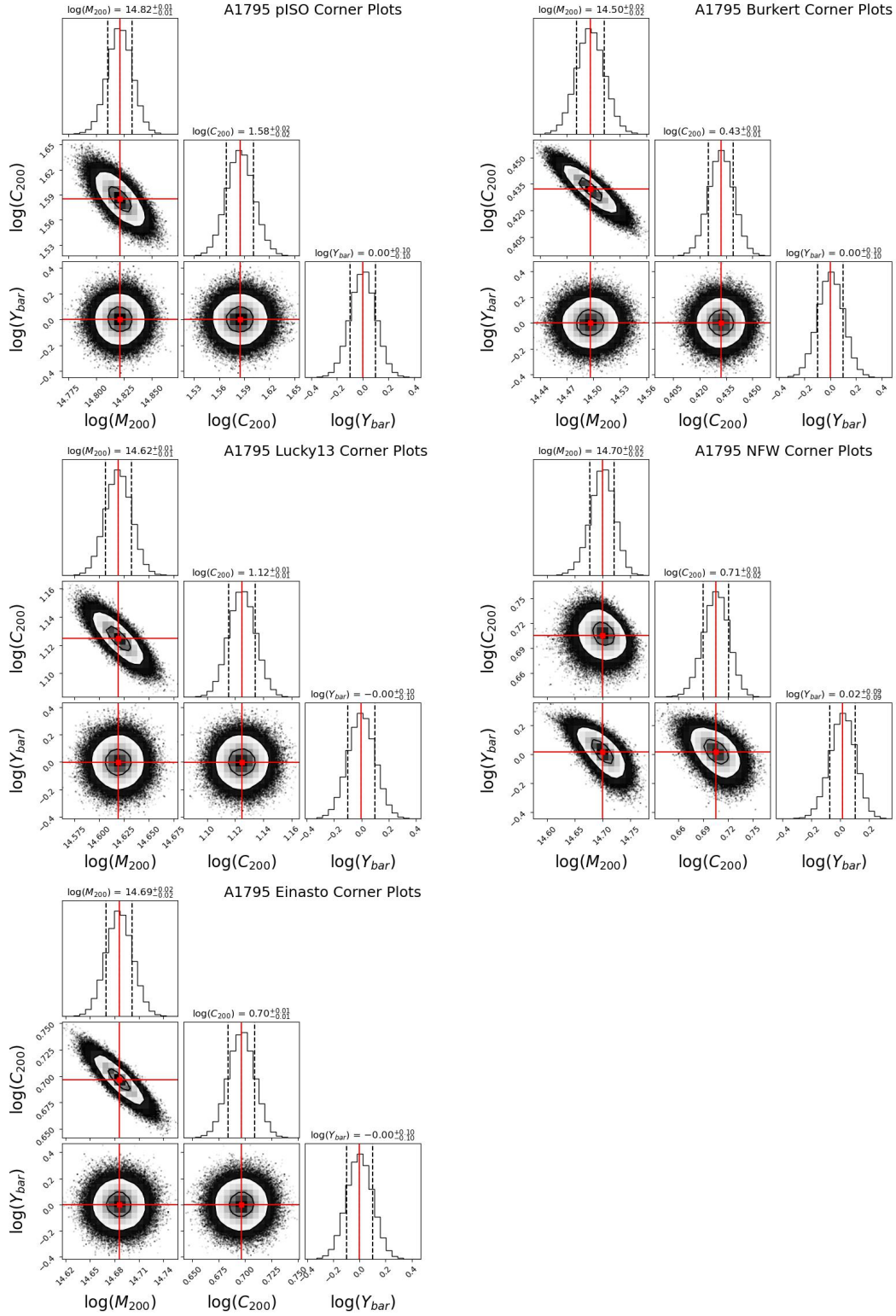
Figure 3.11: The Corner plots for A1795. The best fit value is represented as a red dot at the centre of the cross on the 2D projection of the posterior probabilities. This best fit value is printed above the 1D projections of the posterior probabilities. The solid red line in the 1D projections represents the best fit value, along with the dashed lines on either side representing the 16th and 84th quantile.
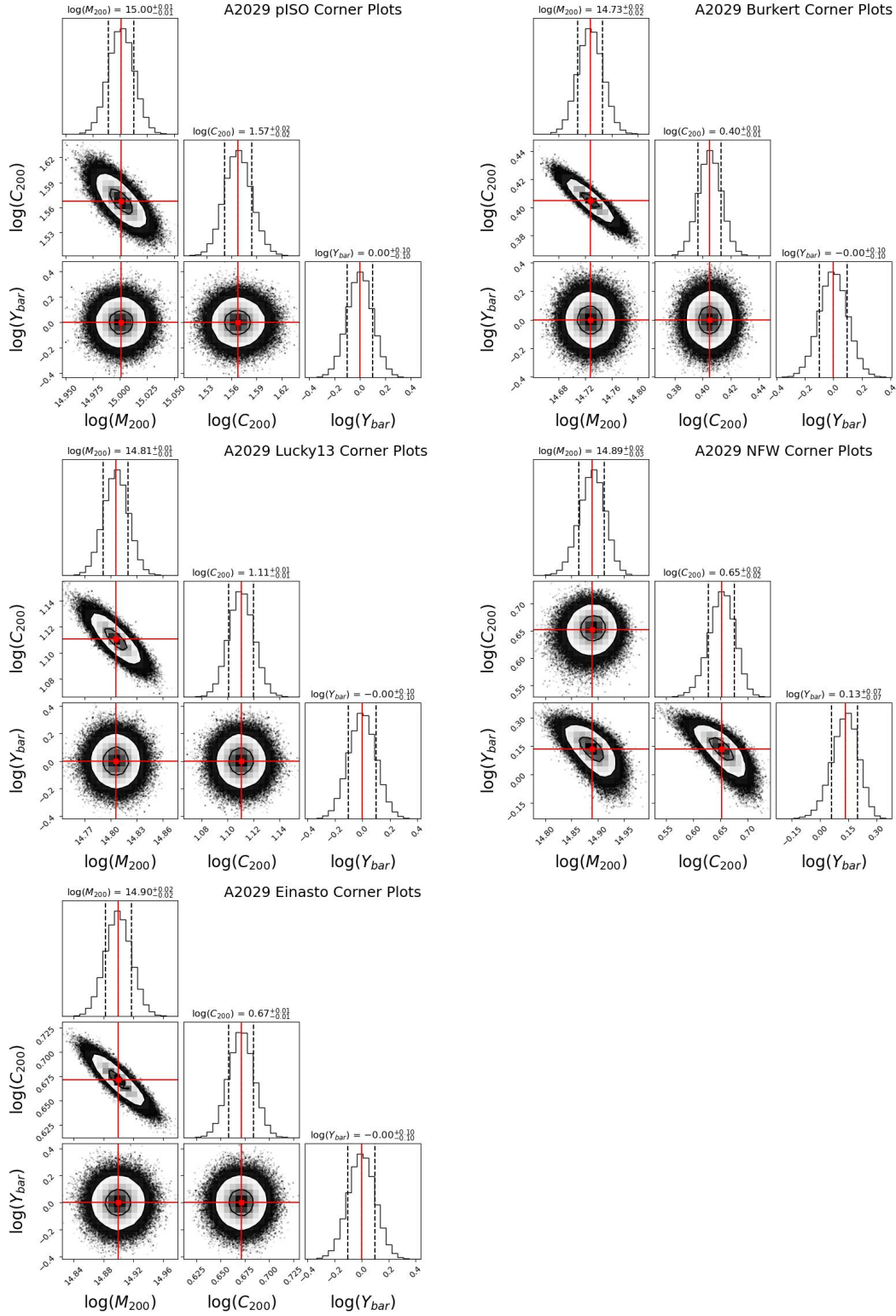
Figure 3.12: The Corner plots for A2029. The best fit value is represented as a red dot at the centre of the cross on the 2D projection of the posterior probabilities. This best fit value is printed above the 1D projections of the posterior probabilities. The solid red line in the 1D projections represents the best fit value, along with the dashed lines on either side representing the 16th and 84th quantile.
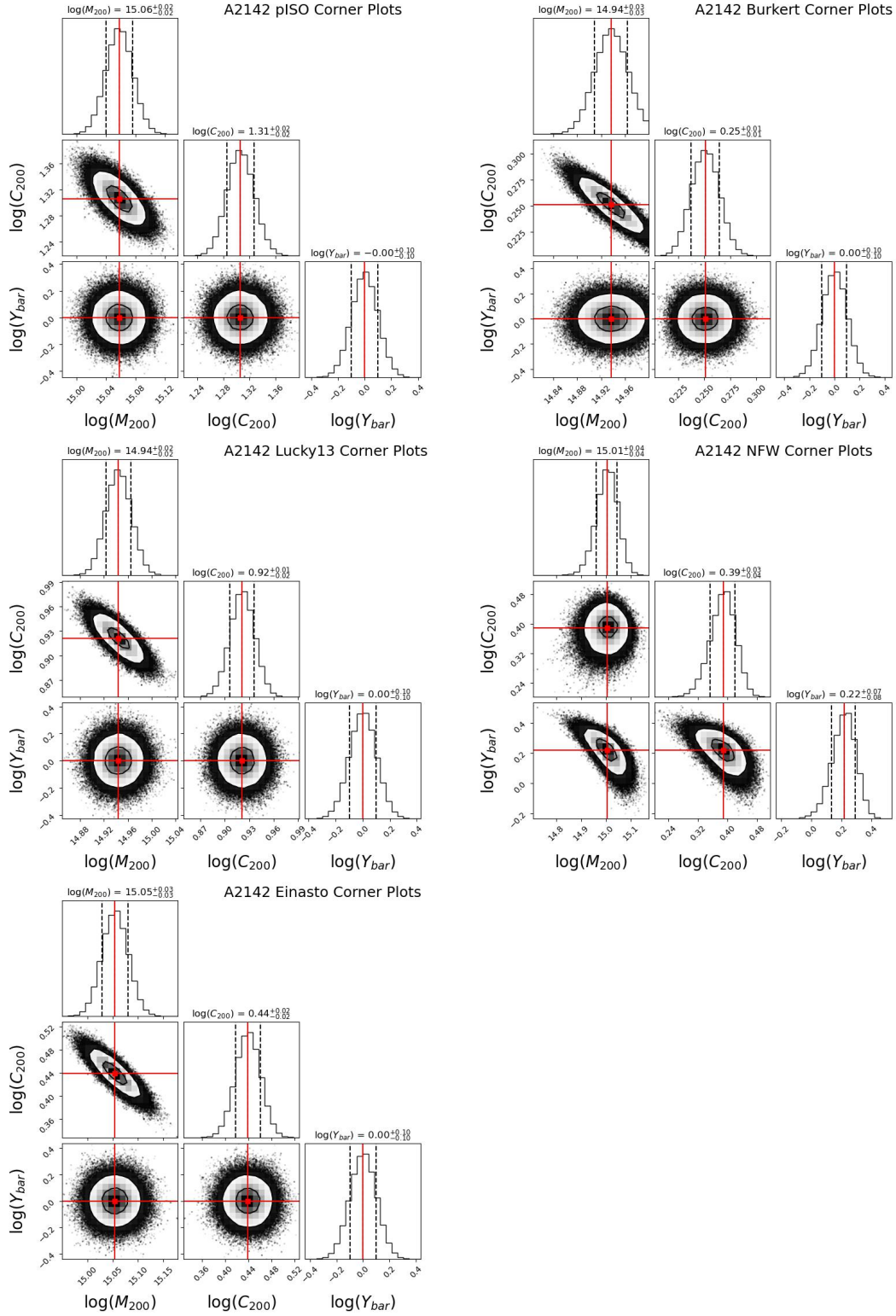
Figure 3.13: The Corner plots for A2142. The best fit value is represented as a red dot at the centre of the cross on the 2D projection of the posterior probabilities. This best fit value is printed above the 1D projections of the posterior probabilities. The solid red line in the 1D projections represents the best fit value, along with the dashed lines on either side representing the 16th and 84th quantile.
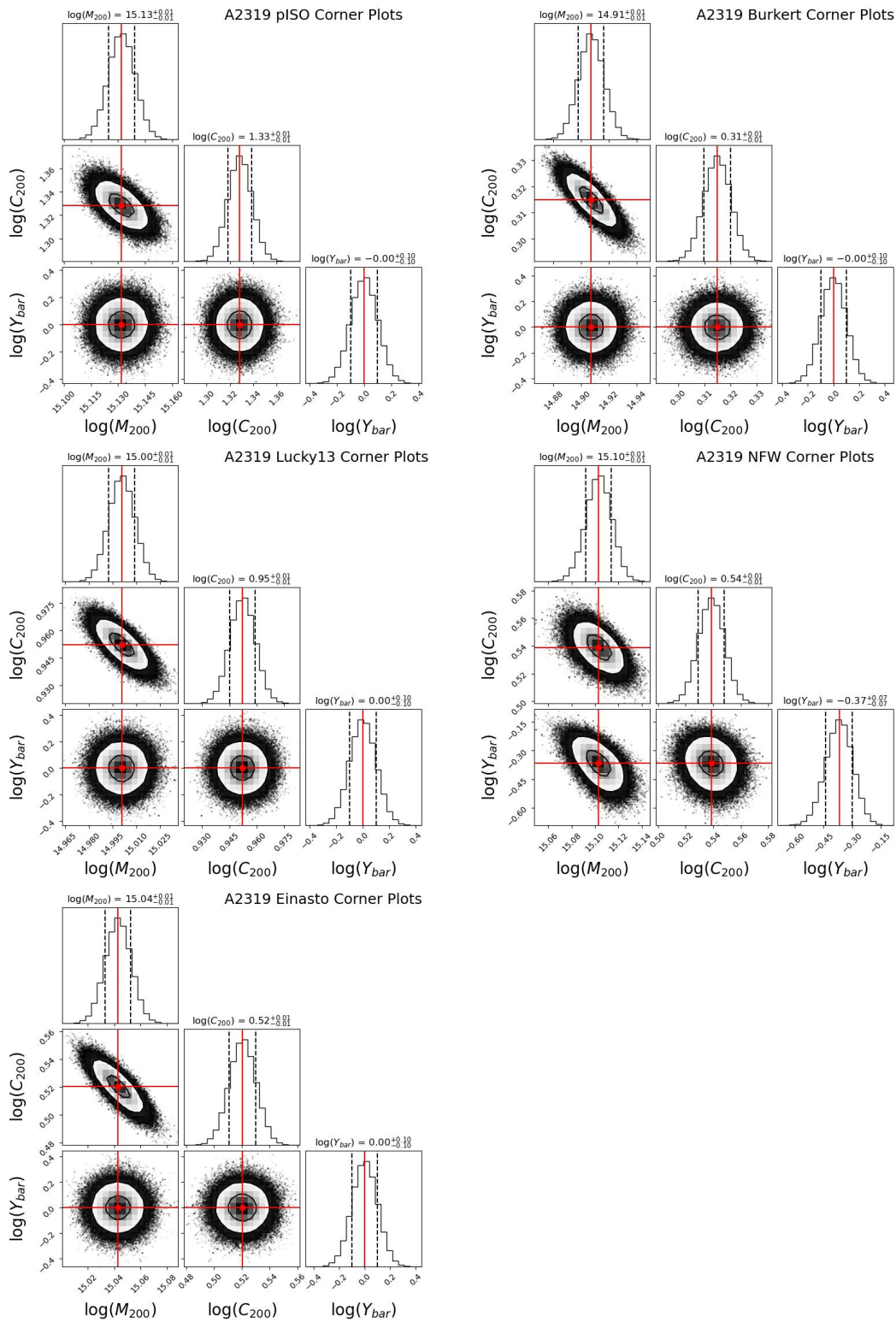
Figure 3.14: The Corner plots for A2319. The best fit value is represented as a red dot at the centre of the cross on the 2D projection of the posterior probabilities. This best fit value is printed above the 1D projections of the posterior probabilities. The solid red line in the 1D projections represents the best fit value, along with the dashed lines on either side representing the 16th and 84th quantile.

4

Milgromian Dynamics

In this Chapter I discuss galaxy clusters in the context of Milgromian dynamics to investigate whether this paradigm can explain the observed acceleration profiles of galaxy clusters. I firstly lay out models with constant M/L in Section 4.1, which imply the need for additional missing mass in galaxy clusters with a different distribution than the observed baryonic mass. Next I constrain the distribution of such a missing mass component using a direct subtraction approach in Section 4.2, as well as an MCMC fitting approach in Section 4.3.

4.1 MOND fits with constant M/L

Similarly to Section 3.2, using the Newtonian dynamics approach, the total gravitational acceleration was fit by scaling up the baryonic component using MOND dynamics. Since this involves fitting the observed gravitational acceleration, Equation 1.6 is used. As stated in Section 1.2.1, the explicit form of the interpolating function does not hugely affect the results. The $n = 1$ interpolation function was chosen, which results in

$$g = g_N \frac{1 + (1 + 4y^{-1})^{1/2}}{2} \tag{4.1}$$

where $y = g_N/a_0$. Here, the only contribution to g_N is the baryonic gravitational acceleration from galaxies and the ICM, which is scaled by the free parameter Υ_{bar}. Similarly to the previous Chapter, this was set to 0 in logspace and allowed to explore a large range of 0.25 dex or approximately 58%. Figure 4.1 shows the

results of the fit. The first column contains the acceleration profile, the second column contains the mass profile and the third column contains the rotation curve. The rows are the individual clusters. The best fit Υ_{bar} values are given in Table 4.1. These values indicate that in the context of MOND, in order to reproduce the observations, there must be approximately 3-5 times more matter than observed. In addition, the fact that the acceleration profiles are not well fit with a constant baryonic mass-to-light ratio imply that the missing mass must have a somewhat different distribution than the visible baryons.

This is quite a different situation to the results of the baryonic scaling using Newtonian dynamics. The most important difference is the magnitudes of Υ_{bar} because the MOND values are approximately a factor of 2 smaller. This is a success for MOND, as the theory attempts to minimize the amount of missing mass required. However, the values of Υ_{bar} are still too large to be ascribed to uncertainties in the ICM mass, which dominated the baryonic mass budget. There is still a need for additional mass in MOND for galaxy clusters. This result is consistent with investigations carried out in the past. [69] For example, it has been proposed that this "missing mass" may be in the form of undetected baryons, such as cold and compact gas clouds pressure-confined by the ICM (Milgrom [70]), or sterile neutrinos with a mass of about 11eV (Angus [71]). The fact that the acceleration profiles are not well fitted by simply scaling up the baryonic component means that the missing mass must have a different distribution than the visible baryons, as is investigated in the next Section.

Table 4.1: The best fit baryonic scaling Υ_{bar} values in the context of MOND in log and linear scale

Cluster	$log_{10}(\Upsilon_{bar})$	Υ_{bar}
A644	$0.684^{+0.00807}_{-0.00817}$	$4.826^{+1.0188}_{-0.981}$
A1795	$0.628^{+0.00577}_{-0.00582}$	$4.244^{+1.0134}_{-0.987}$
A2029	$0.551^{+0.00532}_{-0.00531}$	$3.558^{+1.0123}_{-0.988}$
A2142	$0.505^{+0.00852}_{-0.00867}$	$3.201^{+1.0198}_{-0.980}$
A2319	$0.529^{+0.00431}_{-0.00437}$	$3.800^{+1.00997}_{-0.990}$
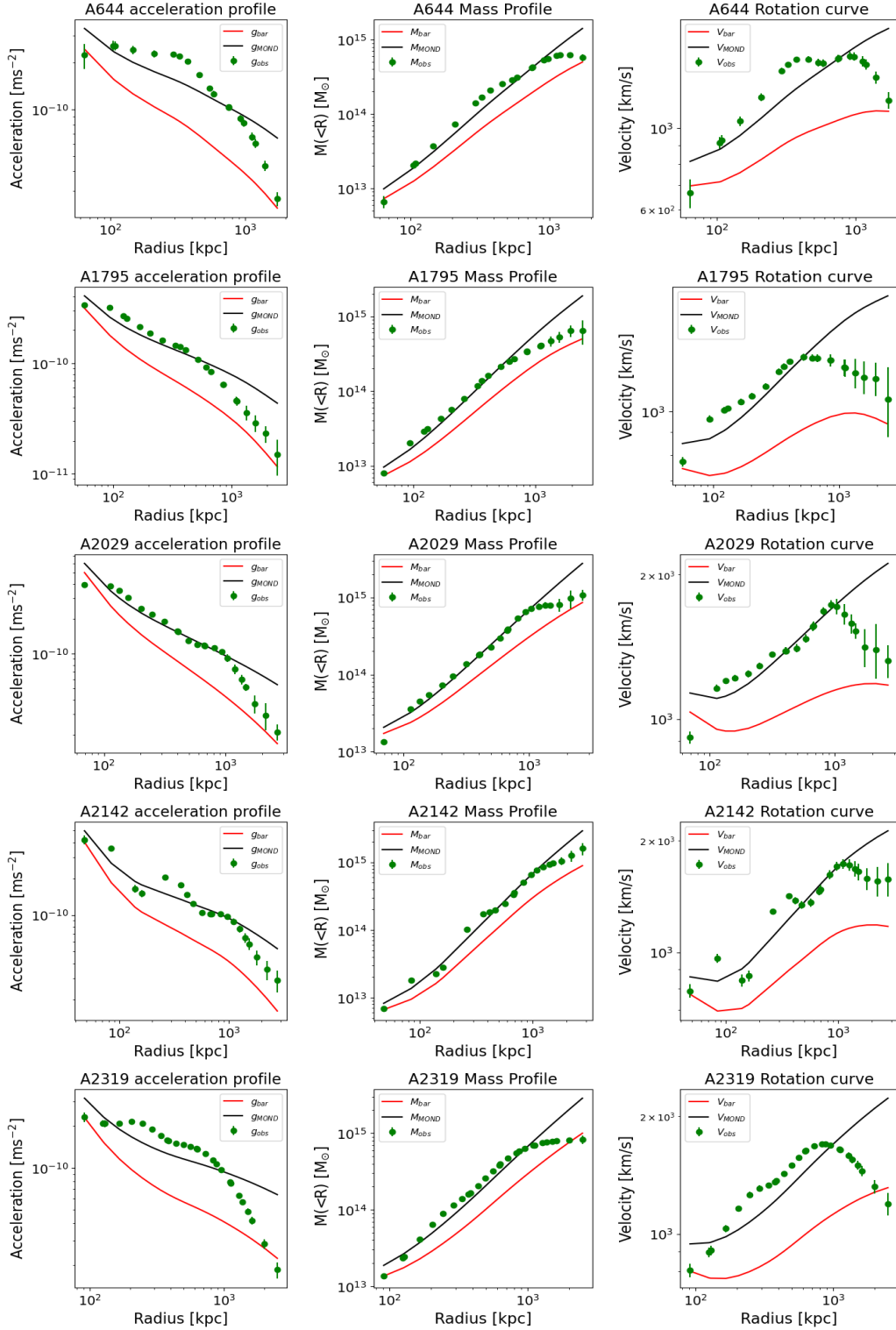
Figure 4.1: The baryonic scaling profiles in the context of MOND. The green data points are the g_{obs} data, the red line is the g_{bar} data and the black line is the scaled g_{bar} data.

4.2   MOND missing mass profiles

In order to determine the magnitude and profile of this additional missing mass, it is useful to recall the general form of the MOND equation

$$g_N = g\mu\left(\frac{g}{a_0}\right) \tag{4.2}$$

A first step in trying to determine the profile of the unknown or missing mass component can be done rearranging this equation to solve for g_{mm} (for the Newtonian grvaitational field of the missing mass) starting from

$$g_N = g_{bar} + g_{mm} = g_{obs}\mu\left(\frac{g_{obs}}{a_0}\right), \tag{4.3}$$

then we have the following expression for g_{mm}

$$g_{mm} = g_{obs}\mu\left(\frac{g_{obs}}{a_0}\right) - g_{bar}, \tag{4.4}$$

which is related to the mass distribution of this missing mass by the usual Newtonian gravitational acceleration equation

$$g_{mm} = \frac{GM_{mm}(r)}{r^2}. \tag{4.5}$$

The resulting mass profile is shown in Figure 4.2. The figures on the left are in linear scale and the figures on the right are in log scale. The different symbols indicate data from X-ray observations as blue circles and data from SZ observations as red triangles. It is immediately clear that there is an issue here because the mass profiles start to decrease after a certain radius and actually become negative in several cases. Taking the data at face value, this would point to MOND not being a viable theory.
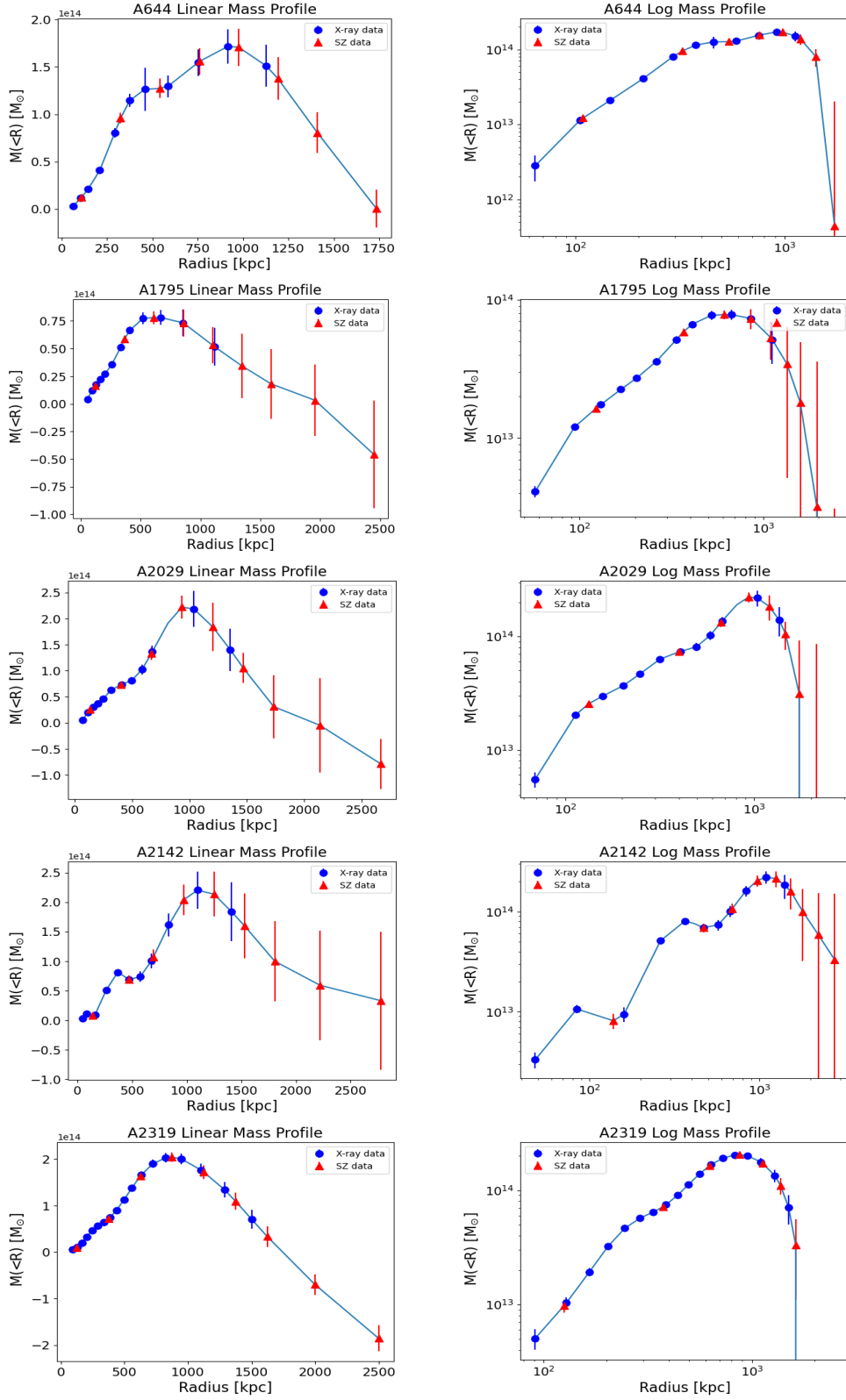
Figure 4.2: The resulting "missing mass" profiles from subtracting the baryonic gravitational acceleration g_{bar} from the observed gravitational acceleration g_{obs} in a MOND context. The plots on the left are in linear scale and the plots on the right are in log scale. The blue circles are from the X-ray observations and data from SZ observations are shown as red triangles

However, Equation 4.3 assumes that these clusters are isolated systems and that their environments had no effect on them i.e. the external field effect was not considered. Using Equation 1.32 for the external field effect

$$g_N = g_{mm} + g_{bar} = g_{obs}\mu\left(\frac{g_{obs} + g_e}{a_0}\right) + g_e\left[\mu\left(\frac{g_{obs} + g_e}{a_0}\right) - \mu\left(\frac{g_e}{a_0}\right)\right] \quad (4.6)$$

we can again solve for g_{mm}. The simple function with $n = 1$ was used and the external field was fixed to be 10%, 30%, 50% and 100% of the acceleration a_0. Using large galaxy surveys, the MOND external gravitational field due to the large-scale distribution of mass in the nearby Universe is computed to be of the order of $10\%a_0$. [72] [73] It is interesting, however, to consider higher values of g_e for two reasons: (i) galaxy clusters live in the highest density regions of the Universe, so the surrounding EFE may be higher than the average one, (ii) there are MOND theories in which the EFE is effectively given by several times the instantaneous value of g_e, so that Equation 4.6 with a higher value of g_e may provide some effective approximation for such theories. In Figure 4.3, the mass profile with no EFE is also shown in black. The left column contains the mass profiles in a linear scale and the right column displays the mass profiles in a log scale. The X-ray data in circles is still distinguished from the SZ in triangles.

In the cases of A644, A1795 and A2029 we can see that the mass profile with $g_{ext} = 0$ are negative and applying an external field of 10% (in red) is enough to make the profiles positive, albeit they are still decreasing. A2142 does not have a negative mass for $g_{ext} = 0$ and the 10% case is enough to make the profile much flatter. The 10% case for A2319 is not enough to make this profile positive but the 30% case does. The 30% case hugely improves the profiles for A2142, A2029 and A1795. A644 and A2319 however still have slightly decreasing mass profiles even for the extreme case of $g_{ext} = a_0$. There is a saturation effect above the extreme case of $g_{ext} = a_0$ where there is little to no variation in the mass profiles. Changing n of the interpolating function has little effect also, as expected. This means that for A644 and A2319 the external field effect cannot solve the issue of the decreasing mass profile, but it is successful for the others.

Eckert et al. [6] also found similar decreasing mass profiles in a MOND context but they did not consider the external field effect. They instead discussed the issue of hydrostatic bias. The observed acceleration profiles were obtained under the assumption that the cluster is in hydrostatic equilibrium with the gravitational potential, however this may not be a sound assumption in the outskirts. There could be problems with the assumptions made about the pressure support because of possible bulk motions of the gas; if the gas is moving rapidly, it can create additional pressure that was not accounted for. Closely related to this, if the motion of the

gas is turbulent, then the turbulence will cause additional pressure support. Galaxy clusters are also complex structures which are not completely smooth and uniform. They contain clumps of gas which would again alter the pressure and density profiles. There may also be mergers starting to occur in the outskirts. These possible effects, among others, may cause the HSE assumption to be invalid.

Eckert et al. [6] determined that the mass estimates from hydrostatic equilibrium at large radii (R>1 Mpc) are most likely underestimated because they could compare this data with mass estimates from weak lensing as determined by Herbonnet et al. [74]. Eckert et al. [6] estimated that the HSE assumption was not applicable beyond R_{500}. The calculated values for R_{500} can be found in Table 2 in Eckert et al. [6] and correspond approximately to 1 Mpc. Referring to Figure 4.2, the decrease in the mass profiles only occurs >1 Mpc, so if this data is indeed biased then there may be no issue with the MOND theory. It is also important to note that there has been extensive investigations into A2319 due to its odd behaviour as seen in Ghirardini et al. [75]. They posit that the cluster is undergoing a merger which is causing clumpiness in the gas and could drive the cluster out of dynamical equilbrium.

In addition to the data potentially being biased for $R > 1$Mpc, it is pertinent to recall the fact that the data is made up of X-ray and SZ data. With reference to Figure 4.2, it is clear in the linear plots that the data beyond 1 Mpc mostly consists of the SZ data. It seems that discounting the SZ data and assuming that there is a hydrostatic bias beyond 1 Mpc is one and the same. In the following Section, we will directly fit different missing mass profiles to the observed accelerations excluding data at R>1 Mpc. Then we quantify the maximum amount of hydrostatic bias that is needed in a MOND scenario with no EFE.
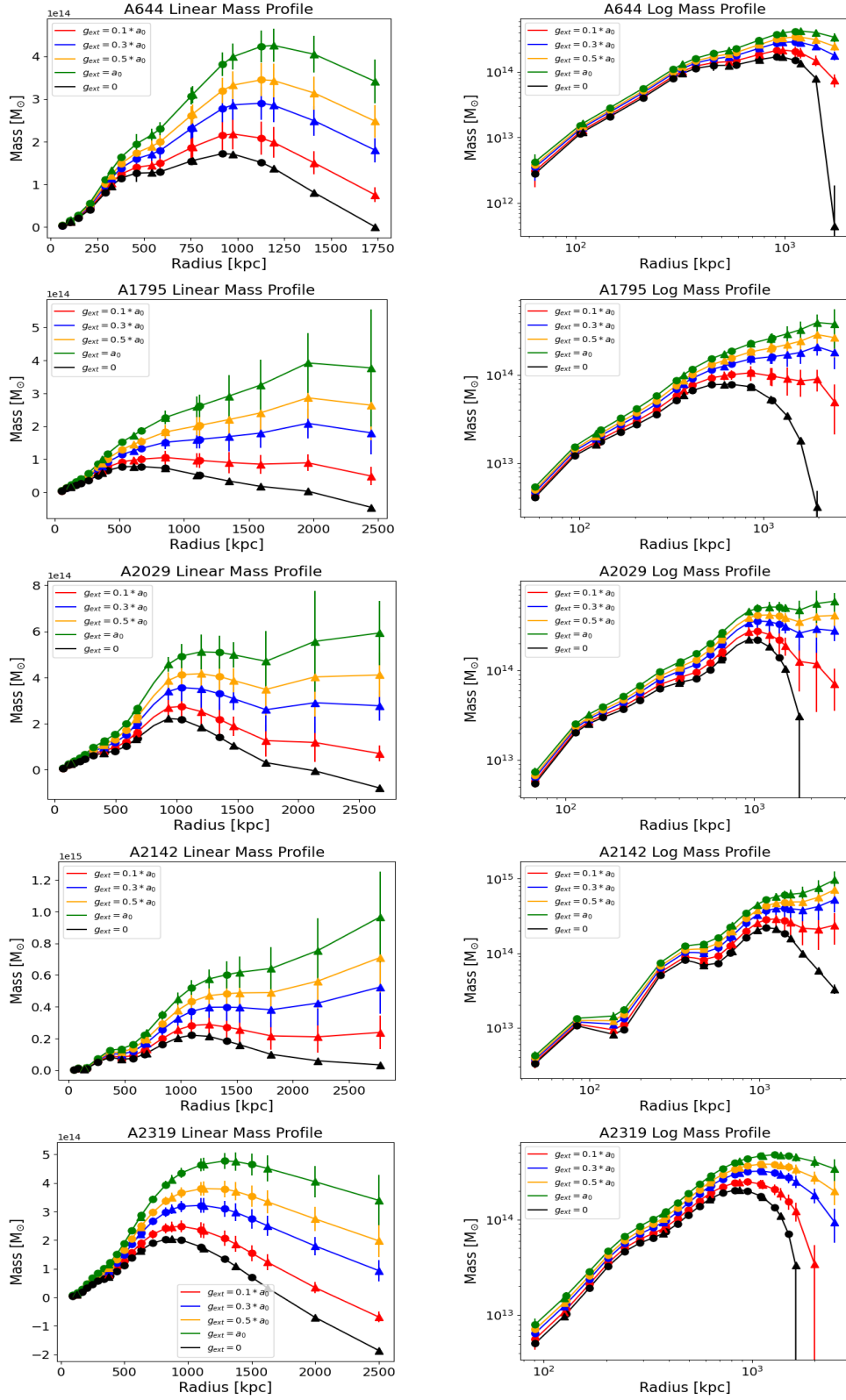
Figure 4.3: The external field effect applied to the missing mass profiles. The black line represents the original mass profile with no external field effect, the red line represents an external field of $0.1a_0$, the blue line represents $g_{ext} = 0.3a_0$, the yellow line represents $g_{ext} = 0.5a_0$ and the green line represents $g_{ext} = a_0$. The plots on the left are in linear scale and the plots on the right are in log scale. The X-ray data is still represented by circles and the SZ data by triangles.

4.3 MOND fits with a missing mass component

This Section attempts to fit the observed acceleration profiles with MOND by explicitly modelling the missing mass component with various parametric functions. As was the case with the Newtonian fits, the MCMC method of parameter estimation is used. The free parameters in these fits are the missing mass component named M_{mm}, the scale radius r_s and the baryonic scaling parameter Υ_{bar}. Υ_{bar} was again assigned a lognormal prior with a starting point of 0 in logspace and an uncertainty of 0.25 dex. M_{mm} and r_s were assigned uniform priors with broad boundaries to begin with that were later refined.

4.3.1 Cored profiles with converging mass

For any density profile of the form

$$\rho(r) = \frac{\rho_0}{(1 + \frac{r}{r_s})^n} \tag{4.7}$$

the total enclosed mass converges to a finite value for $n > 3$. For example the NFW profile is a case with $n = 3$ at large radii. The first profile that of this form that was tested is the $n = 4$ profile

$$\rho(r) = \frac{\rho_0}{(1 + \frac{r}{r_s})^4} \tag{4.8}$$

The total enclosed mass is given by

$$M(< r) = \int_0^r 4\pi r'^2 \frac{\rho_0}{(1 + \frac{r'}{r_s})^4} dr' \tag{4.9}$$

$$= \frac{4\pi \rho_0 r_s^3}{3} \frac{\left(\frac{r}{r_s}\right)^3}{\left(1 + \frac{r}{r_s}\right)^3} \tag{4.10}$$

In the limit of $r \to \infty$ the mass converges to a finite value given by

$$M_{mm} = \frac{4\pi \rho_0 r_s^3}{3} \tag{4.11}$$

and expressing this in terms of the adimensional variable $x = r/r_s$ gives the final

expression

$$M(r) = M_{mm}\frac{x^3}{(1+x)^3}. \tag{4.12}$$

The same methodology was performed for the $n = 5$ profile resulting in

$$M(r) = M_{mm}\frac{(x^4 + 4x^3)}{(1+x)^4} \tag{4.13}$$

where M_{mm} is defined as $\pi\rho_0 r_s^3/3$ for the $n = 5$ case. As well as the $n = 6$ case

$$M(r) = M_{mm}\frac{(x^5 + 5x^4 + 10x^3)}{(1+x)^5} \tag{4.14}$$

where M_{mm} is defined as $4\pi\rho_0 r_s^3/30$ for the $n = 6$ case.

4.3.2   Truncated sphere with $\rho(r) \propto r^{-1}$

We now consider a density profile that is abruptly truncated at some radius r_s and has a cuspy profile for $r < r_s$ given by

$$\rho(r) = \begin{cases} \frac{\rho_0}{r} & r < r_s \\ 0 & r > r_s \end{cases} \tag{4.15}$$

so that the total enclosed mass is

$$M(r = r_s) = \int_0^{r_s} 4\pi\frac{\rho_0}{r'}r'^2 dr' \tag{4.16}$$

$$= \frac{4\pi\rho_0 r_s^2}{2} \quad = M_{mm} \tag{4.17}$$

The mass profile at some radius $r < r_s$ is therefore

$$M(r) = \int_0^r 4\pi r'^2\frac{\rho_0}{r'} dr' \tag{4.18}$$

$$= \frac{4\pi\rho_0 r^2}{2} \tag{4.19}$$

Multiplying by r_s^3/r_s^3 and using the expression for M_{mm} gives

$$M(r) = M_{mm}x^2 \tag{4.20}$$

84

4.3.3 Truncated sphere with constant density

We now consider the case of a profile in which the density is a constant with radius up to the truncation radius and after which it goes to zero. This density profile is described by the piecewise function

$$\rho(r) = \begin{cases} \rho_0 & r < r_s \\ 0 & r > r_s \end{cases} \tag{4.21}$$

Total enclosed mass is given by

$$M(r < r_s) = \int_0^{r_s} 4\pi \rho_0 r'^2 dr' \tag{4.22}$$

$$= \frac{4\pi \rho_0 r_s^3}{3} \quad = M_{mm} \tag{4.23}$$

The mass profile is therefore

$$M(r) = \int_0^{r'} 4\pi r'^2 \rho_0 r'^2 dr' \tag{4.24}$$

$$= \frac{4\pi \rho_0 r^3}{3} \tag{4.25}$$

Multiplying by r_s^3/r_s^3 and using the expression for M_{mm} gives the expression

$$M(r) = M_{mm} x^3 \tag{4.26}$$

4.4 Results

The corner plots of the fits can be found at the end of the chapter. The results are presented in the same way as before; every cluster has a dedicated page where the columns are the acceleration profiles, the mass profiles and the circular velocity curves. The rows contain the various models where $1/R^4$ stands for the $\rho(r) = \rho_0/(1 + \frac{r}{r_s})^4$ profile, likewise for $1/R^5$ and $1/R^6$. The fits were made only using data up to 1 Mpc as discussed in Section 4.2, but the g_{obs} data beyond 1 Mpc is still included as hollow points for reference. The grey line labelled as MONDe stands for extrapolated because the g_{mond} formula, along with the best fit parameters, were applied to the data beyond 1 Mpc in order to attempt to determine the extent of the hydrostatic bias. A full discussion can be found in Section 4.4.2.

It is not immediately clear which of the profiles provide the best fit. The $1/r$ and constant density profiles however have very strict boundaries which makes the blue line, representing the missing mass component, have extreme and pointed behaviour. This is in contrast to the R^n profiles which are much smoother and have more gradual profiles. It is more likely in nature to find these smoother profiles rather than profiles with strict boundary. A quantitative comparison is found in the next section.

Table 4.2: The best fit model parameters from the MCMC parameter estimation procedure. These values are quoted in base 10 logarithm with M_{mm} in Solar mass units and r_s in kpc

		$1/r$	Const.	$1/R^4$	$1/R^5$	$1/R^6$
A644	$log(\Upsilon_{bar})$	$0.34\ ^{+0.06}_{-0.07}$	0.53 ± 0.03	$-0.36\ ^{+0.17}_{-0.18}$	$-0.33\ ^{+0.17}_{-0.18}$	$-0.29\ ^{+0.17}_{-0.19}$
	$log(M_{mm})$	14.00 ± 0.04	13.80 ± 0.04	13.62 ± 0.03	13.47 ± 0.03	13.40 ± 0.03
	$log(r_s)$	$2.56\ ^{+0.02}_{-0.01}$	$2.44\ ^{+0.03}_{-0.02}$	2.53 ± 0.02	2.52 ± 0.02	2.65 ± 0.02
A1795	$log(\Upsilon_{bar})$	$0.49\ ^{+0.02}_{-0.03}$	0.53 ± 0.01	$0.11\ ^{+0.08}_{-0.09}$	$0.21\ ^{+0.06}_{-0.07}$	0.25 ± 0.05
	$log(M_{mm})$	$13.25\ ^{+0.10}_{-0.06}$	$13.10\ ^{+0.04}_{-0.05}$	13.07 ± 0.05	12.88 ± 0.05	12.80 ± 0.05
	$log(r_s)$	$2.27\ ^{+0.06}_{-0.02}$	2.16 ± 0.01	2.09 ± 0.02	2.27 ± 0.02	2.40 ± 0.02
A2029	$log(\Upsilon_{bar})$	0.47 ± 0.02	0.48 ± 0.01	$0.24\ ^{+0.05}_{-0.06}$	$0.29\ ^{+0.04}_{-0.05}$	0.32 ± 0.04
	$log(M_{mm})$	13.25 ± 0.08	$13.19\ ^{+0.07}_{-0.08}$	$13.17\ ^{+0.05}_{-0.06}$	12.97 ± 0.06	12.88 ± 0.06
	$log(r_s)$	$2.29\ ^{+0.05}_{-0.03}$	$2.22\ ^{+0.02}_{-0.04}$	2.15 ± 0.03	$2.33\ ^{+0.02}_{-0.03}$	$2.45\ ^{+0.02}_{-0.03}$
A2142	$log(\Upsilon_{bar})$	$0.36\ ^{+0.03}_{-0.04}$	$0.39\ ^{+0.02}_{-0.03}$	0.35 ± 0.05	0.36 ± 0.05	$0.36\ ^{+0.04}_{-0.05}$
	$log(M_{mm})$	$13.62\ ^{+0.06}_{-0.07}$	$13.55\ ^{+0.06}_{-0.07}$	$13.12\ ^{+0.12}_{-0.14}$	$12.95\ ^{+0.11}_{-0.14}$	12.89 ± 0.10
	$log(r_s)$	2.54 ± 0.02	2.46 ± 0.02	2.35 ± 0.06	2.53 ± 0.05	2.65 ± 0.05
A2319	$log(\Upsilon_{bar})$	0.36 ± 0.03	0.51 ± 0.01	$0\ ^{+0.08}_{-0.10}$	$0.08\ ^{+0.07}_{-0.08}$	$0.12\ ^{+0.06}_{-0.07}$
	$log(M_{mm})$	14.04 ± 0.04	13.72 ± 0.05	13.75 ± 0.03	13.56 ± 0.03	13.47 ± 0.03
	$log(r_s)$	2.76 ± 0.01	$2.65\ ^{+0.02}_{-0.03}$	2.54 ± 0.02	2.71 ± 0.02	2.83 ± 0.01
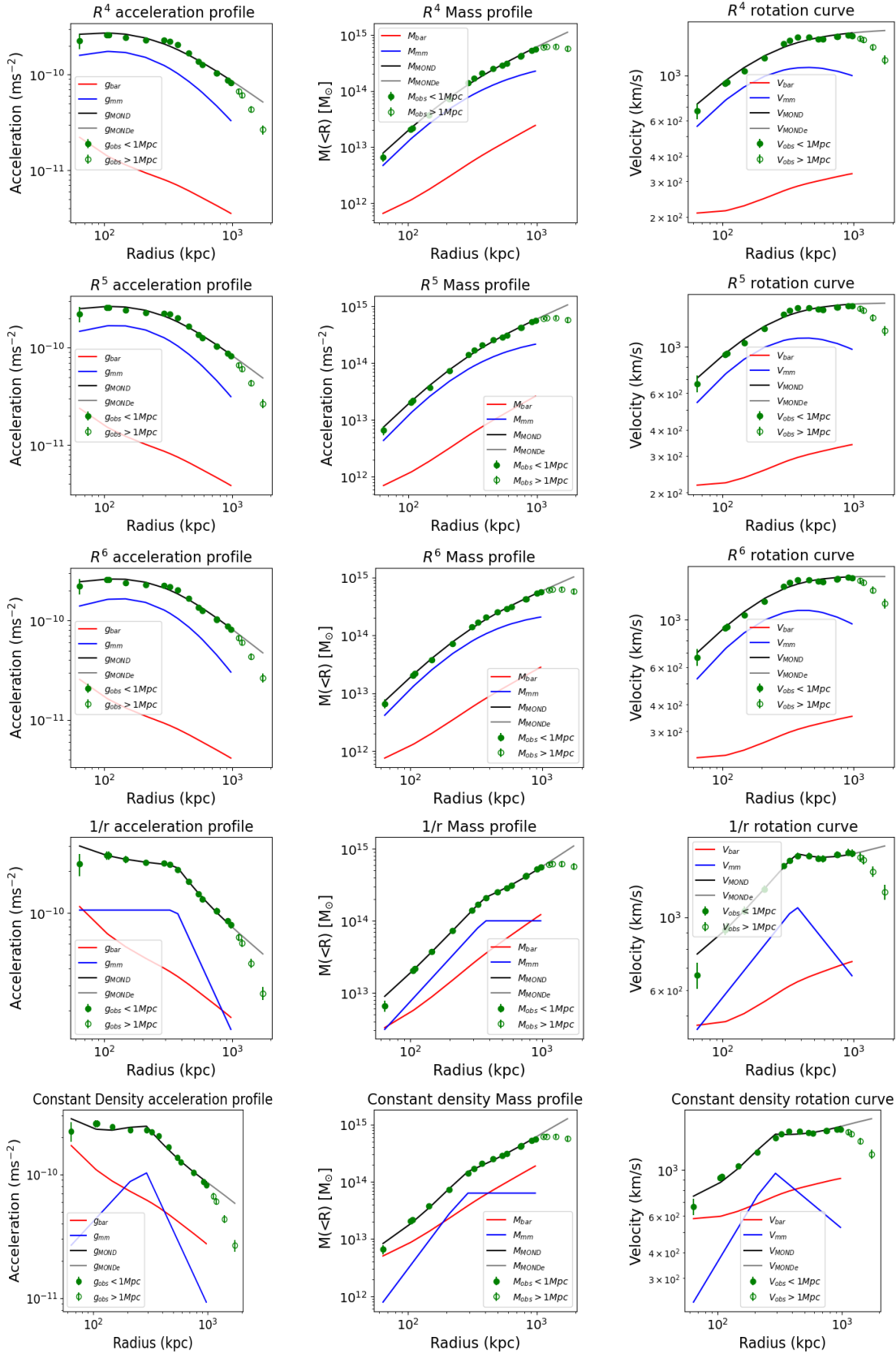
Figure 4.4: The A644 profiles. The solid green data points are the g_{obs} data up to 1 Mpc and the green circles are the g_{obs} data beyond 1 Mpc. The red line is the g_{bar} data, the blue line is the model's missing mass gravitational acceleration profile, the black line is the MOND fit with data up to 1 Mpc and the grey line is the MOND fit extrapolated to the data beyond 1 Mpc.
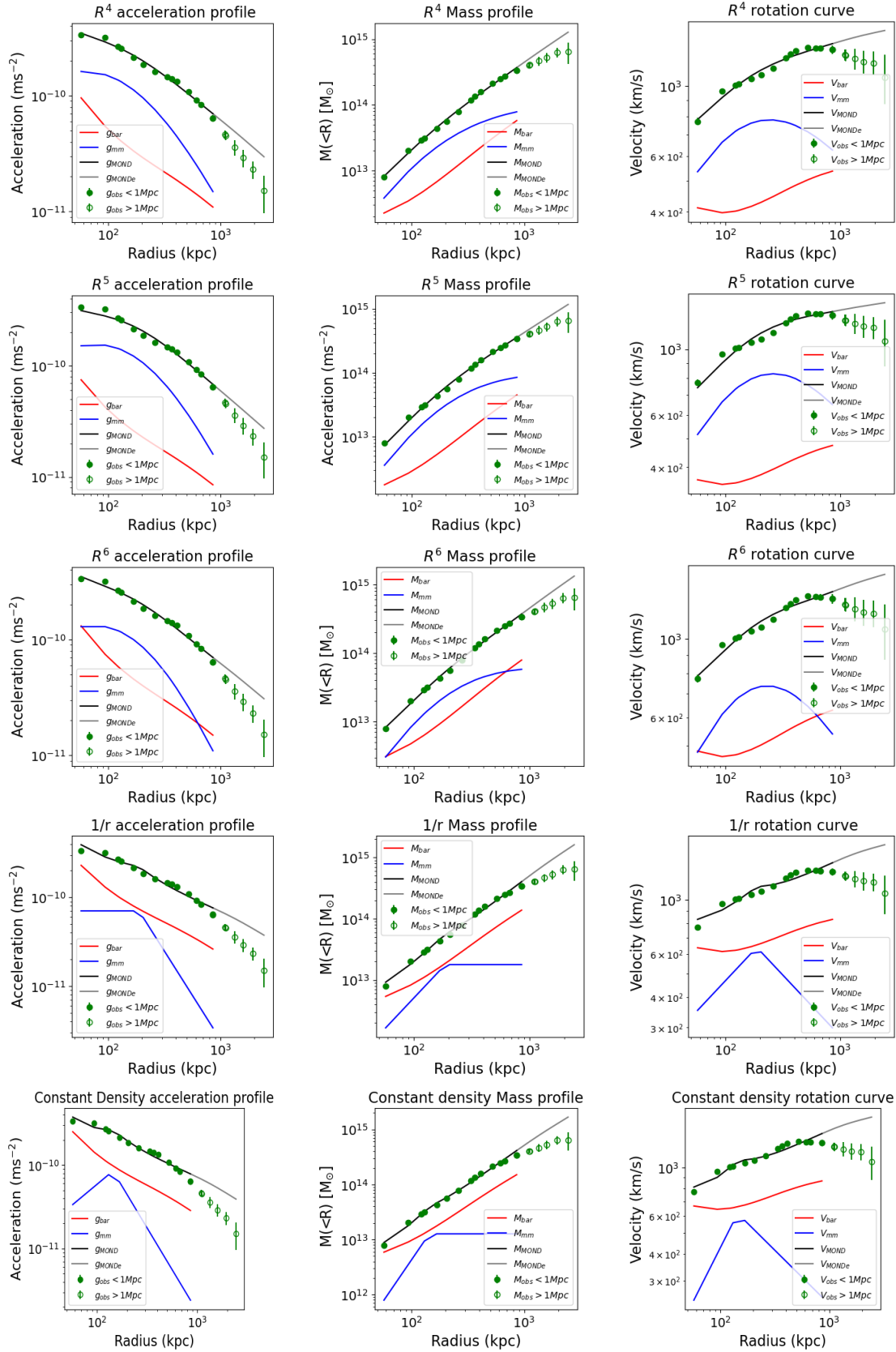
Figure 4.5: The A1795 profiles. The solid green data points are the g_{obs} data up to 1 Mpc and the green circles are the g_{obs} data beyond 1 Mpc. The red line is the g_{bar} data, the blue line is the model's missing mass gravitational acceleration profile, the black line is the MOND fit with data up to 1 Mpc and the grey line is the MOND fit extrapolated to the data beyond 1 Mpc.
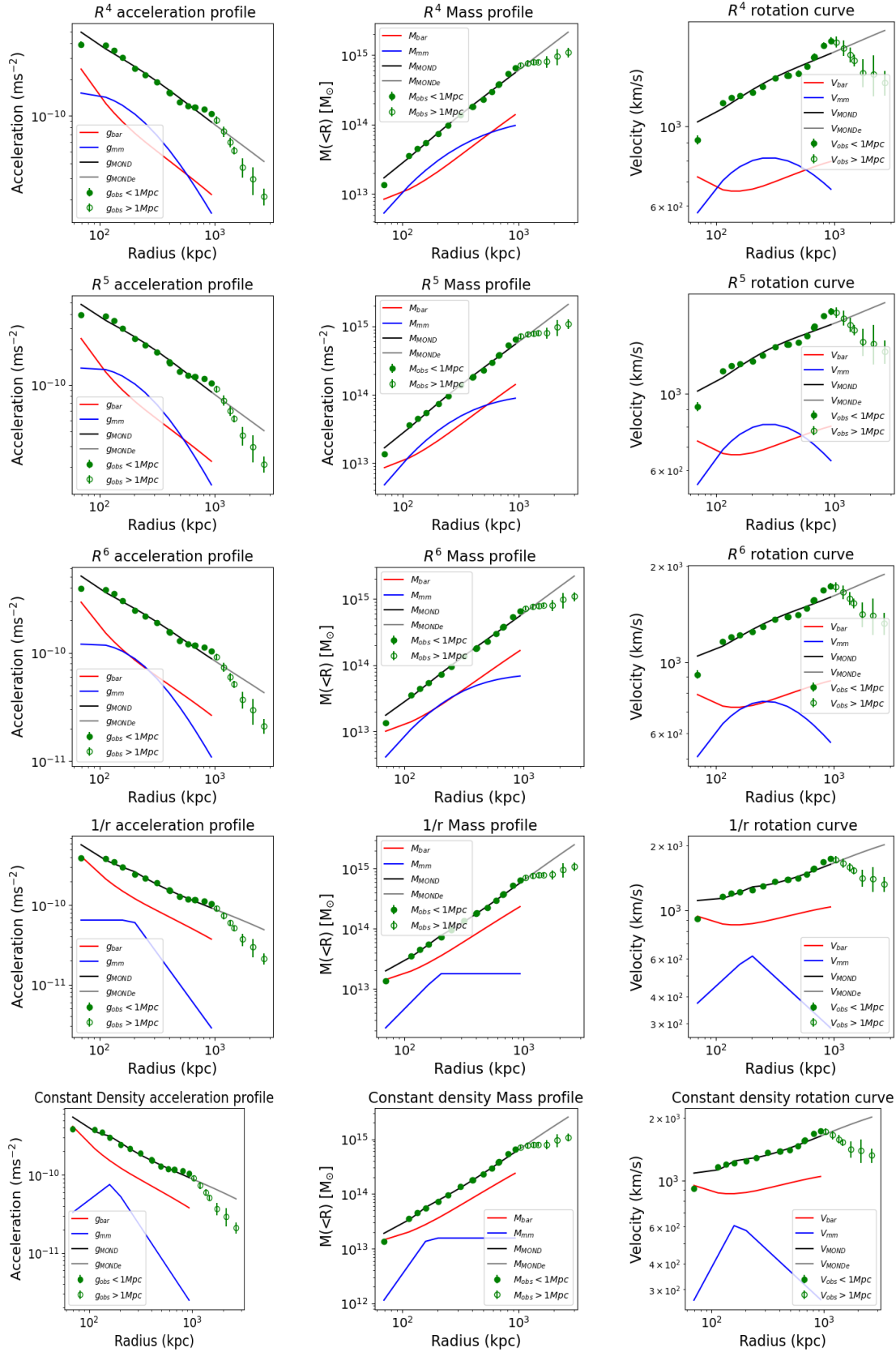
Figure 4.6: The A2029 profiles. The solid green data points are the g_{obs} data up to 1 Mpc and the green circles are the g_{obs} data beyond 1 Mpc. The red line is the g_{bar} data, the blue line is the model's missing mass gravitational acceleration profile, the black line is the MOND fit with data up to 1 Mpc and the grey line is the MOND fit extrapolated to the data beyond 1 Mpc.
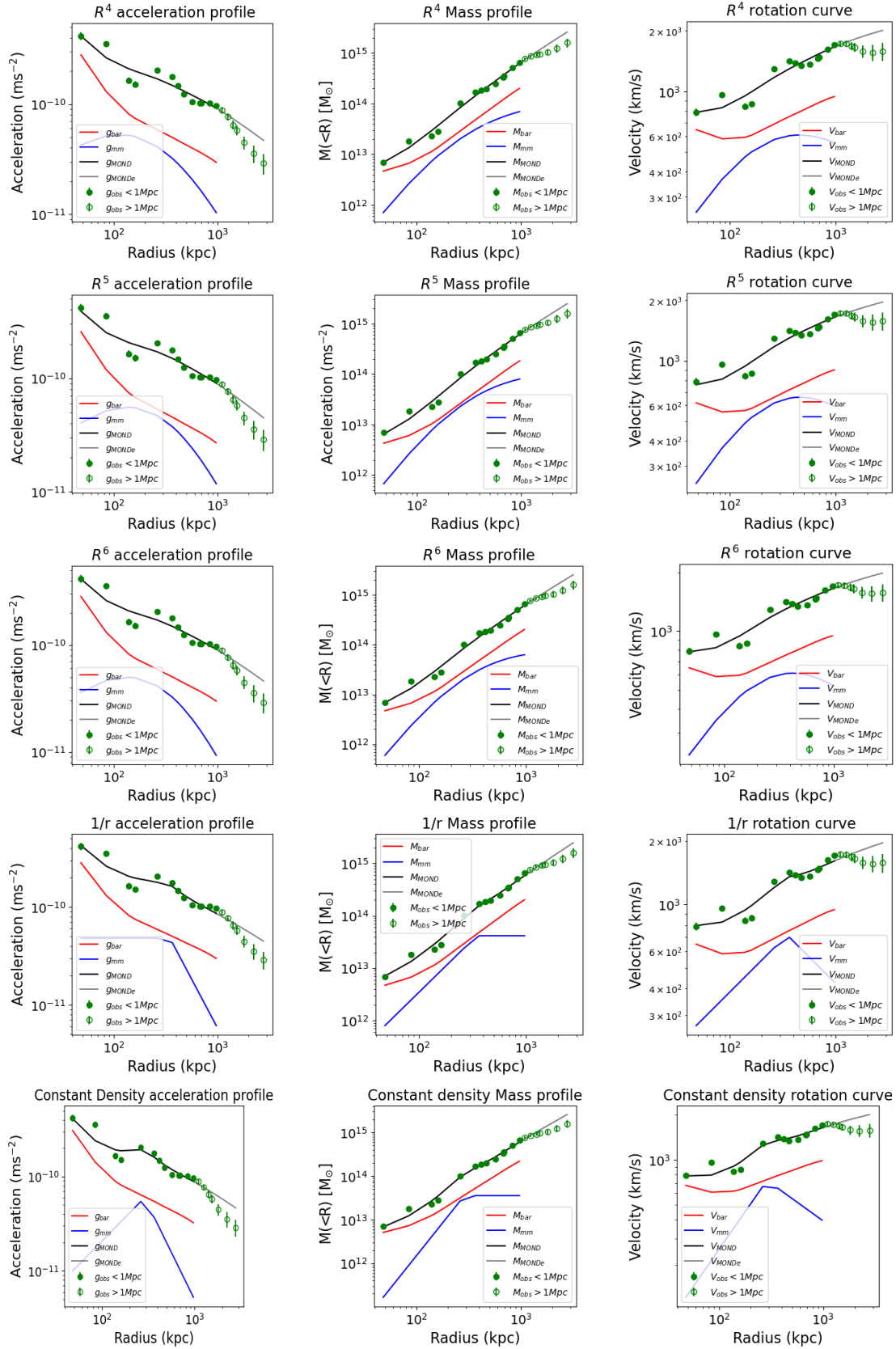
Figure 4.7: The A2142 profiles. The solid green data points are the g_{obs} data up to 1 Mpc and the green circles are the g_{obs} data beyond 1 Mpc. The red line is the g_{bar} data, the blue line is the model's missing mass gravitational acceleration profile, the black line is the MOND fit with data up to 1 Mpc and the grey line is the MOND fit extrapolated to the data beyond 1 Mpc.
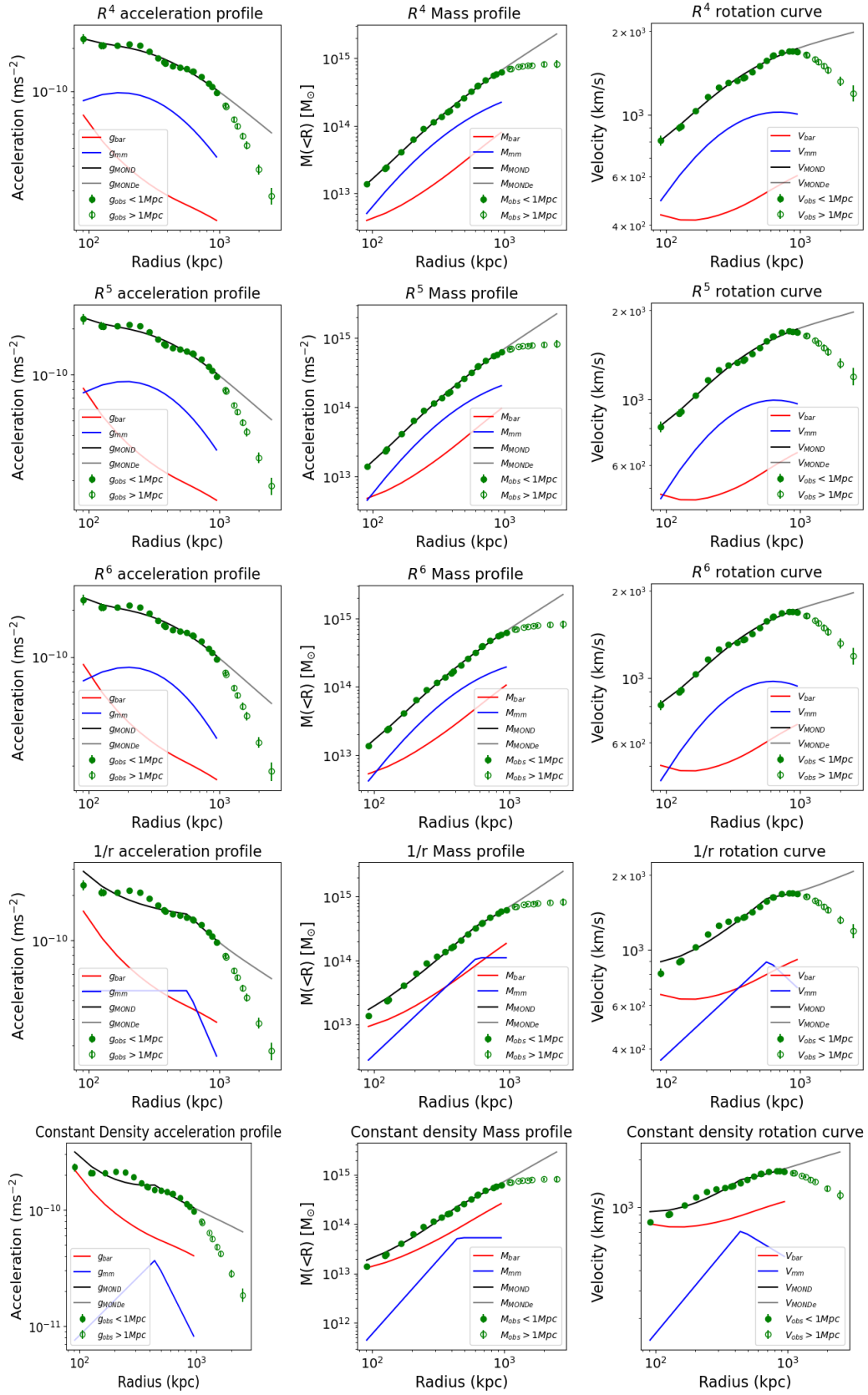
Figure 4.8: The A2319 profiles. The solid green data points are the g_{obs} data up to 1 Mpc and the green circles are the g_{obs} data beyond 1 Mpc. The red line is the g_{bar} data, the blue line is the model's missing mass gravitational acceleration profile, the black line is the MOND fit with data up to 1 Mpc and the grey line is the MOND fit extrapolated to the data beyond 1 Mpc.

4.4.1 BIC values

The BIC values were calculated for these models in order to quantitatively compare them. The results can be found in Table 4.3. The average BIC for the models is shown in Table 4.4. Recall that the smaller the BIC value the better the model fits the data. Referring to Table 3.5 which quantifies the strength of how much better a model is with respect to another, we can comment that there is virtually no difference between the $1/r$ and the constant density models. If these models are compared to the R^n models however, there is a strong to very strong preference for those R^n models. The $1/R^5$ and $1/R^6$ models were included to determine whether or not a steeper profile than the $1/R^4$ profile is preferred. The $1/R^4$ profile has a slightly smaller BIC than the $1/R^5$ profile value but according to Table 3.5 this difference is negligible in terms of preference. However the even steeper $1/R^6$ profile, is less preferred than the $1/R^4$ and $1/R^5$ profiles, but is strongly preferred than the other two. It is no surprise that the data favors the R^n models because they are the smooth profiles with no abrupt discontinuities in contrast to the other models.

Table 4.3: The BIC values for the models in a MOND context

Cluster	Baryonic scaling	$1/r$	Const. ρ	$1/R^4$	$1/R^5$	$1/R^6$
A644	-655.711	-688.222	-689.114	-693.759	-699.84	-703.654
A1795	-668.034	-688.871	-693.525	-708.634	-697.57	-705.963
A2029	-649.022	-661.679	-665.720	-676.965	-678.792	-673.347
A2142	-571.229	-583.01	-581.085	-581.87	-579.929	-581.548
A2319	-838.057	-876.082	-865.134	-910.981	-909.501	-867.21

Table 4.4: Average BIC values by model

Model	Average BIC
Baryonic Scaling	-676.410
$1/r$	-699.573
Constant density	-698.916
$1/R^4$	-714.442
$1/R^5$	-713.126
$1/R^6$	-706.344

With reference to the corner plots at the end of the Chapter, the $1/R^4$ plots are the most well behaved set. The $1/r$ and constant density plots occasionally had abnormalities such as a slight bimodal distribution. The main peak was chosen by

the code as the best fit parameters in each case because the second peak was never very strong. The number of steps, walkers and burn-ins were all increased to try to minimize these effects but they persisted. This indicates that it is not a problem of insufficient time to converge to the best fit parameter, but that these models are a poor choice for the data.

The last piece of evidence to suggest that the R^n models are more favorable, in particular the $1/R^4$ model, is the magnitude of the Υ_{bar} values as quoted in Table 4.2. The magnitude of these values have been reduced significantly in comparison to the values in Table 4.1 in which the baryons alone were scaled up. These are quite reasonable values for the Υ_{bar}, the largest being for A2142 and is 2.2 in a linear scale. This is a success for MOND as the need for additional baryonic matter has been greatly decreased. This has been seen to be true for galaxies but has had varying degrees of success for galaxy clusters. The magnitudes of Υ_{bar} for the $1/r$ and constant density models have been slightly reduced in some cases but still remains large, adding to the support for discounting those models.

4.4.2 Estimation of hydrostatic bias

As described in Section 4.2, the fits were performed using data up to 1 Mpc. After the best fit parameters were determined with this data set, the model was extrapolated out to larger radii using those parameters. This model is shown as the grey profile and labelled MONDe. In order to attempt to determine the level of hydrostatic bias, we compute

$$\frac{g_{mond} - g_{obs}}{g_{obs}} \text{x}100 \tag{4.27}$$

This is a measure of the absolute percentage difference between the data and the model. This was applied to the whole dataset, not just that above 1 Mpc. This percentage difference is plotted against the radius in Figure 4.9. The rows show the results from the individual clusters and columns show the various models. The black points labelled g_{MOND} are the points that were used in the fit up to 1 Mpc. The grey points labelled as g_{MONDe} are those extrapolated beyond 1 Mpc. Since the BIC values are so similar for the $1/R^4$ and $1/R^5$ profiles, only the $1/R^4$ profiles were included here.

In general, the black points stay within approximately 20%. Cluster A2142, however, has a lot of variation in the points in the inner radii as seen in Figure 4.7 and so the percentage difference from model to data is larger here. Occasionally, the first, or first two residuals from the extrapolated model are negative. This is expected because the R_{500} value that was calculated in Eckert et al. [6], above which there is hydrostatic bias, is not exactly 1 Mpc but very slightly above for

some clusters. Above the R_{500} value however all of the residuals are positive as expected. The cluster with the largest deviation of the data from the extrapolated model is A2319 in the fifth row where one point reaches as high as 250%. This means that, in order to compensate for the decreasing mass profiles, there needs to be a factor of 2.5 times more gravitational acceleration (hence pressure support) in the furthest outskirts, in this extreme case. We recall, however, that A2319 is likely affected by mergers at large radii, so it is not surprising to find such an anomalous value. This may instead point to the remarkable fact that MOND may be able to identify such merging clusters.

Focusing on the $1/R^4$ profile which represents the most favorable model, there needs to be a factor of approximately 0.4 to 1.2 times more gravitational acceleration at large radii. This is consistent with the results from Eckert et al. [6] who estimates that the dynamical mass was underestimated above 1 Mpc. This additional acceleration could be due to the fact that the gas may be clumpy rather than smooth and also by modifications to the pressure due to phenomena such as the bulk motion of the gas.
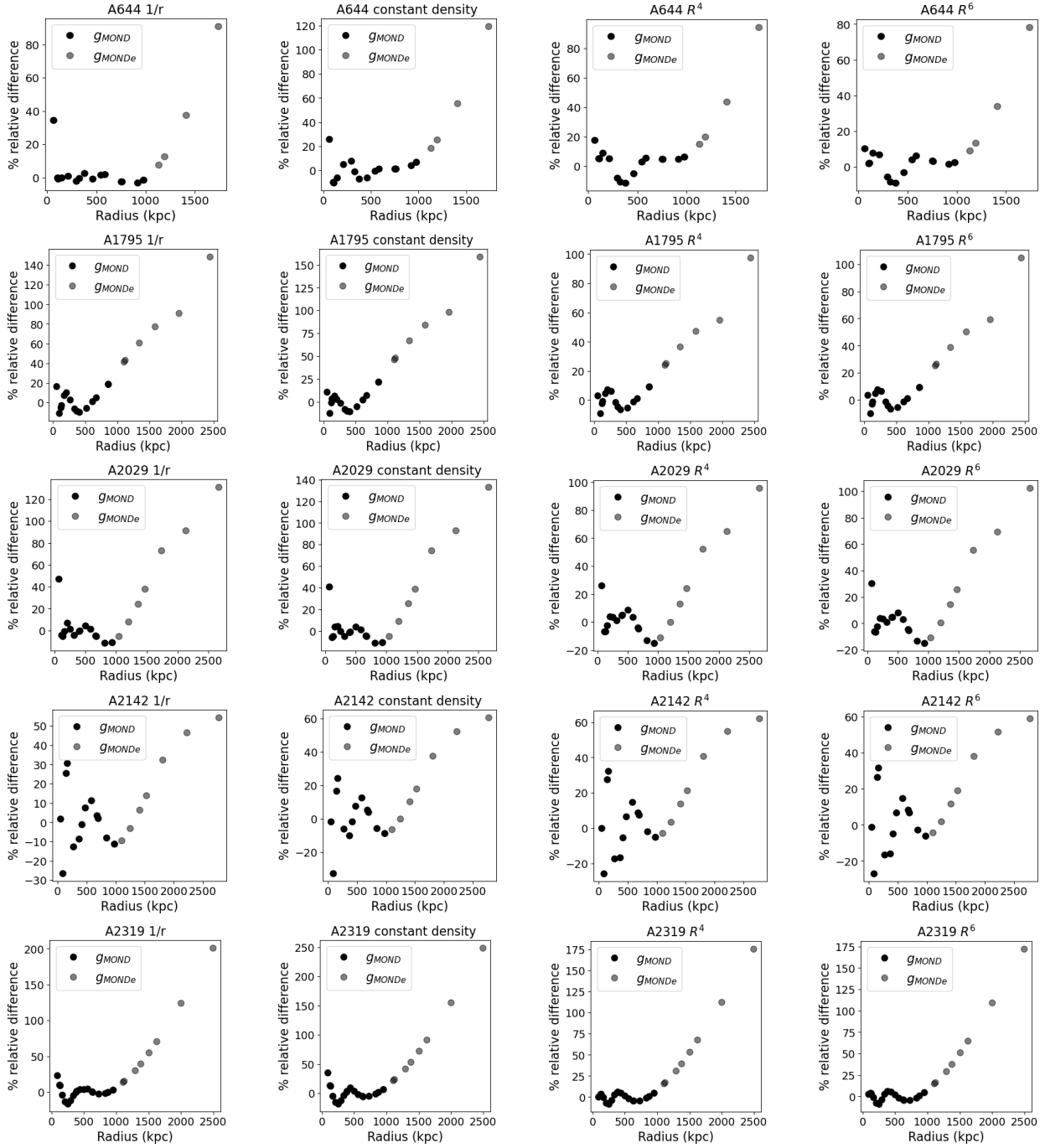
Figure 4.9: An estimation of the hydrostatic bias by calculating the percentage relative difference between the model and the data. The black points are those from the data up to 1 Mpc and the grey points are from the data beyond 1 Mpc.

Table 4.5: Correlation coefficients of M_{mm} and R_s from the best fit $1/R^4$ model, with T_{3D}, T_{vir} and T_{spec}. The p-value is quoted alongside its coefficient.

	$\mathbf{T_{3D}}$		$\mathbf{T_{vir}}$		$\mathbf{T_{spec}}$	
	$\mathbf{M_{mm}}$	$\mathbf{R_s}$	$\mathbf{M_{mm}}$	$\mathbf{R_s}$	$\mathbf{M_{mm}}$	$\mathbf{R_s}$
Pearson	0.623	0.824	0.607	0.817	0.106	0.575
P-value	0.262	0.086	0.278	0.092	0.865	0.310
Spearman	0.600	0.900	0.6	0.900	0.3	0.800
P-value	0.285	0.037	0.285	0.037	0.624	0.104
Kendall	0.400	0.800	0.400	0.800	0.200	0.600
P-value	0.483	0.083	0.483	0.083	0.187	0.233

4.4.3 Correlation tests

In order to determine the nature of the missing mass M_{mm}, the best fit values of M_{mm} and r_s were plotted against the stellar mass, gas mas, baryonic mass, luminosity, spectroscopic temperature, Virial temperature and T_{3D}. This was only done for the $1/R^4$ data because it is the most favorable model. The only plots that showed any sort of correlation were the plots against the various temperatures: T_{3D}, T_{vir} and T_{spec}. In order to determine the strength of these correlations, a number of correlation tests were performed and presented in Table 4.5.

The first test was Pearson's correlation coefficient which measures the strength and direction of the linear relationship between two variables. The coefficient runs from -1 to 1. A value of -1 indicates strong negative linear correlation, a value close to 0 indicates no or weak correlation and a value of 1 indicates a strong positive linear correlation. The second test was the Spearman coefficient. This coefficient measures the strength and direction of the monotonic relationship between two variables. This also runs from -1 to 1, -1 being strong negative monotonic relationship and 1 being strong positive monotonic relationship as before. The last test performed was Kendall's coefficient. This measures the correspondence between two rankings. Values close to 1 indicate strong agreement, values close to -1 indicate strong disagreement. While Kendall's correlation measures the rank correlation, it does not necessarily imply a linear relationship. This coefficient also ranges from -1 to 1.

The p-value was calculated alongside all of the coefficients. The reason that the

p-value is slightly different for each test is that they all make different assumptions about the data. The Pearson test assumes a linear relationship in the data but the Kendall and Spearman do not. In addition, the sample size affects the p-value and the sample size here is only 5, so the p-values are less precise and vary more between tests.

The results from the Kendall coefficient test are small which would indicate a moderate to weak positive rank correlation between the two datasets. However looking to the p-value being much larger than 0.05, the usual significance level, the evidence is too weak to conclude that the observed correlation is statistically significant. However if we test at 10% significance, which may be fairer considering the small sample size, there is correlation between R_s and T_{3D} and R_s and T_{vir}. The same can be said for the Pearson test, testing at 10% significance level there is also correlation between R_s and T_{3D} and R_s and T_{vir}. Looking to the Spearman test there are the same correlations as well as T_{spec} and R_s. These tests would therefore indicate that there is indeed a correlation between the scale radius and the temperature. From the Pearson test it would indicate a linear relationship and from the other two tests it is likely that it is a positive monotonic relationship.
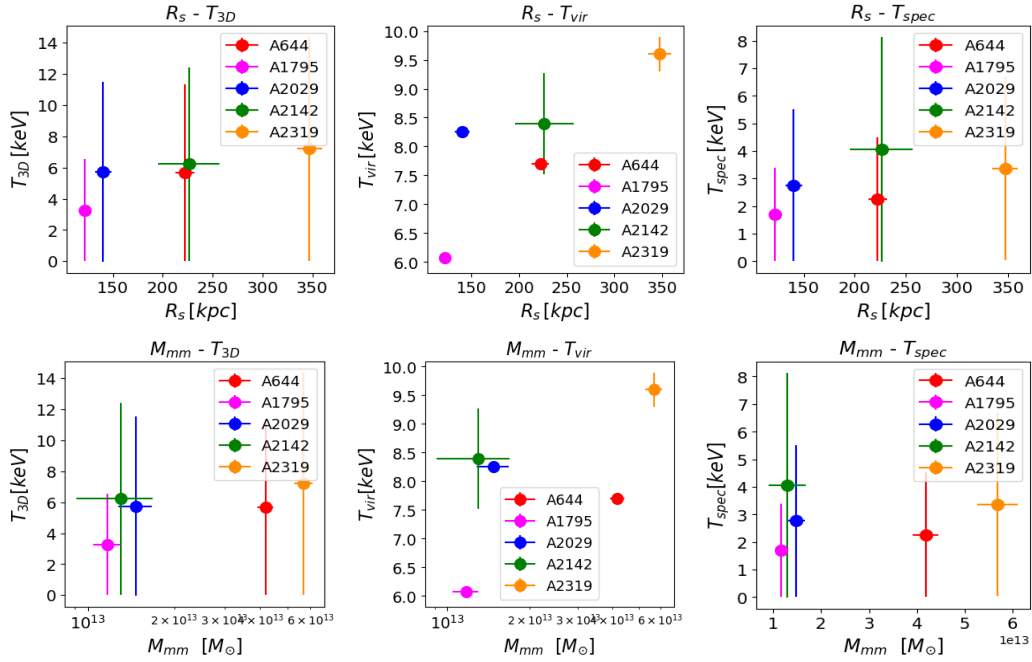
Figure 4.10: Correlation plots of the R_s and M_{mm} values taken from the $1/R^4$ model with the various temperatures

These plots are included in Figure 4.10. The data for T_{3D} and T_{spec} was provided by Dr. D. Eckert and T_{vir} was found in Eckert et al. [76]. The errors are of the

same order of magnitude as the 3D temperature and spectroscopic temperature from Eckert which makes the correlation and strength slightly less significant. The error for the virial temperatures are much smaller and so this relationship is much clearer.

Although the p-values for the M_{mm} tests are quite large, it is still intriguing that the values for the coefficients were of the order 0.6 for the Spearman and Pearson tests. The values would indicate a linear relationship as inferred from the Pearson test and the Spearman would indicate it to be a positive monotonic relationship. The p-value for these figures is approximately 0.27, so it is too large to infer any strong correlations, but this may be due to the small sample size.

4.5 Corner Plots
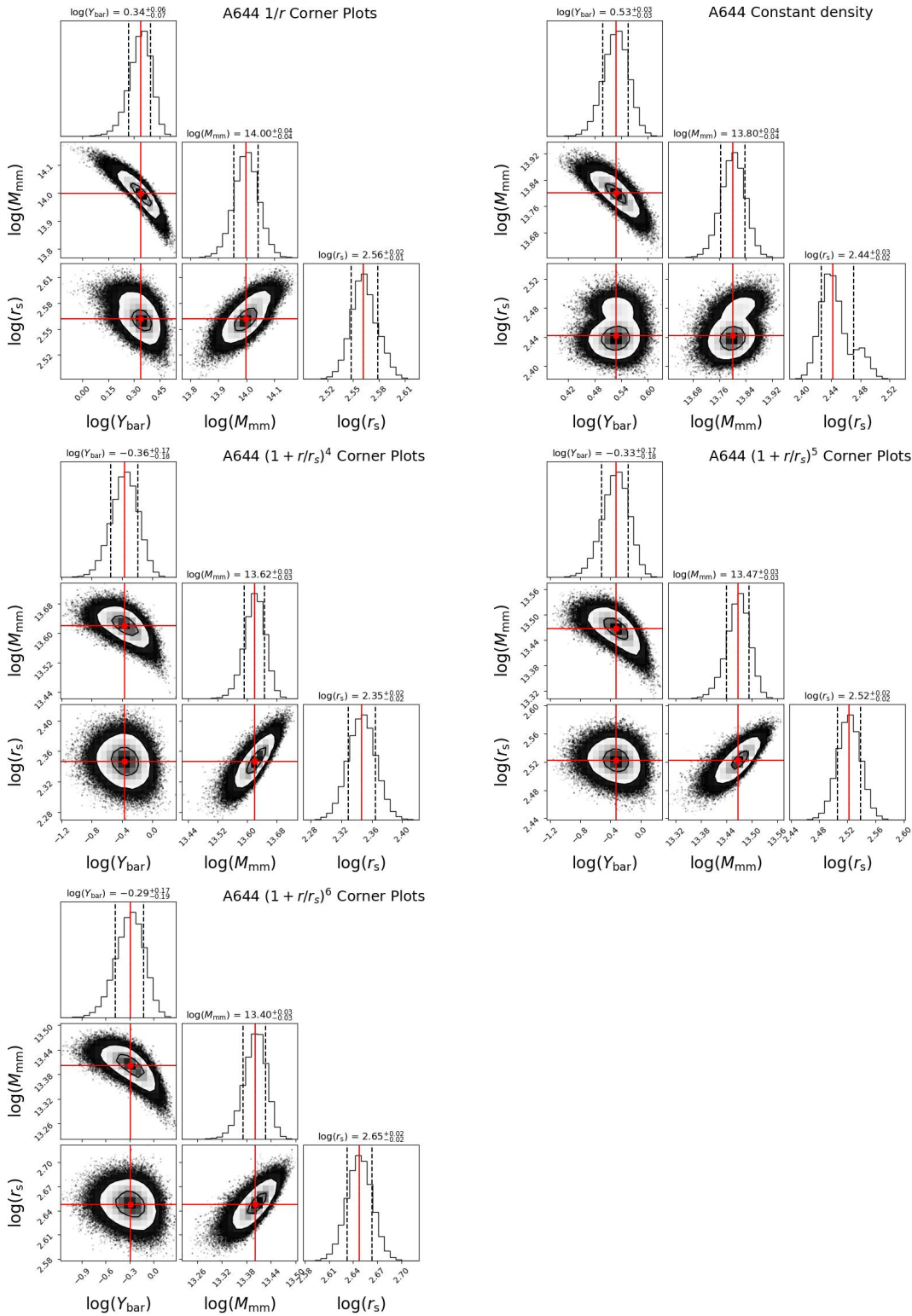
Figure 4.11: The Corner plots for A644. The best fit value is represented as a red dot at the centre of the cross on the 2D projection of the posterior probabilities. This best fit value is printed above the 1D projections of the posterior probabilities. The solid red line in the 1D projections represents the best fit value, along with the dashed lines on either side representing the 16th and 84th quantile.
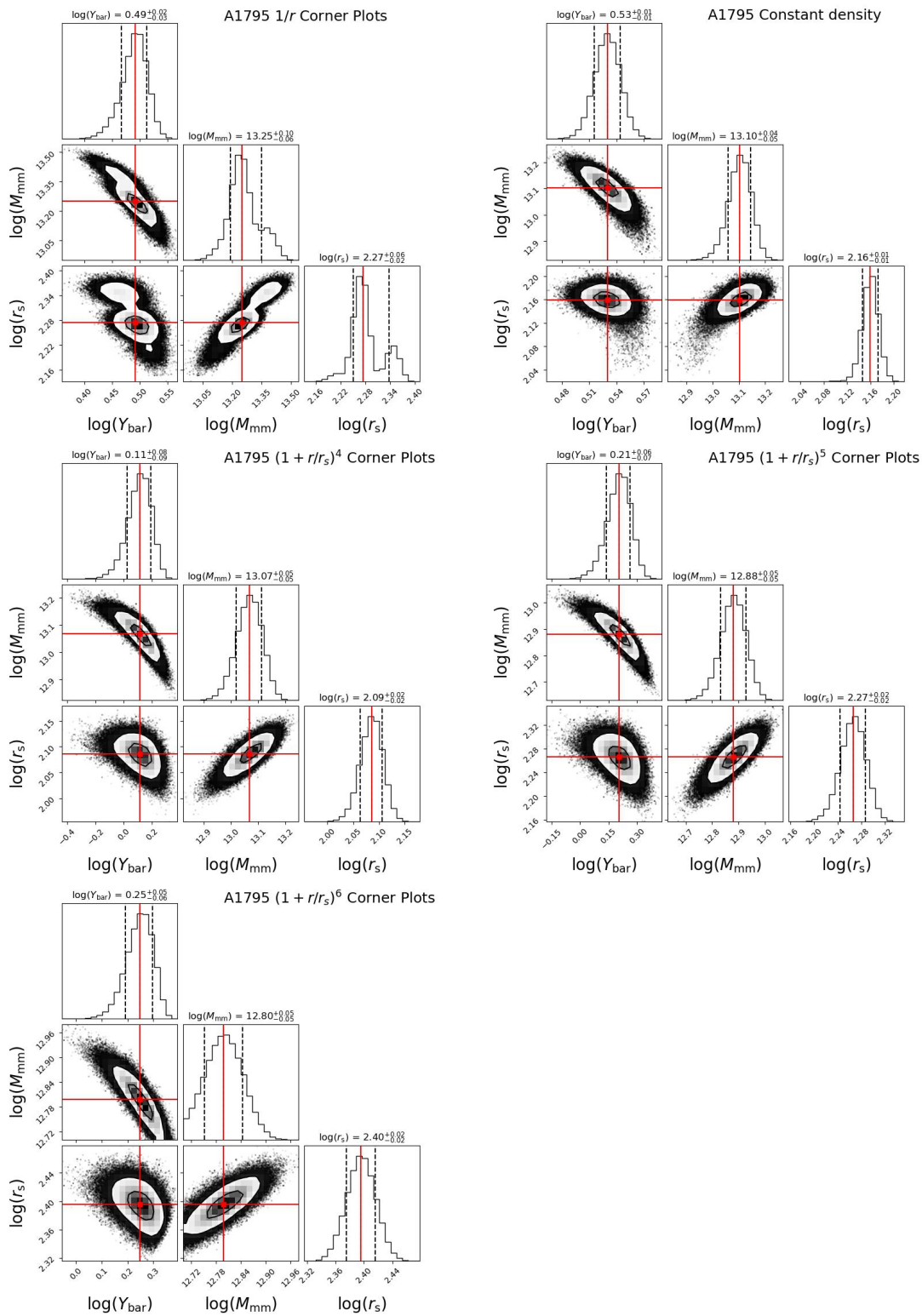
Figure 4.12: The Corner plots for A1795. The best fit value is represented as a red dot at the centre of the cross on the 2D projection of the posterior probabilities. This best fit value is printed above the 1D projections of the posterior probabilities. The solid red line in the 1D projections represents the best fit value, along with the dashed lines on either side representing the 16th and 84th quantile.
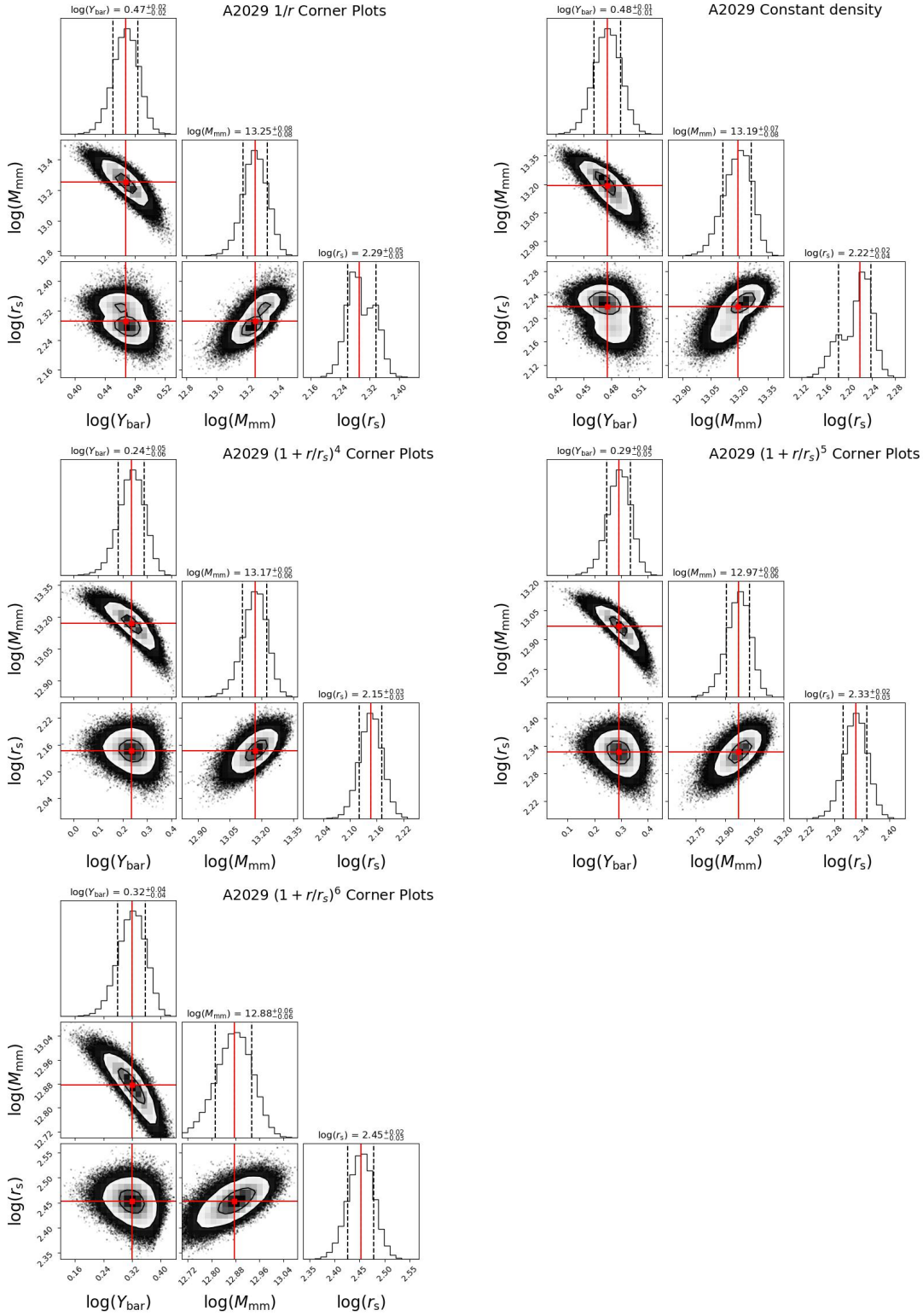
Figure 4.13: The Corner plots for A2029. The best fit value is represented as a red dot at the centre of the cross on the 2D projection of the posterior probabilities. This best fit value is printed above the 1D projections of the posterior probabilities. The solid red line in the 1D projections represents the best fit value, along with the dashed lines on either side representing the 16th and 84th quantile.
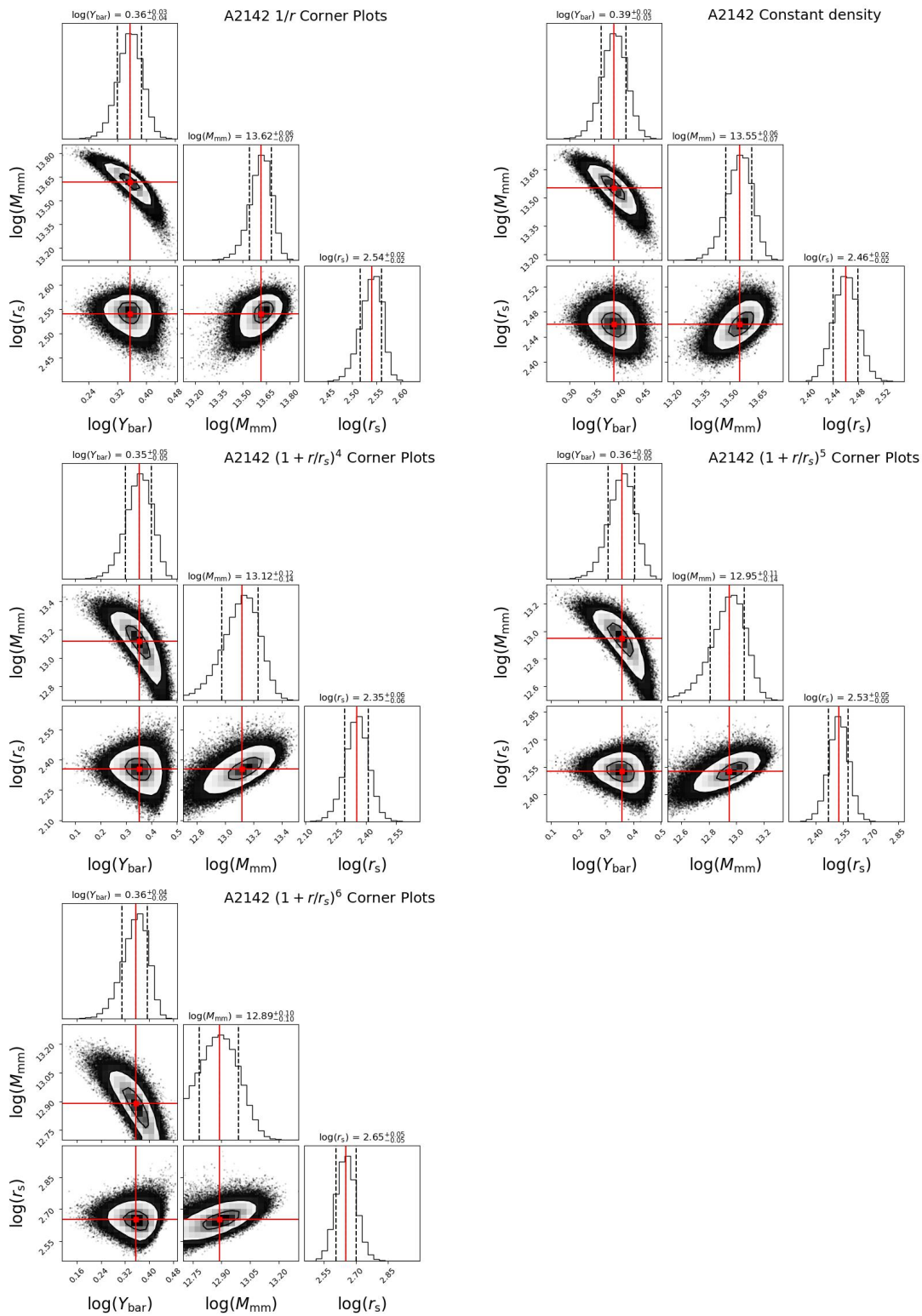
Figure 4.14: The Corner plots for A2142. The best fit value is represented as a red dot at the centre of the cross on the 2D projection of the posterior probabilities. This best fit value is printed above the 1D projections of the posterior probabilities. The solid red line in the 1D projections represents the best fit value, along with the dashed lines on either side representing the 16th and 84th quantile.
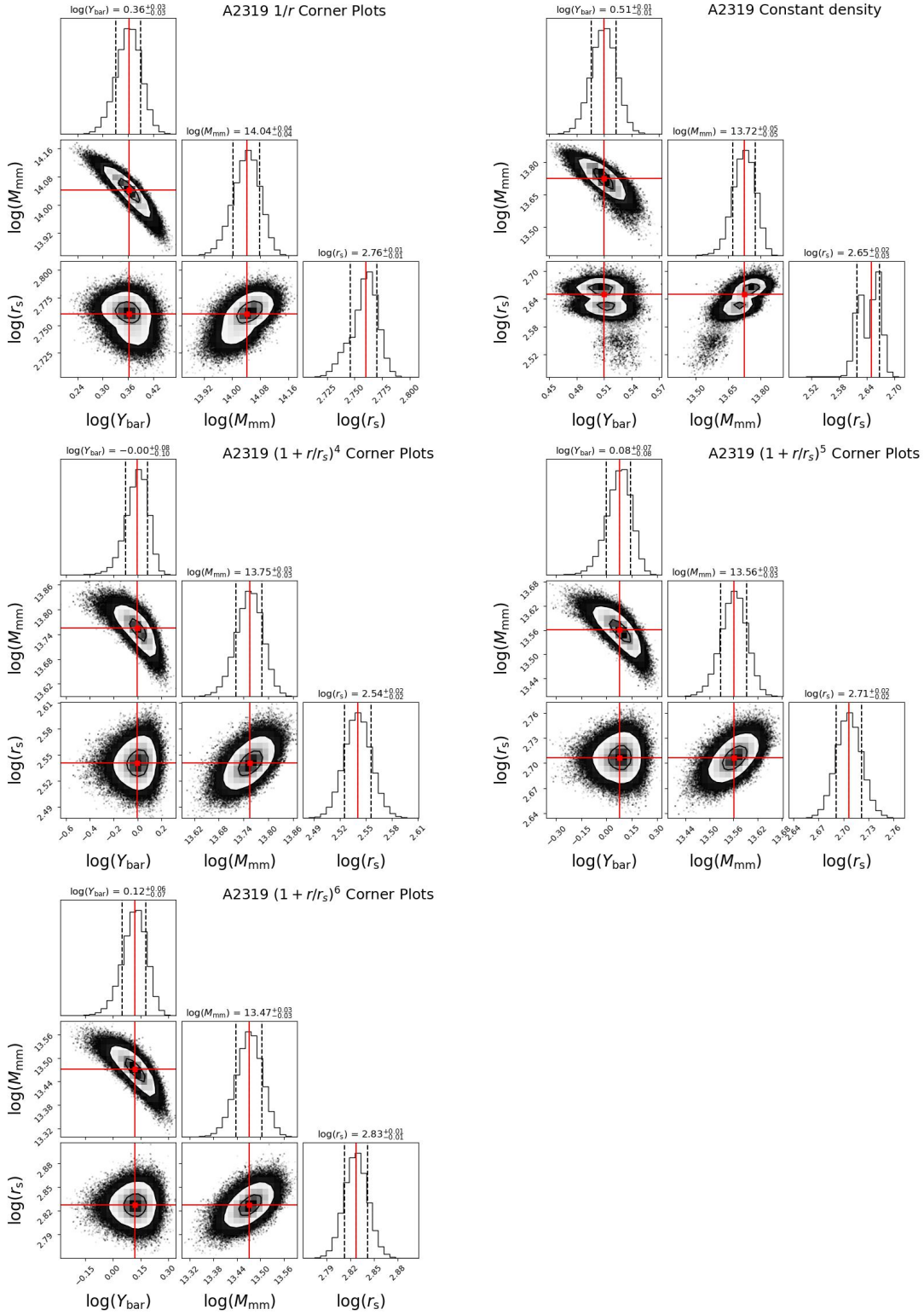
Figure 4.15: The Corner plots for A2319. The best fit value is represented as a red dot at the centre of the cross on the 2D projection of the posterior probabilities. This best fit value is printed above the 1D projections of the posterior probabilities. The solid red line in the 1D projections represents the best fit value, along with the dashed lines on either side representing the 16th and 84th quantile.

5

Discussion and Conclusions

The hypothesised theory of cold dark matter is the cornerstone of ΛCDM cosmology. DM is reported by many as confirmed and widely accepted in the scientific community. However, the lack of direct laboratory evidence of this enigmatic particle, as well as some shortcomings of ΛCDM, has lead to a search for other explanations. This thesis investigated one such explanation known as MOND. This theory was tested in the context of galaxy clusters, as it has been known to have great success in reproducing galactic rotation curves, but less success with galaxy clusters. The standard Newtonian approach has been investigated alongside the theory of MOND in order to determine whether one theory wins out. In this Chapter, I discuss the various successes and problems with the two approaches adopted in this thesis, and also in the context of the wider field of research of the dark matter problem.

5.1   Model Comparison

A number of density profiles were fit to the clusters under Newtonian dynamics and Milgromian dynamics. Their BIC values were calculated in order to quantitatively compare the most preferred model. Since it was determined that there was likely some hydrostatic bias in the outskirts of the clusters, the BIC values quoted in Table 5.1 are those from the fits using the data up to 1 Mpc. This is a more fair comparison of the models because the BIC depends on the size of the dataset.

As expected, the baryonic scaling model is the worst fit model by quite a large margin, in both the Newtonian and Milgromian case. However it is noteworthy

Table 5.1: Average BIC values for data < 1 Mpc for Newtonian and Milgromian models

Newtonian Model	Average BIC	Milgromian Model	Average BIC
Baryonic scaling	-655.995	Baryonic Scaling	-676.410
pISO	-711.949	$1/r$	-699.573
Burkert	-704.026	Constant density	-698.916
Lucky13	-708.003	$1/R^4$	-714.442
NFW	-706.945	$1/R^5$	-713.126
Einasto	-707.856	$1/R^6$	-706.344

Table 5.2: Baryonic scaling Υ values from the two approaches

Cluster	Newtonian Υ_{bar}	Milgromian Υ_{bar}
A644	$7.963^{+1.009}_{-0.991}$	$4.826^{+1.0188}_{-0.981}$
A1795	$10.023^{+1.012}_{-0.988}$	$4.244^{+1.0134}_{-0.987}$
A2029	$7.228^{+1.006}_{-0.994}$	$3.558^{+1.0123}_{-0.988}$
A2142	$5.888^{+1.009}_{-0.991}$	$3.201^{+1.0198}_{-0.980}$
A2319	$6.209^{+1.013}_{-0.987}$	$3.800^{+1.00997}_{-0.990}$

that the Milgromian baryonic scaling model is a better fit than the Newtonian one. This is a positive result for MOND, as MOND is constructed in a way to try and minimise the amount of missing matter needed. This is also seen in the fact that the Υ_{bar} values are smaller in the Milgromian models as shown in Table 5.2. The Υ_{bar} value was decreased by approximately a factor of two in most cases. However, this value is still too large to be a reasonable mass-to-light ratio because one would expect $\Upsilon_{bar} \approx 1$ with small variations (of the order 20-30%) to account for errors on the baryonic mass in the ICM and individual galaxies. This result is consistent with previous studies performed on galaxy clusters in a MOND context (e.g. Sanders [69]); the need for additional missing mass is null for galaxies, but for galaxy clusters it is still required.

For the same number of fitting parameters (equal to three in all models that were tested) the smaller the BIC, the better the model fits the data, and so the more negative the number in this case, the better the fit. In general, the BIC values for the Newtonian models are all less than -700, so this could point to those models in general being better descriptions of the data. This goes hand-in-hand with the corner plots. The corner plots of the models in Chapter 3 are much more well behaved than those in Chapter 4; the 1D histograms in Chapter 3 were very close to gaussians and the 2D distributions were mostly circular. Within the Newtonian models, the pseudo-isothermal model was still the best fit model having used the

data up to 1 Mpc. This cored profile is still preferred to the cusped NFW and Einasto. This confirmed that the well known "cusp-core problem", that has been observed in galaxies, is also observed in galaxy clusters. This is an outstanding problem with ΛCDM. There is no strong preference between the NFW and Einasto profiles. They have a very weak preference over the cored Burkert profile. The Lucky13 profile is slightly preferred over the NFW but these are weak preferences.

The model which best describes the data overall according to the BIC values is the $1/R^4$ model (or almost equally the $1/R^5$ model). This model has a strong preference over the pseudo-isothermal profile from the Newtonian models. This would be a very promising result for MOND, except that the MOND models had a free parameter M_{mm} for the missing mass. It is a well established criticism of MOND that it still requires some missing mass in galaxy clusters. At the same time, it is relevant that this M_{mm} mass is of the order 10^{13} as quoted from the best fit parameters in Table 4.2. With reference to Table 3.1 of the best fit parameters for the halo mass M_{200}, these were of the order 10^{15}, so MOND requires much less missing mass than the ΛCDM Newtonian approach.

5.2 Successes and Issues of the ΛCDM paradigm

The successes of the ΛCDM model in Chapter 3 must be highlighted. In particular, with reference to Figure 3.7 which shows the mass-concentration relation, almost all of the clusters lie within 1σ of the expected relation, with cluster A2142 being an outlier. This means that if the clusters are described using the NFW or Einasto halo, they follow the expected mass-concentration relation. This relation states that massive halos are predicted to have lower concentrations, while less massive halos tend to have higher concentrations. This may appear as a great success for the ΛCDM model, but the NFW or Einasto profiles were not the best fit models for the data. The cored profiles, in particular the pseudo-isothermal profile, turned out to be the most preferred profile. So although the mass-concentration relation was found to hold for these clusters, it does not mean that the cusped profiles fit the data any better than the cored ones.

The preference for the cored profiles has been noted by many on galaxy scales and named the "cusp-core problem". This is a long standing issue of ΛCDM for which there is still no clear explanation. On galaxy scales, a possible solution is strong baryonic feedback that may remove large amounts of baryons from the central regions, cause oscillations in the total gravitational potential, and eventually lead to the formation of DM cores. On cluster scales, it is intriguing that this preference for cored profiles is also found. This may be contributing to a re-evaluation of the structure formation scenario in ΛCDM and the effect of baryonic physics. Adding

to this, massive clusters have been discovered at redshifts larger than 1, for example cluster XMMU J2235.3-2557 from Rosati et al. [77]. The presence of this cluster at such a large redshift further demands a reevaluation of the timeline of structure formation that has been described by ΛCDM.

The possible problems in the current theory of structure formation could also be seen in the results obtained for the stellar-to-halo mass relation. This relation describes the connection between the mass of the dark matter halo and the mass of stars within the central galaxy. In ΛCDM, galaxies form in the halos by accretion and by mergers and then the stars are formed from these galaxies. This relationship therefore is integral to understanding galaxy formation and subsequent galaxy cluster formation. The deviation that is seen in Figure 3.9 could point to the fact that the NFW and Einasto halos were not the best descriptions of the data and therefore would not follow the relation, or the fact that this is not a universal property. This would point to a problem with the structure formation scenario in ΛCDM.

5.3 Successes and Issues of the MOND paradigm

As we have previously discussed, MOND can fit the cluster data as long as there is an additional component with 2-4 times more mass than the ICM. A possible candidate particle to account for the missing mass is an 11 eV sterile neutrino. This neutrino is separate to the three flavours of neutrinos that are already part of the standard model. The sterile neutrino is so called because it does not interact electromagnetically or through the weak force. This does make this particle difficult to detect. Theoretically, it is a viable option and has had success in recreating the current level of precision in the measurements of the CMB anisotropies. It is also consistent with a structure formation scenario in MOND. [71]

Another possible candidate for this matter is that of "dark baryons" in the form of compact clouds of cold gas. These theorised baryons would only be present in clusters and not in spiral galaxies, but Milgrom [70] posits that this may be allowed as these two objects are very different in terms of baryonic content and likely the formation processes. Milgrom [70] also proposes that since the mass of the dark baryons that is required is similar to that of the hot gas in clusters, that there is some process in which a fraction of the baryons have somehow transformed into the cool dark clouds of baryons. This does not happen in spirals but it may be relevant for ellipticals which contain some hot gas. Since there seems to be some correlation between this M_{mm} (and r_s) with the temperature of the hot gas in the clusters as seen in Section 4.4.3, this candidate may have stronger evidence than the sterile neutrino.

Importantly, both sterile neutrinos and compact clouds of cold gas behave as

collisionless particles so they may be used to explain the bullet cluster in a MOND context. There are modifications that can be made to the standard MOND formalism in which the observations of the Bullet cluster can be explained. One of these is a relativistic theory that is based in a tensor-vector-scalar field theory known as TeVeS. This theory is the relativistic extension to the AQUAL MOND theory described in Section 1.2.2. The total potential in this theory is given by $\Phi \approx \phi_N + \phi$ where ϕ_N is the Newtonain potential and ϕ is a dynamical scalar field. This ϕ is a stand-in for the dark matter gravitational potential in a MOND context. The Bullet cluster has three distinct mass distributions; the baryonic matter near the centre and the majority of the matter on either side of this. If we consider a triple-centred model for the potential Φ then a distribution very similar to that of the Bullet cluster can be achieved by only considering a baryonic density distribution. The full details can be found in Angus et al. [78]. The main point is that the Bullet cluster's mass distribution can be reproduced in other theories so it may not be the absolute proof of particle dark matter, as it was presented. [79]

In addition to the missing mass, the external field effect (EFE) in MOND may play a role to reproduce the dynamics of galaxy clusters. The concept of the external field effect is an interesting one, as it is not present in other gravitational theories e.g. in General Relativity. MOND theories directly violate the underlying assumption in GR of the strong equivalence principle so the EFE emerges, whereas the weak equivalence principle and the Einstein equivalence principle still hold. The introduction of the EFE in this thesis came about when we tried to directly infer the mass profile of the missing mass component. It was found that these missing mass profiles were decreasing, which is unphysical and would lead to MOND not being a viable theory. In order to rectify this, the external field effect was investigated.

In MOND, one finds that the internal dynamics of a galaxy or a cluster are affected by its environment. Once the MOND equations in an EFE context were applied to the missing mass profiles, there were varying degrees of improvement, but in every case there was some improvement. The most successful case was from cluster A2142, whereby applying an external field of just $0.1a_0$ the mass profile went from negative to flat, and with an external field of $0.3a_0$, it was increasing.

The case of A2319 had the least amount of improvement. This cluster, however, is undergoing a merging event and so the dynamics in the outskirts are more complicated. As stated in Section 4.4.2, in order to explain the decreasing mass profiles for the missing mass in a different way, an investigation into hydrostatic bias was performed. It is likely that there is some level of bias in the outskirts of these galaxies, which may be causing the decreasing mass profiles. However an interesting point that was discovered here was that A2319 needed a much larger amount of gravitational acceleration in the furthest outskirts as compared to the other clusters. This could mean that MOND may have the ability to detect whether clusters are

undergoing mergers in the outskirts, by determining the amount of gravitational acceleration that is needed in the outskirts, in order to make the mass profile not decrease.

5.4   Extensions and Future work

There are many other avenues that could be explored starting from the work done in this thesis. The simplest extension to this would be to test more models, under Newtonian dynamics and Milgromian dynamics. In particular, with regards to the Milgromian dynamics, it would be interesting to investigate the external field effect in more detail. Also, it would be of interest to see whether clusters that are known to be undergoing mergers would follow the same results as A2319, or if this method could predict whether it is undergoing a merger in the outskirts. It would also be worthwhile to use the MOND equations which are derived taking the external field effect in account as seen in Chae et al. [80]. The interpolating function for these equations is a function of the gravitational external field. This value for g_{ext} would be a free parameter in the fits and would explore various priors to better determine its behaviour. A larger sample size of galaxy clusters would also greatly improve the strength of the conclusions that could be drawn.

Issues that occur in the ΛCDM model do not necessarily add credit to MOND and vice versa, but it is more important to show that this widely accepted theory is not completely successful. It has many successes such as an explanation for the CMB and its anisotropies, a theory of structure formation to account for LSS and nucleosynthesis to name a few. However it does have a number of outstanding issues as discussed above, as well as the problems of missing baryons, the empirical Tully-fisher relation and the observations from the bullet cluster. Some of these issues can be accounted for using MOND. Whether or not MOND is the best theory remains to be seen. This thesis set out to investigate whether or not it can compete with the widely accepted ΛCDM model on galaxy cluster scales.

References

[1] Vera C. Rubin and Jr. Ford, W. Kent. Rotation of the Andromeda Nebula from a Spectroscopic Survey of Emission Regions. , 159:379, February 1970. doi: 10.1086/150317.

[2] Hubblesite. Gravity of galaxy cluster abell 2218 creates giant lens. Available online. URL https://hubblesite.org/contents/media/images/2000/07/942-Image.html. Accessed on October 2, 2023.

[3] C. L. Bennett, D. Larson, J. L. Weiland, N. Jarosik, G. Hinshaw, N. Odegard, K. M. Smith, R. S. Hill, B. Gold, M. Halpern, E. Komatsu, M. R. Nolta, L. Page, D. N. Spergel, E. Wollack, J. Dunkley, A. Kogut, M. Limon, S. S. Meyer, G. S. Tucker, and E. L. Wright. Nine-year Wilkinson Microwave Anisotropy Probe (WMAP) Observations: Final Maps and Results. , 208(2): 20, October 2013. doi: 10.1088/0067-0049/208/2/20.

[4] Volker Springel, Simon D. M. White, Adrian Jenkins, Carlos S. Frenk, Naoki Yoshida, Liang Gao, Julio Navarro, Robert Thacker, Darren Croton, John Helly, John A. Peacock, Shaun Cole, Peter Thomas, Hugh Couchman, August Evrard, Jörg Colberg, and Frazer Pearce. Simulations of the formation, evolution and clustering of galaxies and quasars. , 435(7042):629–636, June 2005. doi: 10.1038/nature03597.

[5] Chandra X ray Observatory. Chandra images by category: Groups clusters of galaxies. Available online. URL https://chandra.si.edu/photo/category/galaxyclusters.html. Accessed on October 3, 2023.

[6] D. Eckert, S. Ettori, E. Pointecouteau, R. F. J. van der Burg, and S. I. Loubser. The gravitational field of X-COP galaxy clusters. , 662:A123, June 2022. doi: 10.1051/0004-6361/202142507.

[7] Angelo Secchi. *L'astronomia in Roma nel pontificato DI Pio IX.* 1877.

[8] H. Poincare. The Milky Way and the Theory of Gases. *Popular Astronomy*, 14:475–488, October 1906.

[9] J. H. Oort. The force exerted by the stellar system in the direction perpendicular to the galactic plane and some related problems. , 6:249, August 1932.

[10] Heinz Andernach and Fritz Zwicky. English and Spanish Translation of Zwicky's (1933) The Redshift of Extragalactic Nebulae. *arXiv e-prints*, art. arXiv:1711.01693, November 2017. doi: 10.48550/arXiv.1711.01693.

[11] Sinclair Smith. The Mass of the Virgo Cluster. , 83:23, January 1936. doi: 10.1086/143697.

[12] D. H. Rogstad and G. S. Shostak. Gross Properties of Five Scd Galaxies as Determined from 21-CENTIMETER Observations. , 176:315, September 1972. doi: 10.1086/151636.

[13] A. Bosma. *The distribution and kinematics of neutral hydrogen in spiral galaxies of various morphological types.* PhD thesis, University of Groningen, Netherlands, March 1978.

[14] V. C. Rubin, Jr. Ford, W. K., and N. Thonnard. Extended rotation curves of high-luminosity spiral galaxies. IV. Systematic dynamical properties, Sa -> Sc. , 225:L107–L111, November 1978. doi: 10.1086/182804.

[15] Katherine Garrett and Gintaras Dūda. Dark Matter: A Primer. *Advances in Astronomy*, 2011:968283, January 2011. doi: 10.1155/2011/968283.

[16] Anton G. Bergmann, Vahe Petrosian, and Roger Lynds. Gravitational Lens Models of Arcs in Clusters. , 350:23, February 1990. doi: 10.1086/168359.

[17] Douglas Clowe, Maruša Bradač, Anthony H. Gonzalez, Maxim Markevitch, Scott W. Randall, Christine Jones, and Dennis Zaritsky. A Direct Empirical Proof of the Existence of Dark Matter. , 648(2):L109–L113, September 2006. doi: 10.1086/508162.

[18] Chiara Mastropietro and Andreas Burkert. Simulating the Bullet Cluster. *Monthly Notices of the Royal Astronomical Society*, 389(2):967–988, 09 2008. ISSN 0035-8711. doi: 10.1111/j.1365-2966.2008.13626.x. URL https://doi.org/10.1111/j.1365-2966.2008.13626.x.

[19] Jounghun Lee and Eiichiro Komatsu. Bullet Cluster: A Challenge to ΛCDM Cosmology. , 718(1):60–65, July 2010. doi: 10.1088/0004-637X/718/1/60.

[20] Glennys R. Farrar and Rachel A. Rosen. A new force in the dark sector? *Phys. Rev. Lett.*, 98:171302, Apr 2007. doi: 10.1103/PhysRevLett.98.171302. URL https://link.aps.org/doi/10.1103/PhysRevLett.98.171302.

[21] Robert Thompson and Kentaro Nagamine. Pairwise velocities of dark matter haloes: a test for the Λ cold dark matter model using the bullet cluster. , 419 (4):3560–3570, February 2012. doi: 10.1111/j.1365-2966.2011.20000.x.

[22] J. P. Ostriker, P. J. E. Peebles, and A. Yahil. The Size and Mass of Galaxies, and the Mass of the Universe. , 193:L1, October 1974. doi: 10.1086/181617.

[23] G. F. Smoot, C. L. Bennett, A. Kogut, E. L. Wright, J. Aymon, N. W. Boggess, E. S. Cheng, G. de Amici, S. Gulkis, M. G. Hauser, G. Hinshaw, P. D. Jackson, M. Janssen, E. Kaita, T. Kelsall, P. Keegstra, C. Lineweaver, K. Loewenstein, P. Lubin, J. Mather, S. S. Meyer, S. H. Moseley, T. Murdock, L. Rokke, R. F. Silverberg, L. Tenorio, R. Weiss, and D. T. Wilkinson. Structure in the COBE Differential Microwave Radiometer First-Year Maps. , 396:L1, September 1992. doi: 10.1086/186504.

[24] A. Arbey and F. Mahmoudi. Dark matter and the early Universe: A review. *Progress in Particle and Nuclear Physics*, 119:103865, July 2021. doi: 10. 1016/j.ppnp.2021.103865.

[25] Planck Collaboration, N. Aghanim, Y. Akrami, M. Ashdown, J. Aumont, C. Baccigalupi, M. Ballardini, A. J. Banday, R. B. Barreiro, N. Bartolo, S. Basak, R. Battye, K. Benabed, J. P. Bernard, M. Bersanelli, P. Bielewicz, J. J. Bock, J. R. Bond, J. Borrill, F. R. Bouchet, F. Boulanger, M. Bucher, C. Burigana, R. C. Butler, E. Calabrese, J. F. Cardoso, J. Carron, A. Challinor, H. C. Chiang, J. Chluba, L. P. L. Colombo, C. Combet, D. Contreras, B. P. Crill, F. Cuttaia, P. de Bernardis, G. de Zotti, J. Delabrouille, J. M. Delouis, E. Di Valentino, J. M. Diego, O. Doré, M. Douspis, A. Ducout, X. Dupac, S. Dusini, G. Efstathiou, F. Elsner, T. A. Enßlin, H. K. Eriksen, Y. Fantaye, M. Farhang, J. Fergusson, R. Fernandez-Cobos, F. Finelli, F. Forastieri, M. Frailis, A. A. Fraisse, E. Franceschi, A. Frolov, S. Galeotta, S. Galli, K. Ganga, R. T. Génova-Santos, M. Gerbino, T. Ghosh, J. González-Nuevo, K. M. Górski, S. Gratton, A. Gruppuso, J. E. Gudmundsson, J. Hamann, W. Handley, F. K. Hansen, D. Herranz, S. R. Hildebrandt, E. Hivon, Z. Huang, A. H. Jaffe, W. C. Jones, A. Karakci, E. Keihänen, R. Keskitalo, K. Kiiveri, J. Kim, T. S. Kisner, L. Knox, N. Krachmalnicoff, M. Kunz, H. Kurki-Suonio, G. Lagache, J. M. Lamarre, A. Lasenby, M. Lattanzi, C. R. Lawrence, M. Le Jeune, P. Lemos, J. Lesgourgues, F. Levrier, A. Lewis, M. Liguori, P. B. Lilje, M. Lilley, V. Lindholm, M. López-Caniego, P. M. Lubin, Y. Z. Ma, J. F. Macías-Pérez, G. Maggio, D. Maino, N. Mandolesi, A. Mangilli, A. Marcos-Caballero, M. Maris, P. G. Martin, M. Martinelli, E. Martínez-González, S. Matarrese, N. Mauri, J. D. McEwen, P. R. Meinhold, A. Melchiorri, A. Mennella, M. Migliaccio, M. Millea, S. Mitra, M. A. Miville-Deschênes, D. Molinari, L. Montier, G. Morgante, A. Moss, P. Natoli, H. U. Nørgaard-Nielsen, L. Pagano, D. Paoletti, B. Partridge, G. Patanchon, H. V. Peiris, F. Perrotta, V. Pettorino, F. Piacentini, L. Polastri, G. Polenta, J. L. Puget, J. P. Rachen, M. Reinecke, M. Remazeilles,

A. Renzi, G. Rocha, C. Rosset, G. Roudier, J. A. Rubiño-Martín, B. Ruiz-Granados, L. Salvati, M. Sandri, M. Savelainen, D. Scott, E. P. S. Shellard, C. Sirignano, G. Sirri, L. D. Spencer, R. Sunyaev, A. S. Suur-Uski, J. A. Tauber, D. Tavagnacco, M. Tenti, L. Toffolatti, M. Tomasi, T. Trombetti, L. Valenziano, J. Valiviita, B. Van Tent, L. Vibert, P. Vielva, F. Villa, N. Vittorio, B. D. Wandelt, I. K. Wehus, M. White, S. D. M. White, A. Zacchei, and A. Zonca. Planck 2018 results. VI. Cosmological parameters. , 641:A6, September 2020. doi: 10.1051/0004-6361/201833910.

[26] Kevork N. Abazajian, Jennifer K. Adelman-McCarthy, Marcel A. Agüeros, Sahar S. Allam, Carlos Allende Prieto, Deokkeun An, Kurt S. J. Anderson, Scott F. Anderson, James Annis, Neta A. Bahcall, C. A. L. Bailer-Jones, J. C. Barentine, Bruce A. Bassett, Andrew C. Becker, Timothy C. Beers, Eric F. Bell, Vasily Belokurov, Andreas A. Berlind, Eileen F. Berman, Mariangela Bernardi, Steven J. Bickerton, Dmitry Bizyaev, John P. Blakeslee, Michael R. Blanton, John J. Bochanski, William N. Boroski, Howard J. Brewington, Jarle Brinchmann, J. Brinkmann, Robert J. Brunner, Tamás Budavári, Larry N. Carey, Samuel Carliles, Michael A. Carr, Francisco J. Castander, David Cinabro, A. J. Connolly, István Csabai, Carlos E. Cunha, Paul C. Czarapata, James R. A. Davenport, Ernst de Haas, Ben Dilday, Mamoru Doi, Daniel J. Eisenstein, Michael L. Evans, N. W. Evans, Xiaohui Fan, Scott D. Friedman, Joshua A. Frieman, Masataka Fukugita, Boris T. Gänsicke, Evalyn Gates, Bruce Gillespie, G. Gilmore, Belinda Gonzalez, Carlos F. Gonzalez, Eva K. Grebel, James E. Gunn, Zsuzsanna Györy, Patrick B. Hall, Paul Harding, Frederick H. Harris, Michael Harvanek, Suzanne L. Hawley, Jeffrey J. E. Hayes, Timothy M. Heckman, John S. Hendry, Gregory S. Hennessy, Robert B. Hindsley, J. Hoblitt, Craig J. Hogan, David W. Hogg, Jon A. Holtzman, Joseph B. Hyde, Shin-ichi Ichikawa, Takashi Ichikawa, Myungshin Im, Željko Ivezić, Sebastian Jester, Linhua Jiang, Jennifer A. Johnson, Anders M. Jorgensen, Mario Jurić, Stephen M. Kent, R. Kessler, S. J. Kleinman, G. R. Knapp, Kohki Konishi, Richard G. Kron, Jurek Krzesinski, Nikolay Kuropatkin, Hubert Lampeitl, Svetlana Lebedeva, Myung Gyoon Lee, Young Sun Lee, R. French Leger, Sébastien Lépine, Nolan Li, Marcos Lima, Huan Lin, Daniel C. Long, Craig P. Loomis, Jon Loveday, Robert H. Lupton, Eugene Magnier, Olena Malanushenko, Viktor Malanushenko, Rachel Mandelbaum, Bruce Margon, John P. Marriner, David Martínez-Delgado, Takahiko Matsubara, Peregrine M. McGehee, Timothy A. McKay, Avery Meiksin, Heather L. Morrison, Fergal Mullally, Jeffrey A. Munn, Tara Murphy, Thomas Nash, Ada Nebot, Jr. Neilsen, Eric H., Heidi Jo Newberg, Peter R. Newman, Robert C. Nichol, Tom Nicinski, Maria Nieto-Santisteban, Atsuko Nitta, Sadanori Okamura, Daniel J. Oravetz, Jeremiah P. Ostriker,

Russell Owen, Nikhil Padmanabhan, Kaike Pan, Changbom Park, George Pauls, Jr. Peoples, John, Will J. Percival, Jeffrey R. Pier, Adrian C. Pope, Dimitri Pourbaix, Paul A. Price, Norbert Purger, Thomas Quinn, M. Jordan Raddick, Paola Re Fiorentin, Gordon T. Richards, Michael W. Richmond, Adam G. Riess, Hans-Walter Rix, Constance M. Rockosi, Masao Sako, David J. Schlegel, Donald P. Schneider, Ralf-Dieter Scholz, Matthias R. Schreiber, Axel D. Schwope, Uroš Seljak, Branimir Sesar, Erin Sheldon, Kazu Shimasaku, Valena C. Sibley, A. E. Simmons, Thirupathi Sivarani, J. Allyn Smith, Martin C. Smith, Vernesa Smolčić, Stephanie A. Snedden, Albert Stebbins, Matthias Steinmetz, Chris Stoughton, Michael A. Strauss, Mark SubbaRao, Yasushi Suto, Alexander S. Szalay, István Szapudi, Paula Szkody, Masayuki Tanaka, Max Tegmark, Luis F. A. Teodoro, Aniruddha R. Thakar, Christy A. Tremonti, Douglas L. Tucker, Alan Uomoto, Daniel E. Vanden Berk, Jan Vandenberg, S. Vidrih, Michael S. Vogeley, Wolfgang Voges, Nicole P. Vogt, Yogesh Wadadekar, Shannon Watters, David H. Weinberg, Andrew A. West, Simon D. M. White, Brian C. Wilhite, Alainna C. Wonders, Brian Yanny, D. R. Yocum, Donald G. York, Idit Zehavi, Stefano Zibetti, and Daniel B. Zucker. The Seventh Data Release of the Sloan Digital Sky Survey. , 182(2):543–558, June 2009. doi: 10.1088/0067-0049/182/2/543.

[27] Gianfranco Bertone and Dan Hooper. History of dark matter. *Reviews of Modern Physics*, 90(4):045002, October 2018. doi: 10.1103/RevModPhys.90.045002.

[28] J. G. de Swart, G. Bertone, and J. van Dongen. How dark matter came to matter. *Nature Astronomy*, 1:0059, March 2017. doi: 10.1038/s41550-017-0059.

[29] M. Milgrom. A modification of the Newtonian dynamics as a possible alternative to the hidden mass hypothesis. , 270:365–370, July 1983. doi: 10.1086/161130.

[30] M. Milgrom. A modification of the Newtonian dynamics - Implications for galaxies. , 270:371–383, July 1983. doi: 10.1086/161131.

[31] M. Milgrom. A modification of the newtonian dynamics : implications for galaxy systems. , 270:384–389, July 1983. doi: 10.1086/161132.

[32] J. Bekenstein and M. Milgrom. Does the missing mass problem signal the breakdown of Newtonian gravity? , 286:7–14, November 1984. doi: 10.1086/162570.

[33] M. Milgrom. MOND as modified inertia. In Gary A. Mamon, Francoise Combes, Cedric Deffayet, and Bernard Fort, editors, *EAS Publications Series*,

volume 20 of *EAS Publications Series*, pages 217–224, January 2006. doi: 10.1051/eas:2006074.

[34] Mordehai Milgrom. Nonlinear conformally invariant generalization of the Poisson equation to D>2 dimensions. , 56(1):1148–1159, July 1997. doi: 10.1103/PhysRevE.56.1148.

[35] Mordehai Milgrom. On the Use of Galaxy Rotation Curves to Test the Modified Dynamics. , 333:689, October 1988. doi: 10.1086/166777.

[36] S. M. Kent. Dark matter in spiral galaxies. I. Galaxies with optical rotation curves. , 91:1301–1327, June 1986. doi: 10.1086/114106.

[37] Federico Lelli. Gas dynamics in dwarf galaxies as testbeds for dark matter and galaxy evolution. *Nature Astronomy*, 6:35–47, January 2022. doi: 10. 1038/s41550-021-01562-2.

[38] Mordehai Milgrom. The a_0 – cosmology connection in MOND. *arXiv e-prints*, art. arXiv:2001.09729, January 2020. doi: 10.48550/arXiv.2001.09729.

[39] Mordehai Milgrom. The Mond Limit from Spacetime Scale Invariance. , 698 (2):1630–1638, June 2009. doi: 10.1088/0004-637X/698/2/1630.

[40] Mordehai Milgrom. MOND — a Pedagogical Review. *Acta Physica Polonica B*, 32(11):3613, November 2001. doi: 10.48550/arXiv.astro-ph/0112069.

[41] Mordehai Milgrom. MOND laws of galactic dynamics. , 437(3):2531–2541, January 2014. doi: 10.1093/mnras/stt2066.

[42] Mordehai Milgrom. MOND theory. *Canadian Journal of Physics*, 93(2):107–118, February 2015. doi: 10.1139/cjp-2014-0211.

[43] Mordehai Milgrom. Quasi-linear formulation of MOND. , 403(2):886–895, April 2010. doi: 10.1111/j.1365-2966.2009.16184.x.

[44] Mordehai Milgrom. General virial theorem for modified-gravity MOND. , 89 (2):024016, January 2014. doi: 10.1103/PhysRevD.89.024016.

[45] Mordehai Milgrom. Modified Dynamics Predictions Agree with Observations of the H i Kinematics in Faint Dwarf Galaxies Contrary to the Conclusions of Lo, Sargent, and Young. , 429:540, July 1994. doi: 10.1086/174341.

[46] M. Milgrom. Dynamics with a Nonstandard Inertia-Acceleration Relation: An Alternative to Dark Matter in Galactic Systems. *Annals of Physics*, 229 (2):384–415, February 1994. doi: 10.1006/aphy.1994.1012.

[47] Stephen Walker, Aurora Simionescu, Daisuke Nagai, Nobuhiro Okabe, Dominique Eckert, Tony Mroczkowski, Hiroki Akamatsu, Stefano Ettori, and Vittorio Ghirardini. The Physics of Galaxy Cluster Outskirts. , 215(1):7, January 2019. doi: 10.1007/s11214-018-0572-8.

[48] Andrey V. Kravtsov and Stefano Borgani. Formation of Galaxy Clusters. , 50:353–409, September 2012. doi: 10.1146/annurev-astro-081811-125502.

[49] Piero Rosati, Stefano Borgani, and Colin Norman. The Evolution of X-ray Clusters of Galaxies. , 40:539–577, January 2002. doi: 10.1146/annurev.astro.40.120401.150547.

[50] Planck Collaboration, P. A. R. Ade, N. Aghanim, C. Armitage-Caplan, M. Arnaud, M. Ashdown, F. Atrio-Barandela, J. Aumont, H. Aussel, C. Baccigalupi, A. J. Banday, R. B. Barreiro, R. Barrena, M. Bartelmann, J. G. Bartlett, E. Battaner, K. Benabed, A. Benoît, A. Benoit-Lévy, J. P. Bernard, M. Bersanelli, P. Bielewicz, I. Bikmaev, J. Bobin, J. J. Bock, H. Böhringer, A. Bonaldi, J. R. Bond, J. Borrill, F. R. Bouchet, M. Bridges, M. Bucher, R. Burenin, C. Burigana, R. C. Butler, J. F. Cardoso, P. Carvalho, A. Catalano, A. Challinor, A. Chamballu, R. R. Chary, X. Chen, H. C. Chiang, L. Y. Chiang, G. Chon, P. R. Christensen, E. Churazov, S. Church, D. L. Clements, S. Colombi, L. P. L. Colombo, B. Comis, F. Couchot, A. Coulais, B. P. Crill, A. Curto, F. Cuttaia, A. Da Silva, H. Dahle, L. Danese, R. D. Davies, R. J. Davis, P. de Bernardis, A. de Rosa, G. de Zotti, J. Delabrouille, J. M. Delouis, J. Démoclès, F. X. Désert, C. Dickinson, J. M. Diego, K. Dolag, H. Dole, S. Donzelli, O. Doré, M. Douspis, X. Dupac, G. Efstathiou, P. R. M. Eisenhardt, T. A. Enßlin, H. K. Eriksen, F. Feroz, F. Finelli, I. Flores-Cacho, O. Forni, M. Frailis, E. Franceschi, S. Fromenteau, S. Galeotta, K. Ganga, R. T. Génova-Santos, M. Giard, G. Giardino, M. Gilfanov, Y. Giraud-Héraud, J. González-Nuevo, K. M. Górski, K. J. B. Grainge, S. Gratton, A. Gregorio, E. Groeneboom, N., A. Gruppuso, F. K. Hansen, D. Hanson, D. Harrison, A. Hempel, S. Henrot-Versillé, C. Hernández-Monteagudo, D. Herranz, S. R. Hildebrandt, E. Hivon, M. Hobson, W. A. Holmes, A. Hornstrup, W. Hovest, K. M. Huffenberger, G. Hurier, N. Hurley-Walker, A. H. Jaffe, T. R. Jaffe, W. C. Jones, M. Juvela, E. Keihänen, R. Keskitalo, I. Khamitov, T. S. Kisner, R. Kneissl, J. Knoche, L. Knox, M. Kunz, H. Kurki-Suonio, G. Lagache, A. Lähteenmäki, J. M. Lamarre, A. Lasenby, R. J. Laureijs, C. R. Lawrence, J. P. Leahy, R. Leonardi, J. León-Tavares, J. Lesgourgues, C. Li, A. Liddle, M. Liguori, P. B. Lilje, M. Linden-Vørnle, M. López-Caniego, P. M. Lubin, J. F. Macías-Pérez, C. J. MacTavish, B. Maffei, D. Maino, N. Mandolesi, M. Maris, D. J. Marshall, P. G. Martin, E. Martínez-González, S. Masi, M. Massardi, S. Matarrese, F. Matthai, P. Mazzotta, S. Mei, P. R.

117

Meinhold, A. Melchiorri, J. B. Melin, L. Mendes, A. Mennella, M. Migliaccio, K. Mikkelsen, S. Mitra, M. A. Miville-Deschênes, A. Moneti, L. Montier, G. Morgante, D. Mortlock, D. Munshi, J. A. Murphy, P. Naselsky, F. Nati, P. Natoli, N. P. H. Nesvadba, C. B. Netterfield, H. U. Nørgaard-Nielsen, F. Noviello, D. Novikov, I. Novikov, I. J. O'Dwyer, M. Olamaie, S. Osborne, C. A. Oxborrow, F. Paci, L. Pagano, F. Pajot, D. Paoletti, F. Pasian, G. Patanchon, T. J. Pearson, O. Perdereau, L. Perotto, Y. C. Perrott, F. Perrotta, F. Piacentini, M. Piat, E. Pierpaoli, D. Pietrobon, S. Plaszczynski, E. Pointecouteau, G. Polenta, N. Ponthieu, L. Popa, T. Poutanen, G. W. Pratt, G. Prézeau, S. Prunet, J. L. Puget, J. P. Rachen, W. T. Reach, R. Rebolo, M. Reinecke, M. Remazeilles, C. Renault, S. Ricciardi, T. Riller, I. Ristorcelli, G. Rocha, C. Rosset, G. Roudier, M. Rowan-Robinson, J. A. Rubiño-Martín, C. Rumsey, B. Rusholme, M. Sandri, D. Santos, R. D. E. Saunders, G. Savini, M. P. Schammel, D. Scott, M. D. Seiffert, E. P. S. Shellard, T. W. Shimwell, L. D. Spencer, S. A. Stanford, J. L. Starck, V. Stolyarov, R. Stompor, R. Sudiwala, R. Sunyaev, F. Sureau, D. Sutton, A. S. Suur-Uski, J. F. Sygnet, J. A. Tauber, D. Tavagnacco, L. Terenzi, L. Toffolatti, M. Tomasi, M. Tristram, M. Tucci, J. Tuovinen, M. Türler, G. Umana, L. Valenziano, J. Valiviita, B. Van Tent, L. Vibert, P. Vielva, F. Villa, N. Vittorio, L. A. Wade, B. D. Wandelt, M. White, S. D. M. White, D. Yvon, A. Zacchei, and A. Zonca. Planck 2013 results. XXIX. The Planck catalogue of Sunyaev-Zeldovich sources. , 571:A29, November 2014. doi: 10.1051/0004-6361/201321523.

[51] D. Eckert, S. Ettori, E. Pointecouteau, S. Molendi, S. Paltani, and C. Tchernin. The XMM cluster outskirts project (X- COP). *Astronomische Nachrichten*, 338(293):293–298, March 2017. doi: 10.1002/asna.201713345.

[52] S. Ettori, V. Ghirardini, D. Eckert, E. Pointecouteau, F. Gastaldello, M. Sereno, M. Gaspari, S. Ghizzardi, M. Roncarelli, and M. Rossetti. Hydrostatic mass profiles in X-COP galaxy clusters. , 621:A39, January 2019. doi: 10.1051/0004-6361/201833323.

[53] D. Eckert, V. Ghirardini, S. Ettori, E. Rasia, V. Biffi, E. Pointecouteau, M. Rossetti, S. Molendi, F. Vazza, F. Gastaldello, M. Gaspari, S. De Grandi, S. Ghizzardi, H. Bourdin, C. Tchernin, and M. Roncarelli. Non-thermal pressure support in X-COP galaxy clusters. , 621:A40, January 2019. doi: 10.1051/0004-6361/201833324.

[54] H. Hoekstra, T. S. van Albada, and R. Sancisi. On the apparent coupling of neutral hydrogen and dark matter in spiral galaxies. , 323(2):453–459, May 2001. doi: 10.1046/j.1365-8711.2001.04214.x.

[55] R. A. Swaters, R. Sancisi, J. M. van der Hulst, and T. S. van Albada. The link between the baryonic mass distribution and the rotation curve shape. , 425(3):2299–2308, September 2012. doi: 10.1111/j.1365-2966.2012.21599.x.

[56] K. G. Begeman, A. H. Broeils, and R. H. Sanders. Extended rotation curves of spiral galaxies : dark haloes and modified dynamics. , 249:523, April 1991. doi: 10.1093/mnras/249.3.523.

[57] A. Burkert. The Structure of Dark Matter Halos in Dwarf Galaxies. , 447: L25–L28, July 1995. doi: 10.1086/309560.

[58] Pengfei Li, Federico Lelli, Stacy McGaugh, and James Schombert. A Comprehensive Catalog of Dark Matter Halo Models for SPARC Galaxies. , 247 (1):31, March 2020. doi: 10.3847/1538-4365/ab700e.

[59] Julio F. Navarro, Carlos S. Frenk, and Simon D. M. White. The Structure of Cold Dark Matter Halos. , 462:563, May 1996. doi: 10.1086/177173.

[60] J. Einasto. On the Construction of a Composite Model for the Galaxy and on the Determination of the System of Galactic Parameters. *Trudy Astrofizicheskogo Instituta Alma-Ata*, 5:87–100, January 1965.

[61] Aaron A. Dutton and Andrea V. Macciò. Cold dark matter haloes in the Planck era: evolution of structural parameters for Einasto and NFW profiles. , 441(4):3359–3374, July 2014. doi: 10.1093/mnras/stu742.

[62] J. P. Ostriker and P. J. E. Peebles. A Numerical Study of the Stability of Flattened Galaxies: or, can Cold Galaxies Survive? , 186:467–480, December 1973. doi: 10.1086/152513.

[63] R. A. Swaters, R. Sancisi, J. M. van der Hulst, and T. S. van Albada. The link between the baryonic mass distribution and the rotation curve shape. , 425(3):2299–2308, September 2012. doi: 10.1111/j.1365-2966.2012.21599.x.

[64] Andrew A. Neath and Joseph E. Cavanaugh. The bayesian information criterion: background, derivation, and applications. *WIREs Computational Statistics*, 4(2):199–203, 2012. doi: https://doi.org/10.1002/wics.199. URL https://wires.onlinelibrary.wiley.com/doi/abs/10.1002/wics.199.

[65] W. J. G. de Blok. The Core-Cusp Problem. *Advances in Astronomy*, 2010: 789293, January 2010. doi: 10.1155/2010/789293.

[66] Benjamin P. Moster, Thorsten Naab, and Simon D. M. White. Galactic star formation and accretion histories from matching galaxies to dark matter haloes. , 428(4):3121–3138, February 2013. doi: 10.1093/mnras/sts261.

[67] Xiaohu Yang, H. J. Mo, and Frank C. van den Bosch. Constraining galaxy formation and cosmology with the conditional luminosity function of galaxies. , 339(4):1057–1080, March 2003. doi: 10.1046/j.1365-8711.2003.06254.x.

[68] Benjamin P. Moster, Rachel S. Somerville, Christian Maulbetsch, Frank C. van den Bosch, Andrea V. Macciò, Thorsten Naab, and Ludwig Oser. Constraints on the Relationship between Stellar Mass and Halo Mass at Low and High Redshift. , 710(2):903–923, February 2010. doi: 10.1088/0004-637X/710/2/903.

[69] R. H. Sanders. The Virial Discrepancy in Clusters of Galaxies in the Context of Modified Newtonian Dynamics. , 512(1):L23–L26, February 1999. doi: 10.1086/311865.

[70] Mordehai Milgrom. Marriage à-la-MOND: Baryonic dark matter in galaxy clusters and the cooling flow puzzle. , 51(10-12):906–915, May 2008. doi: 10.1016/j.newar.2008.03.023.

[71] G. W. Angus. Is an 11eV sterile neutrino consistent with clusters, the cosmic microwave background and modified Newtonian dynamics? , 394(1):527–532, March 2009. doi: 10.1111/j.1365-2966.2008.14341.x.

[72] Kyu-Hyun Chae, Federico Lelli, Harry Desmond, Stacy S. McGaugh, Pengfei Li, and James M. Schombert. Testing the Strong Equivalence Principle: Detection of the External Field Effect in Rotationally Supported Galaxies. , 904 (1):51, November 2020. doi: 10.3847/1538-4357/abbb96.

[73] Kyu-Hyun Chae, Harry Desmond, Federico Lelli, Stacy S. McGaugh, and James M. Schombert. Testing the Strong Equivalence Principle. II. Relating the External Field Effect in Galaxy Rotation Curves to the Large-scale Structure of the Universe. , 921(2):104, November 2021. doi: 10.3847/1538-4357/ac1bba.

[74] Ricardo Herbonnet, Cristóbal Sifón, Henk Hoekstra, Yannick Bahé, Remco F. J. van der Burg, Jean-Baptiste Melin, Anja von der Linden, David Sand, Scott Kay, and David Barnes. CCCP and MENeaCS: (updated) weak-lensing masses for 100 galaxy clusters. , 497(4):4684–4703, October 2020. doi: 10.1093/mnras/staa2303.

[75] V. Ghirardini, S. Ettori, D. Eckert, S. Molendi, F. Gastaldello, E. Pointecouteau, G. Hurier, and H. Bourdin. The XMM Cluster Outskirts Project (X-COP): Thermodynamic properties of the intracluster medium out to R_{200} in Abell 2319. , 614:A7, June 2018. doi: 10.1051/0004-6361/201731748.

[76] D. Eckert, S. Ettori, E. Pointecouteau, S. Molendi, S. Paltani, and C. Tchernin. The XMM cluster outskirts project (X- COP). *Astronomische Nachrichten*, 338(293):293–298, March 2017. doi: 10.1002/asna.201713345.

[77] P. Rosati, P. Tozzi, R. Gobat, J. S. Santos, M. Nonino, R. Demarco, C. Lidman, C. R. Mullis, V. Strazzullo, H. Böhringer, R. Fassbender, K. Dawson, M. Tanaka, J. Jee, H. Ford, G. Lamer, and A. Schwope. Multi-wavelength study of XMMU J2235.3-2557: the most massive galaxy cluster at z > 1. , 508(2):583–591, December 2009. doi: 10.1051/0004-6361/200913099.

[78] G. W. Angus, B. Famaey, and H. S. Zhao. Can MOND take a bullet? Analytical comparisons of three versions of MOND beyond spherical symmetry. , 371(1):138–146, September 2006. doi: 10.1111/j.1365-2966.2006.10668.x.

[79] Garry W. Angus, Huan Yuan Shan, Hong Sheng Zhao, and Benoit Famaey. On the Proof of Dark Matter, the Law of Gravity, and the Mass of Neutrinos. , 654(1):L13–L16, January 2007. doi: 10.1086/510738.

[80] Kyu-Hyun Chae, Federico Lelli, Harry Desmond, Stacy S. McGaugh, Pengfei Li, and James M. Schombert. Testing the Strong Equivalence Principle: Detection of the External Field Effect in Rotationally Supported Galaxies. , 904 (1):51, November 2020. doi: 10.3847/1538-4357/abbb96.

Acknowledgments